This is to certify that the
dissertation entitled

THE FORMATION AND ACTIVITY OF PLATINUM ADLAYERS ON DIAMOND ELECTRODES FOR ELECTROCATALYSIS

presented by

JASON ALAN BENNETT

has been accepted towards fulfillment
of the requirements for the

Doctoral degree in Chemistry

Greg M. Swain
Major Professor's Signature

August 13, 2006
Date

MSU is an Affirmative Action/Equal Opportunity Institution

THE FORMATION AND ACTIVITY OF PLATINUM ADLAYERS ON DIAMOND ELECTRODES FOR ELECTROCATALYSIS

By

Jason Alan Bennett

A DISSERTATION

Submitted to
Michigan State University
in partial fulfillment of the requirements
for the degree of

DOCTOR OF PHILOSOPHY

Department of Chemistry

2006

ABSTRACT

THE FORMATION AND ACTIVITY OF PLATINUM ADLAYERS ON DIAMOND ELECTRODES FOR ELECTROCATALYSIS

By

Jason Alan Bennett

The research described in this dissertation evaluates the potential of diamond as an advanced carbon electrocatalyst support material. This includes both assessing the physical and electrochemical properties of the material as well as a comprehensive investigation into the nature of metal adlayer formation on the material.

The physical and electrochemical properties of boron-doped polycrystalline diamond thin films, prepared with varying levels of sp^2-bonded nondiamond carbon impurity, were systematically investigated. This impurity was introduced through adjustment of the methane-to-hydrogen source gas ratio used for the deposition. Increasing the methane-to-hydrogen ratio resulted in an increase in the fraction of grain boundary, the extent of secondary nucleation, and the amount of sp^2-bonded nondiamond carbon impurity. The effect of the source gas ratio on the electrochemical response towards several well known redox analytes and the oxygen reduction reaction in both acidic and alkaline media was also investigated. The results demonstrate that the grain boundaries, and the sp^2-bonded nondiamond carbon impurity presumably residing there, can have a significant impact on the electrode reaction kinetics for certain redox systems and little influence for others.

The morphological and microstructural stability of microcrystalline and nanocrystalline boron-doped diamond thin film electrodes under conditions observed in phosphoric acid fuel cells was investigated. The electrodes were exposed to a 2 h period of anodic polarization in 85% H_3PO_4 at ~180 °C and 0.1 A/cm^2. Catastrophic degradation was not observed for either type of diamond. The oxidation of the microcrystalline diamond was limited to the surface, and the effects could be reversed upon exposure to a hydrogen plasma. The nanocrystalline diamond exhibited similar responses to well known redox analytes after anodic polarization, however an irreversible increase in the film capacitance was also observed. This is possibly due to surface pitting or heterogeneous conductivity in the film resulting in "hot spots."

Electrodeposition of Pt adlayers as a function of both diamond morphology and diamond surface chemistry was also investigated using a pulsed galvanostatic deposition approach. Our goal was to minimize the particle size and size dispersion (*ca.* 5-15 nm) while maximizing the particle density (*ca.* 10^{10} cm^{-2}) and catalytic activity towards the oxygen reduction reaction. Depositing Pt on clean H-terminated diamond surfaces using 10 pulses of 1-s (50% duty cycle) at a pulse current of 1.25 mA/cm^2 produced the most ideal particles in terms of size (*ca.* 30 nm), density (*ca.* 2 x 10^{10} cm^{-2}), and catalytic activity. Additionally the nucleation and growth mechanism of Pt on microcrystalline and nanocrystalline diamond thin film studied using chronoamperometry indicated that the nucleation moves from instantaneous to progressive with increasing deposition overpotential. Finally, an introductory study of catalyst loss from the diamond surface indicated that the loss of Pt surface area is likely due to Ostwald ripening.

ACKNOWLEDGMENTS

There have been so many people who have influenced my life here at Michigan State University, both professionally and personally. First and foremost I would like to thank my principal advisor, Dr. Greg Swain. I am thankful for the guidance you have given me over the last 5 years. I am additionally grateful that you allowed me to grow as a scientist while still maintaining my livelihood. I will always remember "the proof is in the pudding."

I would also like to thank my second reader, Dr. Merlin Bruening for his additional guidance and many memorable interactions. Additionally, I thank my remaining guidance committee members, Dr. Jim McCusker and Dr. Donnie Reinhard for their roles in this degree. Thank you as well to the MSU chemistry department staff for all their efforts as well as Ewa Danielewicz who trained me on and often provided assistance with the scanning electron microscope.

Of course graduate school would have been much more difficult if it weren't for the love and support of coworkers, friends, and family. I extend a special thanks to past and present Swain group members. Working in the Swain lab has been an enjoyable and rewarding experience. I am especially grateful to those of you who have directly helped me in this pursuit: Jian, Matt, Maggie, and Shannon for their guidance and leadership during my initial years in the group as well as Stotter, Fish, Elizabeth, and Audrey for fruitful discussions and help during these last remaining years.

The friendships I have made here have been the most rewarding part of this journey. To Stotter, Carl, Fish, Mel, Elizabeth, Audrey, Jesse, Bahvik, and Little J: Thank you all for the memories and remember that you are all "cool fish in the nerd pond." Additionally I owe a special thank you to Sarah for her continuous friendship and enduring love. You have added an array of vibrant colors to every aspect of my life.

Finally, I would never have even made it to graduate school without the continuing support and encouragement from my loving family. You guys have always been there in good times and bad. I have cherished every moment and look forward to what the future has in store for us all. Thank you again to everyone who helped me complete this journey.

– Jason –

TABLE OF CONTENTS

LIST OF TABLES

LIST OF FIGURES

CHAPTER 1

Introduction

1.1 Background

Catalysis is of vital importance in today's chemical industry. In fact, few chemical processes are conducted without the use of a catalyst.[1] A subsection of catalysis is electrocatalysis, defined as the study of heterogeneous redox reactions that involve reactant and product species transferring electrons through an electrolyte/catalyst interface.[2] Of particular interest to our group are supported electrocatalysts due to their high surface-to-volume ratio, high dispersion over the support surface and stability. Electrocatalysis is prominent in several applications such as electrochemical chemical synthesis, chemical sensing and energy storage and conversion.

Growing concern over the environmental impacts from burning fossil fuels, limited fuel supplies and reliance on foreign oil has lead to considerable interest in fuel cells as a clean renewable energy alternative for stationary and portable power applications. The fuel cell is not a new concept as it was invented by Sir William Grove in 1839. For example, fuel cells have been used by NASA in aerospace applications for several decades.[3] A fuel cell converts chemical energy into electrical energy through electrocatalytic reactions at two electrodes known as the anode and cathode. Each electrode consists of a porous gas diffusion material and some form of metallic electrocatalyst particles supported on carbon.

The U.S. Department of Energy (DOE) seeks to develop hydrogen, fuel cell and infrastructure technologies, in order to give the public a practical and cost-effective fuel cell vehicle by 2020.[4] However, there are several technological hurdles that must be overcome before fuel cells can become a viable, clean energy alternative for transportation: (*i*) supplying, dispersing, and storing alternate fuels (*e.g.*, H_2),[5] (*ii*) reducing cost and improving efficiency through reduced electrocatalyst loading or newly developed non-noble metal electrocatalysts,[6] (*iii*) development of reliable physical and chemical sensors[7] and (*iv*) preventing activity loss caused by carbon support degradation and bipolar plate corrosion. This work is a continuation of our group's efforts to develop an advanced state-of-the-art electrocatalyst support material that can withstand high temperatures and current density for extended periods of time without structural degradation or decreased catalytic activity. Specifically, the investigation of electrocatalyst metal (*e.g.*, Pt) phase formation on diamond will be presented.

1.2 Carbon Material Properties

Various forms of carbon have been used as electrochemical electrodes over the years. Carbon electrodes are commonly composed of sp^2-hybridized atoms as found in highly ordered pyrolytic graphite (HOPG), glassy carbon (GC), as well as carbon nanotubes (CNTs) and nanofibers (CNFs). However, electrically conducting diamond, a sp^3-hybridized form of carbon, has been a focus of study in recent years as an electrode. It is also possible for the carbon to contain a mixed sp^3 and sp^2 microstructure, and such materials are referred to as diamond-like carbon (DLC).

Carbon materials differ from metals for electrochemical purposes in several ways, as discussed by McCreery:[8] (*i*) electronic properties ranging from metallic to semimetallic depending on the carbon microstructure, (*ii*) the ease at which the carbon surface can be modified through adsorption or chemical modification, (*iii*) the very complex surface chemistry of carbon which includes various types of functional groups and surface oxides, and (*iv*) the wider potential window of carbon materials compared to metal electrodes, thus making possible the study of electrochemical processes that were previously unattainable.[8] There are two types of carbon electrodes relevant to this research: glassy carbon (a microstructurally disordered sp^2-bonded material) and boron-doped diamond (a polycrystalline sp^3-bonded material). The structure of these materials is shown in Figure 1.1 and the properties are compared in Table 1.1.[8,9] The terms L_a and L_c in Figure 1A describe the ordered domain width and graphene sheet stacking thickness, respectively.

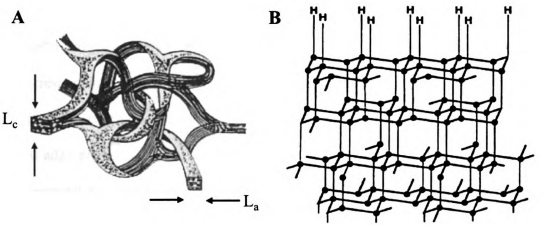

Figure 1.1. The microstructure of (A) glassy carbon and (B) sp^3-bonded diamond. Figures adapted from McCreery and Fischer, respectively.[8,10]

Table 1.1. A Physical and Electrochemical Property Comparison of Glassy Carbon and Boron-Doped Diamond

Material	L_a (Å)	Resistivity (Ω-cm)	Density (g/cm^3)	Capacitance ($\mu F/cm^2$)
Glassy Carbon	~50	4×10^{-3}	1.5	~33
Boron-Doped Diamond	N.A.	~0.1	3.51	3-7

Glassy carbon (GC) is the most popular electrode material for electroanalytical measurements because it is active and yields a reproducible response.[11] It has electrochemical characteristics similar to those of the edge plane of HOPG, and is mechanically strong and nonporous. GC has metallic-like electronic properties. For example, freshly polished GC exhibits a capacitance of *ca.* 30 $\mu F/cm^2$ and a resistivity of *ca.* 4×10^{-3} Ω-cm.[8] Raman spectroscopy is often used to characterize the microstructures of carbon materials, including those of glassy carbon and diamond. Figure 1.2 shows representative spectra for GC (top) and single crystal diamond (bottom). The GC spectrum yields two recognizable peaks, one at *ca.* 1350 cm^{-1} corresponding to the "disorder" band (commonly referred to as the D or A_{1g} band), and the other at *ca.* 1590 cm^{-1} corresponding to the graphite band (commonly referred to as the G or E_{2g} band).[12] A ratio of the respective peak intensities (D/G ratio) gives the fractional amount of exposed edge plane.[13] This is usually denoted as θ_{edge}, and provides a measure of the microstructural disorder in the material. The spectrum for single crystal diamond is quite different, exhibiting a single peak at 1332 cm^{-1} which is associated with the first order diamond phonon. The position and width of this peak is sensitive to factors such as the crystallite size, optical density, boron doping level (synthetic diamond), net stress, defect

density, and film quality (synthetic diamond).[14-16] Raman spectroscopy is a useful tool for assessing the relative levels of sp^2- and sp^3-bonded carbon in a CVD diamond film. This will be discussed further in Chapters 2 and 3.

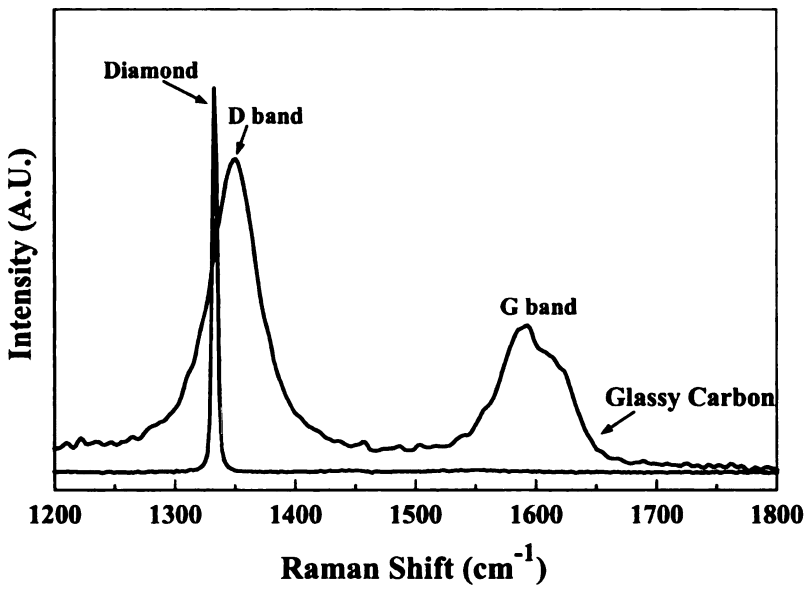

Figure 1.2. Comparative Raman spectra for glassy carbon and single crystal diamond.

Glassy carbon also exhibits characteristic electrochemical properties especially with regard to the background cyclic voltammetric *i-E* curves. Figure 1.3 compares the background cyclic voltammetric *i-E* curves for GC and a boron-doped microcrystalline diamond thin film (discussed below). The *i-E* curve for GC is characterized by a wide potential window, at least as compared to metal electrodes, a large background current and a highly visible reversible redox couple associated with electroactive surface quinone functionalities.[17-20]

Boron-doped diamond has emerged as an attractive alternate electrode to commonly used sp^2-bonded carbon, such as GC, for several electrochemical applications including electroanalysis and electrolytic water purification.[9,21-27] High-quality diamond (*i.e.*, minimal sp^2 nondiamond carbon impurity) possesses several electrochemical properties that make it an attractive material including:[23,28-30] (*i*) a low and stable background current and capacitance in aqueous media (*ca.* 5 $\mu F/cm^2$)[31], (*ii*) a wide working potential window in many aqueous electrolytes (~3-4 V), (*iii*) rapid electron transfer kinetics for several redox systems without any conventional pretreatment, (*iv*) long-term response stability and (*v*) morphological and microstructural stability during anodic and cathodic polarization (~10 A/cm^2) in both acidic and alkaline media. A representative background voltammetric *i-E* curve for a boron-doped microcrystalline diamond thin film is shown in Figure 1.3.

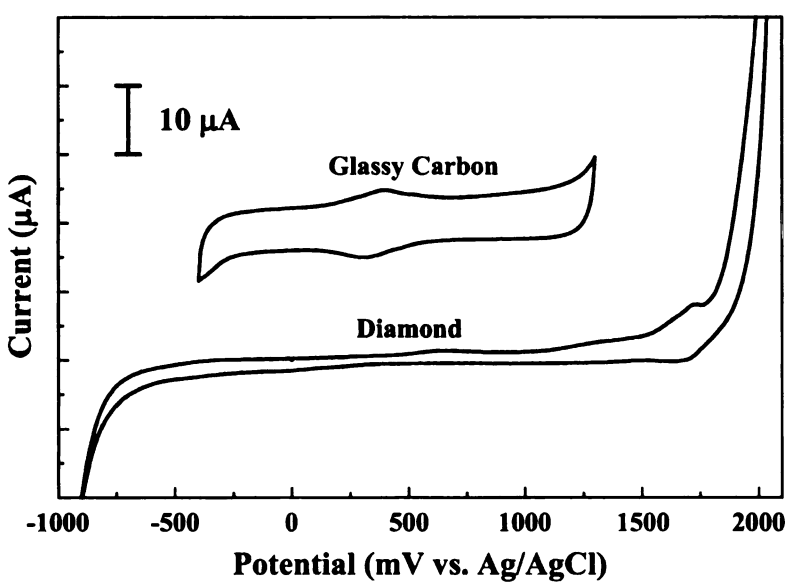

Figure 1.3. Background voltammetric *i-E* curves for glassy carbon and boron-doped microcrystalline diamond thin film in degassed 0.1 M $HClO_4$. Scan rate = 100 mV/s. Geometric area = 0.2 cm^2.

The diamond microstructure consists of tetrahedrally-bonded sp^3-hybridized carbon atoms with each bonded to four others, as shown in Figure 1.1. The surface is usually hydrogen-terminated as shown in the figure; however, the surface chemistry can be easily altered (*e.g.*, oxygen-terminated or aryl molecule modified), as is discussed in Chapter 6 of this dissertation. Diamond can be synthetically grown using several methods including a process employed in our group, microwave-assisted plasma chemical vapor deposition (MPCVD). A typical CVD reactor used for diamond growth (see Figure 2.2) consists of source gases (CH_4 and H_2 for microcrystalline growth and CH_4, H_2 and Ar for nanocrystalline growth), a dopant gas (*e.g.*, B_2H_6 to make the diamond, a natural insulator, electrically conductive), mass flow controllers (M.F.C.) to regulate the gas flows into the reaction chamber, a plasma activation source (*e.g.*, microwave generator) and mechanical pumps and throttle exhaust valve for controlling the system pressure.[9] Two of the most critical parameters for diamond growth are the substrate temperature and system pressure. Such a reactor can be used to grow two types of electrically conducting diamond: microcrystalline (>1 μm crystallite size) and nanocrystalline (~10 to 20 nm crystallite size) thin films. Despite the different morphologies, both types of diamond are highly conductive and possess semi-metallic properties. The nominal boron dopant concentration is *ca.* 10^{20} B/cm^3 and the film resistivity is less than 0.05 Ω cm. The most common architectures are single crystal and polycrystalline thin film.

Microcrystalline diamond is deposited using CH_4 as the primary carbon source. The selected growth conditions convert CH_4 to methyl radicals, $CH_3^{\bullet}$, which serve as the

primary growth species.[32] The added H_2 in the form of atomic hydrogen, $H^{\bullet}$, has three major functions.[9] First, it abstracts hydrogen from methane to produce methyl radicals in the gas phase (*i.e.*, primary reactant species) and from chemisorbed methyl substituents on the surface to produce radical sites for further carbon attachment. Second, it passivates dangling bonds on the surface, which inhibits reconstruction to a sp^2-bonded phase on the growth surface. Third, it rapidly gasifies any of the sp^2-bonded nondiamond carbon impurity that forms.[9] This is why the cool down in atomic hydrogen is an extremely important part of the diamond growth process in order to achieve high quality (*i.e.*, no sp^2-bonded nondiamond carbon impurity) hydrogen-terminated films.

Nanocrystalline diamond is also grown using CH_4 as the primary carbon source, but in an H_2-deficient, Ar-rich atmosphere. The $CH_4/(H_2 + Ar)$ source gas composition affects the film morphology, surface roughness and grain size.[33,34] Unlike microcrystalline diamond, the primary growth mechanism for nanocrystalline diamond involves the insertion of the C_2 carbon dimer into C–C and C–H bonds on the growth surface.[34] The C_2 dimer also appears to be the primary nucleation species when the Ar composition in the gas phase is >90%.[35] The lack of H_2 in the source gas as well as a higher growth pressure results in a higher rate of renucleation. This leads to a continuous and relatively smooth film at a low nominal film thickness. The nucleation and growth of nanocrystalline diamond thin film has been reviewed extensively by Gruen.[35,36]

Usually the growth and cool down conditions for both diamond types are selected to achieve high quality sp^3 carbon and to minimize any sp^2 nondiamond carbon impurity

formation. A key factor in achieving this involves selecting the proper source gas ratio. Bachmann *et al.* created a diagram showing the relationship between the C/H/O ratios and diamond growth.[37,38] An adaptation of the Bachmann triangle is shown in Figure 1.4. The lower shaded region represents C/H/O ratios where no diamond growth occurs, while the top shaded region represents C/H/O ratios where sp^2-bonded nondiamond carbon growth occurs. The small white region in the middle represents the narrow range of source gas composition that will result in diamond growth. The high-quality diamond films produced in our group are grown using only carbon and hydrogen source gases, without added oxygen. This is expressed by the bottom left corner of the triangle where the concentration of H is high compared to the concentration of C (and the concentration of O is zero). As the amount of C increases with respect to H, the quality of the film decreases as less diamond is grown in favor of nondiamond sp^2 carbon growth. This is the basis for the study presented in Chapter 3 where the physical and electrochemical properties of diamond films are assessed as a function of increasing C/H ratio in the diamond growth and hence an increased incorporation of nondiamond carbon within the film microstructure.

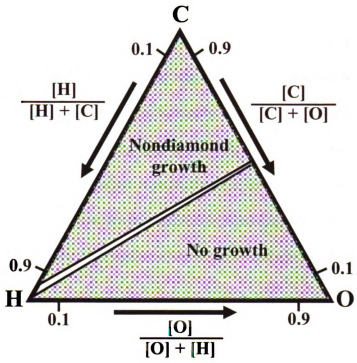

Figure 1.4. Summary of relative [C], [H], and [O] concentrations required to achieve diamond growth. Adapted from Bachmann *et al.*[37,38]

1.3 Electrocatalyst Support Materials

Electrocatalysts are used in both the cathode and anode of PEM fuel cells. Fuel cells are gaining popularity for transportation because they represent a form of clean energy (H_2O is the only waste product) and could potentially lessen our society's reliance on fossil fuels. Currently, Pt and Pt-based alloys are the most common catalysts used in phosphoric acid and polymer electrolyte membrane fuel cells (PAFC and PEMFC, respectively). However, these metals are costly and in somewhat limited supply. For example, in 1987, the lowest loading to give a continuous layer was estimated to cost ~$1000/kW for the catalyst alone![39] The current cost for a PEM fuel cell stack is ~$110/kW, and DOE targets are to reduce this to $30/kW by the year 2015.[4]

There is strong interest in reducing the metal loading and designing more active and less expensive catalysts to reduce the overall fuel cell cost. Supported electrocatalysts have the surface area and turn-over number needed for fuel cells but a suitable material is required on which to highly disperse the nanometer-sized catalyst particles. Figure 1.5 shows a schematic of a PEMFC with a magnified view of the cathode showing the electrocatalyst support material and the supported electrocatalyst particles. Graphitic carbon powder is a commonly used support material that has several desired properties including high surface area, low cost and electrical conductivity.

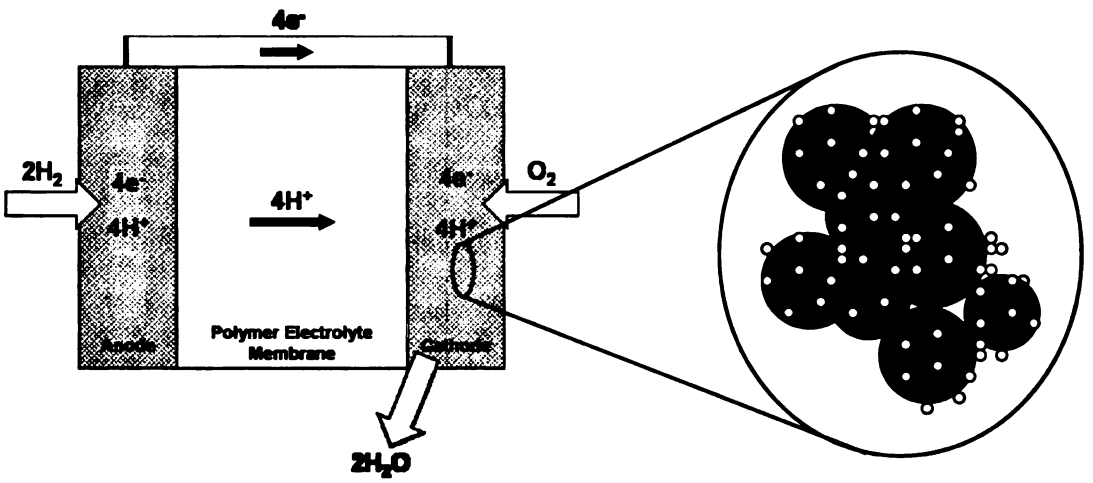

Figure 1.5. Schematic of polymer electrolyte membrane fuel cell (PEMFC). The magnified region shows the active cathode – nanometer-sized catalyst particles (*e.g.*, Pt) highly dispersed on a support material.

Graphitic carbon also has some limitations as a support, most notably its microporosity, which limits access of reactants to some of the electrocatalyst and susceptibility to microstructural degradation due to oxidation and/or corrosion processes. It is important to note that the overall efficiency of a low temperature fuel cell (*e.g.*,

PAFC or PEMFC) is limited by reactions at the cathode where oxygen reduction occurs. The thermodynamic cell voltage, E_{cell}, for this reaction, and hence the optimal fuel cell operating voltage, is 1.23 V.[39,40] However, E_{cell} values of ~700 mV are more commonly observed (using Pt loadings of *ca.* 0.7 mg_{Pt}/cm^2, H_2/air PEMFC at 80 °C)[6] due to sluggish kinetics for the oxygen reduction reaction at the cathode as well as carbon support degradation. The carbon surface can also undergo oxidation and corrosion, the latter by a reaction written as follows:[39]

$$C + 2H_2O \rightarrow CO_2 + 4H^+ + 4e^- \qquad (1.3.1)$$

Since this reaction is electrochemical (E^o = 0.118 V vs. SHE), its rate increases with increasing cathode potential. Additionally, the corrosion rate also increases at a given potential with increasing temperature, vapor pressure, oxygen content and catalyst loading.[41] Furthermore, Pt, currently the most active catalyst for the oxygen reduction reaction in acidic media, significantly accelerates the carbon corrosion rate at lower temperatures (~50 °C) and potentials (~0.55 V vs. SHE) compared to the rate for the base carbon.[41] Carbon support corrosion causes increased ohmic resistance, catalyst particle agglomeration and particle detachment. All these result in a loss in catalytic activity. If the degradation is severe enough, complete electrode failure will result. Though carbon corrosion under PEMFC cathode potentials used in automotive applications (*e.g.*, 0.65 – 0.8 V) was previously thought not to be a serious problem, it was recently determined that cathode potential ranges that far exceed the stability region of standard carbon supports even at 80 °C were reached.[42] For example, PEMFCs in automotive

applications undergo an estimated 30,000 startup/shutdown cycles over the life of a vehicle, which can lead to short term potential excursions of the cathode to potentials as high as 1.5 V vs. SHE due to H_2/air fronts in the anode compartment. At potentials this high, the corrosion rate of current sp^2 carbon supports is high.[42]

It is widely recognized that advanced support materials are needed before fuel cells can become commercially viable, particularly for transportation. These materials must have the same properties as the currently used sp^2-bonded carbons but not the shortcomings of microporosity and corrosion susceptibility. Several types of materials are currently being investigated as alternates. One receiving considerable attention is carbon nanotubes (CNTs).[43-45] While these materials do have the advantage of being electrically conductive and mechanically stable, they are currently limited by their inherent impurities (*e.g.*, Ni, Co, Fe, etc.) and their expense on the industrial scale.[46] Another alternative is carbon nanofibers (CNFs).[43,44,47] While CNFs are electrically conductive and have a lower impurity content compared to CNTs, they are still quite expensive to produce and their long-term stability has yet to be determined. Other alternate support materials receiving interest are mesoporous carbons[48-50] and carbon aerogels.[51] Mesoporous carbons have the advantage of possessing a very high surface area and a large pore diameter. However, it is currently difficult to control the pore diameter and a post-synthesis treatment is required. Carbon aerogels show promise for better control of the pore size but the stability may be an issue. All these materials have some promise as catalyst supports, however they are still composed of sp^2-bonded carbon and are likely to be susceptible to microstructural degradation. To our knowledge, there has been no long-

term investigation into the morphological stability of these materials under fuel cell conditions.

Over the last ten years, electrically conducting diamond has emerged as an alternative to commonly used sp^2-bonded carbon materials for a variety of applications largely because of its large potential operating range, low background current (*i.e.*, increased signal to background ratio) and resistance to both molecular adsorption and fouling.[21,24-26,52,53] Boron-doped diamond also possesses several properties desired for an electrocatalyst support material including (*i*) high electrical conductivity, (*ii*) dimensional stability at high temperature, potential and current density, (*iii*) resistance to corrosion and (*iv*) with advances in diamond synthesis, a low cost.[24,54,55] The material is limited at present because of its low inherent surface area (maximum in powders is 1-10 m^2/g); although detonation diamond is a form of powderous diamond (electrically insulating) with a high surface area (1000 m^2/g).[56] We seek to develop a high surface area diamond support material that is corrosion resistant, electrically conductive and able to support a high dispersion of electrocatalyst particles. Our most promising results, so far, have come from coating sp^2 carbon paper or diamond powders with a thin film of electrically conducting microcrystalline or nanocrystalline diamond.[10,57] In addition to developing an electrically conducting, high surface area form of diamond, we also seek to better understand, control, and stabilize the electrocatalyst particles on the diamond support surface. Therefore, the fundamentals of metal phase formation are of paramount importance.

1.4 Introduction to Metal Phase Formation

Electrochemically active metal particles are deposited onto carbon support materials by one of several methods including (*i*) the collection of metal colloidal particles from microemulsions,[58] (*ii*) physical vapor deposition,[59 and refs. therein] (*iii*) impregnation,[60] (*iv*) DC sputtering[61-63] and (*v*) electrodeposition.[64-66] Electrodeposition is the preferred method because, unlike the other four, it allows for good control of particle properties (*i.e.*, size, density and size dispersion based on chosen deposition parameters) **and** places the particles in direct contact with areas of the support material that are electrically conducting and electrochemically active.

Ideal supported catalysts should (*i*) have a high activity towards the reaction (*e.g.*, H_2 oxidation or O_2 reduction in the case of a fuel cell), (*ii*) be evenly distributed nanometer-sized (~5-10 nm) particles, (*iii*) have a narrow size distribution, (*iv*) have a high distribution density, (*v*) have electronic communication with the supporting material and (*vi*) have long-term stability with the support material (*i.e.*, not detach from the support). The concept of using supported catalysts instead of metal electrodes comes from the fact that only the surface of the metal is involved in electrochemical reactions. Therefore, reducing the catalyst size increases the electrochemically active surface area, while decreasing catalyst loading. This is extremely important in commercial applications where large agglomerates of Pt do not provide a significant increase in catalyst activity but significantly increase the cost of production.

Electrochemically-driven metal phase formation and adlayer growth on foreign substrates has been extensively studied.[66-70] Pletcher gives examples of such reactions including (*i*) the cathodic deposition of metals, (*ii*) the anodic formation of oxide layers either by metal corrosion or the oxidation of metallic ions in solution, (*iii*) the formation of insoluble salts on an anode (*e.g.*, AgCl) and (*iv*) the conversion of one solid phase on a surface to another with a different lattice structure.[70] The focus of the work described in this dissertation is on the cathodic deposition of metals onto a carbon support material. Figure 1.6 shows an adaptation from Pletcher, which illustrates the process of metal phase formation on an ideal support that is atomically smooth, defect free, and homogeneously electrochemically active over the surface.[70] First, the solvated ion diffuses from the bulk solution to the electrode surface where it is reduced to an ad-atom. These ad-atoms are thermodynamically unstable and should redissolve. This can be seen by equation 1.4.1 where $\Delta G_{Surface}$ is positive and proportional to the surface area and ΔG_{Bulk} is negative and its magnitude is proportional to the phase volume.[70]

$$\Delta G_{Phase} = \Delta G_{Surface} + \Delta G_{Bulk} \qquad (1.4.1)$$

Small centers are thus unstable because they have too high a ratio of surface area/volume (ΔG_{Phase} is positive). Therefore, in order for the nucleus to become stable, it must reach a critical size and this can be achieved by the ad-atoms rapidly diffusing along the surface until they cluster into a nucleus of sufficient size to be stable. In electrodeposition, a high concentration of ad-atoms is favored by using a highly concentrated metal salt solution and by driving the electron transfer process by applying a sufficient overpotential. As time progresses, the metallic nucleus grows due to the incorporation of more ad-atoms.

Therefore, the length of time in which the overpotential is applied must not be too long in order to keep as high a surface area/volume ratio as possible. At extended times, the growing particles begin to grow together or agglomerate, and eventually result in the formation of a continuous layer over the whole cathode surface.

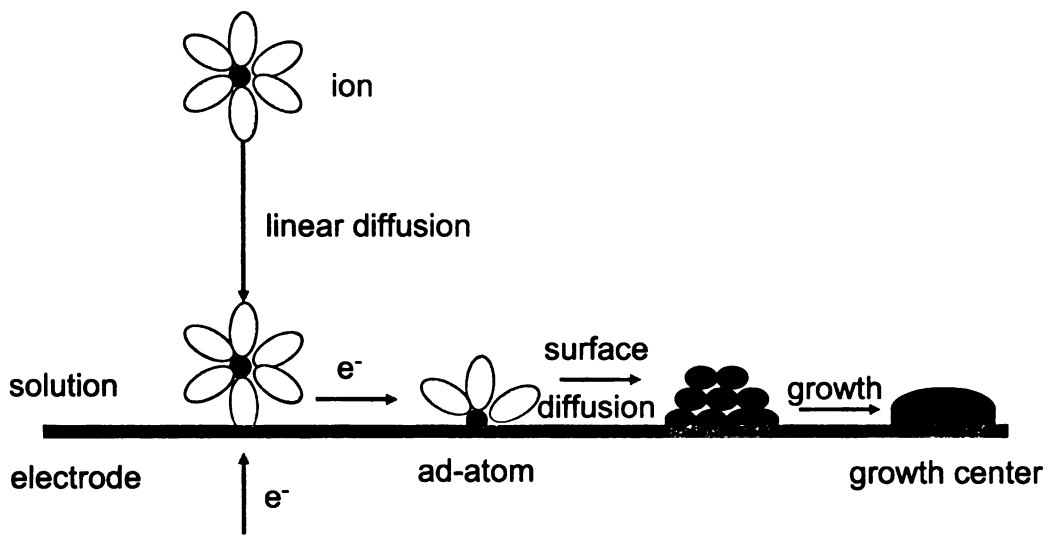

Figure 1.6. Illustration of metal adlayer formation on an ideal (*i.e.*, atomically smooth with homogeneously electronically active) substrate. Adapted from Pletcher.[70]

An important aspect of studying metal phase formation is investigating how an individual metal particle nucleates on the substrate surface. There are two limiting cases commonly used to describe metal phase formation: (*i*) *instantaneous* nucleation and growth where all of the metal nuclei form at the same time and subsequent growth occurs at a particular rate and (*ii*) *progressive* nucleation and growth where new nuclei form over time and subsequent growth occurs from each. Scharifker and Hills presented a way to determine the metal nucleation mechanism by observing the shapes of chronoamperometric *i-t* profiles.[71] A dimensionless *i-t* curve can be obtained for each of

these limiting mechanisms by plotting the square of the ratio of the current to the current max (I^2/I_m^2) vs. the ratio of time and the time at the maximum current (t/t_m).[71] This is shown in Figure 1.7.

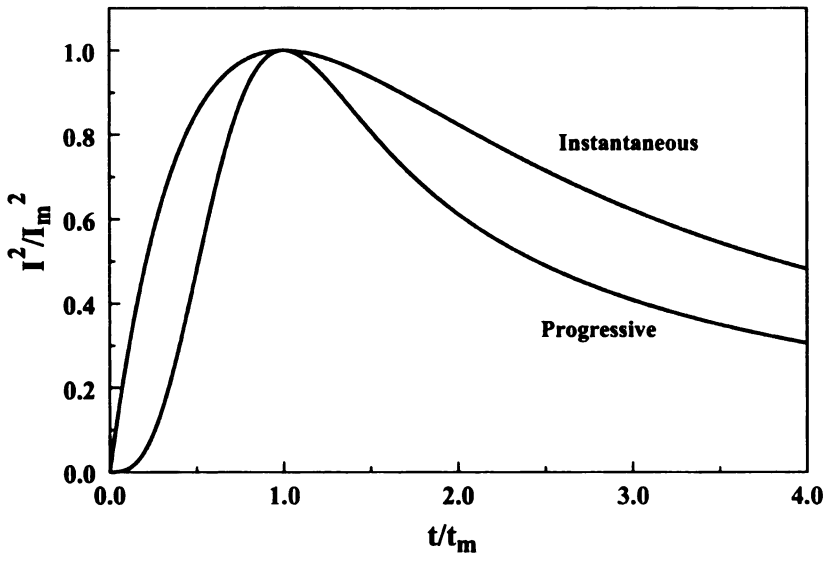

Figure 1.7. Dimensionless *i-t* transient for instantaneous and progressive metal nucleation mechanisms.

These dimensionless *i-t* curves were theoretically derived for the instantaneous and progressive mechanisms using equations 1.4.2 and 1.4.3, respectively, where I is the resulting background subtracted current at time t, I_m is the current maximum and t_m is the time at which the current reaches its maximum.[71] These equations are useful in studying metal nucleation processes because they do not contain experimental variables, such as the diffusion coefficient, nucleation density, or nucleation rate.

$$\frac{I^2}{I_m^2} = \frac{1.9542}{t/t_m}\left\{1-\exp\left[-1.2564\left(t/t_m\right)\right]\right\}^2 \qquad (1.4.2)$$

$$\frac{I^2}{I_m{}^2} = \frac{1.2254}{t/t_m}\left\{1-\exp\left[-2.3367\left(t/t_m\right)^2\right]\right\}^2 \qquad (1.4.3)$$

Assuming a potentiostatic deposition was carried out at a sufficiently cathodic potential, the electrodeposition of metal particles onto an electrode surface would be limited by the diffusion of the solvated metal ions from the bulk to the electrode surface. When the ions in the immediate vicinity of the electrode surface are reduced, a volume void of metal ions known as the depletion layer is formed around the metal nucleus. This results in radial diffusion of ions from the bulk to the metal surface. The depletion layer around each individual metal particle grows in thickness with time and eventually neighboring layers begin to overlap and transition the process from 3-dimensional radial diffusion to 2-dimensional diffusion to a planar electrode. This leads to particle agglomeration, which results in the formation of large particles of widely-dispersed size and low density. This model was first demonstrated by Scharifker and Hills and has since become the model of electrodeposition and is illustrated in Figure 1.8.[71] Figure 1.9 shows the same phenomena, but from a top view. Additionally, this illustrates how the rate of deposition increases with increasing deposition overpotential, and hence quicker overlapping between neighboring depletion layers.

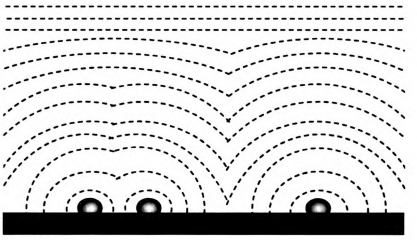

Figure 1.8. Schematic representation of overlapping depletion layers with respect to time. Adapted from Scharifker and Hills.[71]

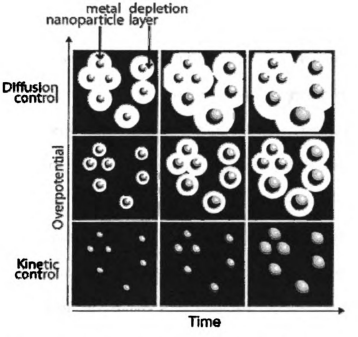

Figure 1.9. Top view of overlapping depletion layers as a function of deposition overpotential and time. Adapted from Penner *et al.*[69,72]

Over the past several years, our group has been investigating the formation of metal adlayers on boron-doped microcrystalline diamond thin films.[64,65,73,74] For example, Wang *et al.* investigated the electrodeposition of Pt using constant current deposition (0.50 mA/cm^2) as a function of time (100-400 s). This resulted in particles 50-300 nm in size and dispersed over the entire surface at an approximate density of 10^8 – 10^9 cm^{-2}.[65] While it was shown that Pt could be stably deposited on the diamond surface using this method, the particles produced were too large to be of practical electrocatalytic use. In addition, several groups including ours have investigated non-electrochemical[63,75,76] and electrochemical metal phase formation on diamond for such purposes as metal ion analysis (*i.e.*, Ag^+, Pb^{2+}, Cu^{2+}, Cd^{2+}, Zn^{2+}, $As^{3+/5+}$ etc.),[21,27,77-81] wastewater remediation,[82] and various electro-catalytic reactions (*e.g.*, H_2 or methanol oxidation and O_2 reduction).[83-85]

A possible alternative to constant potential/current deposition is the application of a pulsed deposition sequence in which the potential/current is applied for short periods of time with dead periods between each pulse. During this dead period, ions diffuse from the bulk to replenish the depletion layer surrounding a metal particle before another pulse is applied. This helps to minimize the overlap of depletion layers from individual particles, thus limiting particle agglomeration and resulting in particles of smaller nominal size and more size-monodispersity. Also, the particle density is increased. Pulsed electrodeposition of metals has been employed for several years to prepare nanometer-sized particles of metals and alloys.[59,66,69,72,86-93] However, metal deposition on diamond is an extremely complicated process that is not yet completely understood.

Unlike most electrode materials used in metal deposition investigations, diamond is quite heterogeneous electronically and structurally.[94] This creates significant challenges in determining the proper deposition parameters (*i.e.*, number of pulses, pulse potential/current magnitude, pulse width, delay time between pulses). It was our supposition at the outset of this research that changing the deposition from a constant current to a pulsed current approach would result in particles with more desirable properties in terms of size, size dispersion, and density while significantly decreasing the metal loading on the electrode surface.

1.5 The Oxygen Reduction Reaction

As mentioned above, electrodes consisting of supported metal catalysts are used in a variety of electrochemical technologies, including electrosynthesis and electrochemical energy conversion (*e.g.*, fuel cells). An example of this is the oxygen reduction reaction (ORR), an important electrochemical reaction because of its relevance in biological systems and energy conversion.[95-106] The ORR can proceed in aqueous electrolytes via two overall pathways: a direct, 4-electron pathway or an indirect, 2-electron pathway.

Carbon electrodes, particularly diamond,[101,102,107] exhibit low activity for ORR as compared to metal electrodes, like Pt. The ORR at carbon electrodes proceeds via the 2-electron pathway in acidic media, as reported by Yeager and shown in equation 1.5.1,[103] producing hydrogen peroxide.

$$O_2 + 2H^+ + 2e^- \rightleftarrows H_2O_2 \quad (E^o = 0.498 \text{ V vs. Ag/AgCl})^{40} \qquad (1.5.1)$$

The ORR at Pt, on the other hand, proceeds with much lower overpotential via the direct, 4-electron pathway in acidic media, as shown in equation 1.5.2, to produce water.

$$O_2 + 4H^+ + 4e^- \rightleftarrows 2H_2O \quad (E^o = 1.032 \text{ V vs. Ag/AgCl})^{40} \qquad (1.5.2)$$

The direct, 4-electron pathway is most desirable, particularly in fuel cells, as it does not involve the formation of peroxide species in solution and the Faradaic efficiency of the reaction is greater (more electrons per molecule). Figure 1.10 compares the ORR in acidic media at diamond to that at Pt. The voltammetric *i-E* curve for the diamond electrode shows a very negative reduction potential of *ca.* -800 mV vs. Ag/AgCl. This corresponds to an overpotential of over 1 V. The *i-E* curve for the polycrystalline Pt electrode however has a much more positive reduction peak potential of *ca.* 450 mV vs. Ag/AgCl. This corresponds to a lower overpotential (*ca.* 500 mV). It is obvious from this that Pt is a much more efficient catalyst for the reaction than diamond. However, due to its considerable expense, there is a desire to achieve the highest catalytic activity at the lowest Pt mass loading. Ideally, a non-Pt-based alternative electrocatalyst for the ORR is desired. There have been numerous investigations of the ORR at solid metal and metal electrocatalyst-supported electrodes,[97-99,103,108-112] but Pt and Pt-based alloys are currently the best electrocatalysts for this reaction.[1,99] As an example, Adzic and coworkers recently developed a procedure which reduces the Pt content to monolayer coverage using a technique which involves the spontaneous replacement of predeposited Cu (upd)

with Pt on Pd nanoparticles. They are also investigating several Pt alloys using the same procedure to further reduce the Pt content.[113-115]

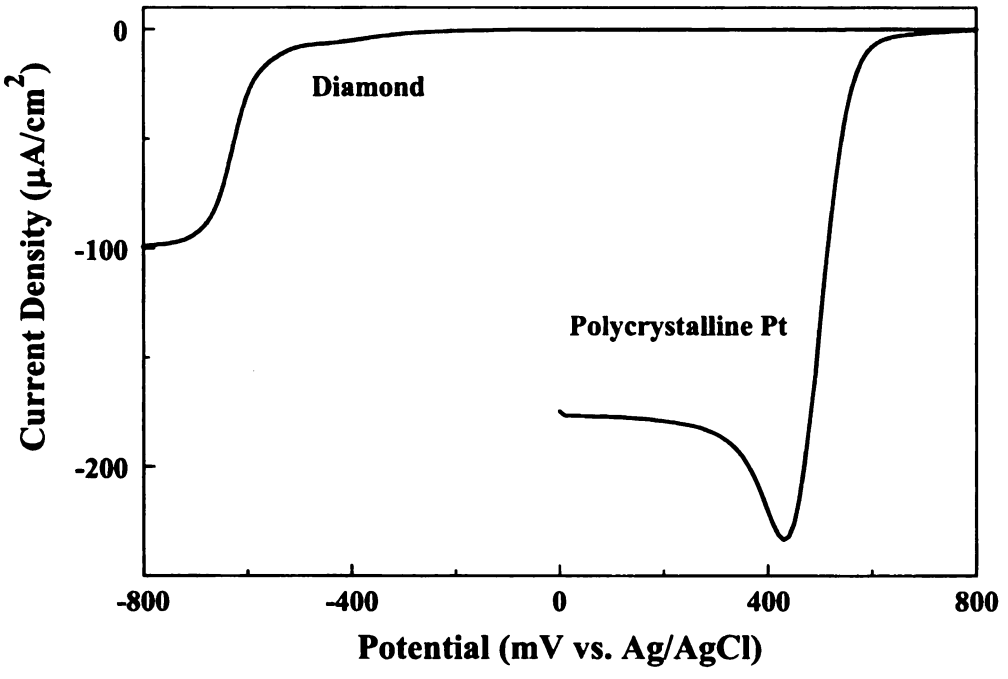

Figure 1.10. Linear sweep voltammetric *i-E* curves for the oxygen reduction reaction (ORR) in 0.1 M $HClO_4$ at boron-doped microcrystalline diamond thin film and polycrystalline Pt. Scan rate = 1 mV/s. Current is normalized to geometric electrode area, 0.2 cm^2.

Kinoshita previously reviewed various oxygen reduction reaction catalysts.[116] However, surging interest in this area for purposes of fuel cells has produced several new potential electrocatalysts. A comparison of several recently published studies on Pt- and non-Pt-based electrocatalysts is presented in Table 1.2.[113,117-121] It is sometimes difficult to directly compare electrocatalyst performance in different reports due to the nature of individual studies, and for this reason, Gasteiger and coworkers recently presented activity benchmarks and requirements for Pt, Pt-alloy, and non-Pt oxygen reduction

catalysts.[6] While Pt and Pt-based alloys are the most active catalysts, state-of-the-art membrane electrode assemblies (MEA) in fuel cells possess Pt loadings of 0.6-0.8 mg_{Pt}/cm^2_{MEA} (Membrane Electrode Assembly) and exhibit power densities of 0.7 W/cm^2_{MEA} at 0.68 V vs. SHE and 80 °C. This translates into a Pt specific power density of 0.85-1.1 g_{Pt}/kW (or 72-94 g of Pt for an ~85 kW stack).[6] In order to satisfy large-scale automotive applications because of cost and supply limitations, the Pt loading must decrease 5-fold and the Pt specific power density must drop below 0.2 g_{Pt}/kW at potentials greater than 0.65 V vs. SHE. Additionally, current specific and mass Pt activities (at 0.9 V vs. SHE) are *ca.* 170-210 $\mu A/cm^2_{Pt}$ and 0.064-0.16 A/mg_{Pt}, respectively. Gasteiger and coworkers point out that if a catalyst was essentially "costless", it could occupy ~20x the volume of the 47% Pt/C cathode catalyst, the activity of which needs to be doubled at a minimum. Therefore, activity of a "costless" cathode needs to be no less than $1/10^{th}$ of the current Pt activity. Table 6 in this reference provides a comparison of several "costless" catalysts.[6]

Table 1.2. Summary of Potential Pt-Based and Non-Pt-Based PEMFC Electrocatalysts Currently Being Investigated

Reference	Electrocatalyst	Experimental Conditions	Conclusions[a]
113	Pt monolayer on metal nanoparticles	0.1 M $HClO_4$, 25 °C	• Mass activity higher than Pt/C by an order of magnitude • Inhibits PtOH formation • $E_{1/2}$ are 25-45 mV more positive than Pt/C
117	Fe-based	PEMFC, 80 °C pure H_2/O_2	• 0.2 Fe wt.% gave highest specific activity • Specific activity ~1000x lower than Pt/C • Specific activity ~ 100x below target of a non-noble catalyst for automotive applications • Could compete with Pt in DMFC because more ORR-selective
118	Pd-Co-Mo (70:20:10)	PEMFC, 60 °C pure H_2/O_2	• Slightly lower ORR activity than Pt/C • More tolerant to CO poisoning • Specific activity max. 4.5 A/m^2 @ 0.7 V (Pt/C = 2) • PEMFC OCP comparable to Pt/C • Cell voltage stable over 80 h at 200 mA/cm^2
119	Pt-FePO	0.1 M $HClO_4$, 60 °C	• Increased ORR activity compared to std. 20 wt.% Pt/C (0.1 mg_{Pt}/cm^2) • 12 wt.% Pt in Pt-FePO • Mass Activity at 0.95 V = 20.5 A/g_{Pt} (Pt/C = 14.3) • Tafel Slope = -74 mV/dec. (Pt/C = -70)
120	Pt-M (M = Fe or Co)	PEMFC, 75 °C pure H_2/O_2	• Particle size (3-8 nm) dependent on M • Both exhibit high activity due to atomic ordering • Pt may be in (100) orientation – most active for ORR
121	Ru-based (Ru_x, Ru_xSe_y, $Ru_xFe_ySe_z$)	PEMFC, 40-80 °C pure H_2/O_2	• OCP = 0.8-0.97 V (Pt = 0.96) • Tafel slope = ~-110 mV/dec. (Pt = -77) • P_{max} = 140 mW/cm^2 at 80 °C (~55% lower than Pt)

[a] – All potentials referenced are vs. SHE

1.6 Dissertation Overview

This dissertation is divided into seven chapters with the research results focused on metal phase formation on diamond and the potential use of diamond as an electrocatalyst support material. In this work, I sought (*i*) to evaluate the potential of microcrystalline and nanocrystalline diamond as an electrocatalyst support material by assessing the physical and electrochemical properties of the material and (*ii*) to understand metal phase formation, specifically Pt, on both microcrystalline and nanocrystalline diamond in an attempt to better control and stabilize electrocatalyst metal particles on the surface. All of the experimental details are reported in Chapter 2, while Chapters 3-6 present the results, discussions and conclusions of the individual investigations. Finally, the complete findings of this work as well as additional areas worth investigating are summarized in Chapter 7.

Chapters 3 and 4 describe some of the basic physical and electrochemical properties of diamond as well as the dimensional stability of the material during exposure to aggressive electrochemical conditions, as these are important for a new support material. As mentioned above, current electrocatalyst support materials are composed of sp^2 carbon. While these materials possess several benefits, they are lacking in physical stability. Chapter 3 reports on the effect of controlled incorporation of sp^2 nondiamond carbon into the diamond microstructure in terms of physical and electrochemical properties. The sp^2 nondiamond carbon is incorporated through increasing the carbon concentration in the growth gas. Chapter 4 assesses the potential use of high quality microcrystalline and nanocrystalline diamond (*i.e.*, low sp^2 nondiamond carbon impurity

content) as an electrocatalyst support material. The microstructural and morphological stability of the material is monitored under conditions typically observed in a PAFC. Specifically, the extent of surface oxidation and morphological degradation was determined to assess whether the material could stably support electrocatalyst particles under harsh conditions.

As discussed previously, our group has published several papers on the deposition of Pt nanoparticles onto the surface of microcrystalline diamond using both DC magnetron sputtering and constant current electrodeposition.[61,62,64,65] However, particles produced by both of these methods were too large for practical application. A comprehensive study of the deposition of nanometer-sized Pt particles using a new deposition approach, pulse galvanostatic deposition, is described in Chapter 5. It was our supposition that this method would better control the metal particle properties in terms of size, size dispersion, density and electrocatalytic activity. Additionally, the first comparison of metal phase formation on two morphologically different types of diamond, microcrystalline and nanocrystalline, is reported.

In an attempt to better understand the particle-diamond interaction, work to examine the effect of the diamond surface chemistry on metal phase formation and stability at both diamond types is described in Chapter 6. Understanding the nature of catalyst loss should aid in our attempt to stabilize the electrocatalyst particles to the diamond surface.

REFERENCES

1. E. Auer, A. Freund, J. Pietsch, and T. Tacke, *Appl. Catal. A: Gen.*, **173**, 259 (1998).

2. A. J. Appleby, in *Comprehensive Treatise of Electrochemistry*, B. E. Conway, J. O. M. Bockris, E. Yeager, S. U. M. Khan, and R. E. White, Editors, **7**, p. 173, Plenum Press, New York, (1983).

3. M. L. Perry and T. F. Fuller, *J. Electrochem. Soc.*, **149**, S59 (2002).

4. U. S. Department of Energy, in *DOE Hydrogen Program - 2005 Annual Progress Report*, (2005).

5. U. S. Department of Energy, in *Basic Research Needs for the Hydrogen Economy: Report of the Basic Energy Sciences Workshop on Hydrogen Production, Storage, and Use*, Argonne National Laboratory, Chicago, IL,150 pages (2003).

6. H. A. Gasteiger, S. S. Kocha, B. Sompalli, and F. T. Wagner, *Appl. Catal. B: Environ.*, **56**, 9 (2005).

7. U. S. Department of Energy - Energy Efficiency and Renewable Energy, in *Hydrogen, Fuel Cells and Infrastructure Technologies Program: Multi-Year Research, Development and Demonstration Plan*, (2003).

8. R. L. McCreery, in *Interfacial Electrochemistry: Theory, Experiment, and Applications*, A. Wieckowski, Editor, p. 631, Marcel Dekker, Inc., New York, (1999).

9. G. M. Swain, in *Electroanalytical Chemistry*, A. J. Bard and I. Rubinstein, Editors, **22**, p. 181, Marcel Dekker, Inc., New York, (2004).

10. A. E. Fischer, Ph. D. Dissertation, *Degradation Mechanisms of Carbon-Based Electrocatalyst Support Materials and Development of an Advanced Support Based on Electrically Conducting Diamond*, Michigan State University, East Lansing, MI, (2005).

11. G. M. Jenkins and K. Kawamura, *Nature (London)*, **231**, 175 (1971).

12. R. L. McCreery, in *Electroanalytical Chemistry*, A. J. Bard and I. Rubinstein, Editors, **17**, p. 221, Marcel Dekker, Inc., New York, (1990).

13. F. Tuinstra and J. L. Koenig, *J. Chem. Phys.*, **53**, 1126 (1970).

14. W. A. Yarbrough and R. Messier, *Science*, **247**, 688 (1990).

15. K. Ushizawa, K. Watanabe, T. Ando, I. Sakagucki, M. Nishitani-Gamo, Y. Sato, and H. Kanada, *Diamond and Rel. Mater.*, **7**, 1719 (1998).

16. D. S. Knight and W. B. White, *J. Mater. Res.*, **4**, 385 (1989).

17. D. H. Karwik, I. F. Hu, S. Weng, and T. Kuwana, *ACS Symp. Ser.*, **288**, 582 (1985).

18. G. W. Hance and T. Kuwana, *Anal. Chem.*, **59**, 131 (1987).

19. J. F. Evans and T. Kuwana, *Anal. Chem.*, **49**, 1632 (1977).

20. J. F. Evans, T. Kuwana, M. T. Henne, and G. P. Royer, *J. Electroanal. Chem.*, **80**, 409 (1977).

21. E. A. McGaw and G. M. Swain, *Anal. Chim. Acta*, **575**, 180 (2006).

22. J. Park, Y. Show, V. Quaiserova, J. J. Galligan, G. D. Fink, and G. M. Swain, *J. Electroanal. Chem.*, **583**, 56 (2005).

23. G. M. Swain, A. B. Anderson, and J. C. Angus, *MRS Bull.*, **23**, 56 (1998).

24. M. Hupert, A. Muck, J. Wang, J. Stotter, Z. Cvackova, S. Haymond, Y. Show, and G. M. Swain, *Diamond and Rel. Mater.*, **12**, 1940 (2003).

25. P. Sonthalia, E. McGaw, Y. Show, and G. M. Swain, *Anal. Chim. Acta*, **522**, 35 (2004).

26. G. W. Muna, V. Quaiserová-Mocko, and G. M. Swain, *Anal. Chem.*, **77**, 6542 (2005).

27. Y. Song, X. Zhao, T. Voice, and G. M. Swain, *Manuscript in preparation.*

28. J. Xu, M. C. Granger, Q. Chen, J. W. Strojek, T. E. Lister, and G. M. Swain, *Anal. Chem.*, **69**, 591A (1997).

29. M. C. Granger and G. M. Swain, *J. Electrochem. Soc.*, **146**, 4551 (1999).

30. J. Wang, G. M. Swain, M. Mermoux, G. Lucazeau, J. Zak, and J. W. Strojek, *New Diamond Front. Carbon Technol.*, **9**, 317 (1999).

31. S. Alehashem, F. Chambers, J. W. Strojek, G. M. Swain, and R. Ramesham, *Anal. Chem.*, **67**, 2812 (1995).

32. J. Asmussen and T. A. Grotjohn, in *Diamond Films Handbook*, J. Asmussen and D. K. Reinhard, Editors, p. 211, Marcel Dekker, Inc., New York, (2002).

33. D. Zhou, D. M. Gruen, L. C. Qin, T. G. McCauley, and A. R. Krauss, *J. Appl. Phys.*, **84**, 1981 (1998).

34. S. Jiao, A. Sumant, M. A. Kirk, D. M. Gruen, A. R. Krauss, and O. Auciello, *J. Appl. Phys.*, **90**, 118 (2001).

35. D. M. Gruen, *MRS Bull.*, **23**, 32 (1998).

36. D. M. Gruen, *Annu. Rev. Mater. Sci*, **29**, 211 (1999).

37. P. K. Bachmann, D. Leers, and H. Lydtin, *Diamond and Rel. Mater.*, **1**, 1 (1991).

38. P. K. Bachmann, H. J. Hagemann, H. Lade, D. Leers, F. Picht, and D. U. Wiechert, *Diamond, SiC, and Nitride Wide Band Gap Semiconductors*, Pittsburgh, PA, C. H. Carter, G. Gildenblatt, S. Nakamura, and R. J. Nemanich, Editors, **339**, p. 267, *MRS Symp Proc.*, Pittsburgh, PA Materials Research Society, (1994).

39. A. J. Appleby, *Corrosion (Houston)*, **43**, 398 (1987).

40. A. J. Bard and L. R. Faulkner, *Electrochemical Methods: Fundamentals and Applications*, John Wiley & Sons, Inc., New York (2001).

41. L. M. Roen, C. H. Paik, and T. D. Jarvi, *Electrochem. Solid-State Lett.*, **7**, A19 (2004).

42. M. F. Mathias, R. Makharia, H. A. Gasteiger, J. J. Conley, T. J. Fuller, C. J. Gittleman, S. S. Kocha, D. P. Miller, C. K. Mittelsteadt, T. Xie, S. G. Yan, and P. T. Yu, *Interface*, **14(3)**, 24 (2005).

43. F. Yuan and H. Ryu, *Nanotechnology*, **15**, S596 (2004).

44. F. Yuan, G. Sasikumar, and H. Ryu, *J. New Mater. Electrochem. Sys.* , **7**, 311 (2004).

45. P. Liu, S.-H. Lee, Y. Yan, T. Gennett, B. J. Landi, A. C. Dillon, and M. J. Heben, *Electrochem. Solid-State Lett.*, **7**, A421 (2004).

46. P. Serp, M. Corrias, and P. Kalck, *Appl. Catal. A: Gen.*, **253**, 337 (2003).

47. J. H. Bitter, M. K. van der Lee, A. G. T. Slotboom, A. J. van Dillen, and K. P. de Jong, *Catal. Lett.*, **89**, 139 (2003).

48. V. Raghuveer and A. Manthiram, *Electrochem. Solid-State Lett.*, **7**, A336 (2004).

49. G. Wang, G. Sun, Z. Zhou, J. Liu, Q. Wang, S. Wang, J. Guo, S. Yang, Q. Xin, and B. Yi, *Electrochem. Solid-State Lett.*, **8**, A12 (2005).

50. J. Ding, K.-Y. Chan, J. Ren, and F.-S. Xiao, *Electrochim. Acta*, **50**, 3131 (2005).

51. A. Smirnova, X. Dong, H. Hara, A. Vasiliev, and N. Sammes, *Int. J. Hydrogen Energy*, **30**, 149 (2005).

52. M. C. Granger, J. Xu, J. W. Strojek, and G. M. Swain, *Anal. Chim. Acta*, **397**, 145 (1999).

53. M. D. Koppang, M. Witek, J. Blau, and G. M. Swain, *Anal. Chem.*, **71**, 1188 (1999).

54. Q. Chen, M. C. Granger, T. E. Lister, and G. M. Swain, *J. Electrochem. Soc.*, **144**, 3806 (1997).

55. G. M. Swain, *J. Electrochem. Soc.*, **141**, 3382 (1994).

56. V. Y. Dolmatov, *Russ. Chem. Rev.*, **70**, 607 (2001).

57. A. E. Fischer and G. M. Swain, *J. Electrochem. Soc.*, **152**, B369 (2005).

58. M. Boutonnet, J. Kizling, P. Stenius, and G. Maire, *Colloids Surf.*, **5**, 209 (1982).

59. J. V. Zoval, J. Lee, S. Gorer, and R. M. Penner, *J. Phys. Chem. B*, **102**, 1166 (1998).

60. Y. Takasu, T. Fujiwara, Y. Murakami, K. Sasaki, M. Oguri, T. Asaki, and W. Sugimoto, *J. Electrochem. Soc.*, **147**, 4421 (2000).

61. J. Wang, G. M. Swain, T. Tachibana, and K. Kobashi, *Electrochem. Solid-State Lett.*, **3**, 286 (2000).

62. J. Wang, G. M. Swain, T. Tachibana, and K. Kobashi, *J. New Mater. Electrochem. Sys.* , **3**, 75 (2000).

63. B. El Roustom, G. Fóti, and C. Comninellis, *Electrochem. Commun.*, **7**, 398 (2005).

64. J. Wang and G. M. Swain, *Electrochem. Solid-State Lett.*, **5**, E4 (2002).

65. J. Wang and G. M. Swain, *J. Electrochem. Soc.*, **150**, E24 (2003).

66. M.-S. Löffler, B. Groß, H. Natter, R. Hempelmann, T. Krajewski, and J. Divisek, *Phys. Chem. Chem. Phys.*, **3**, 333 (2001).

67. E. Budevski, G. Staikov, and W. J. Lorenz, *Electrochemical Phase Formation and Growth*, VCH, New York (1996).

68. E. Budevski, G. Staikov, and W. J. Lorenz, *Electrochim. Acta*, **45**, 2559 (2000).

69. R. M. Penner, *J. Phys. Chem. B*, **105**, 8672 (2001).

70. D. Pletcher, *A First Course in Electrode Processes*, Alresford Press Ltd., U.K. (1991).

71. B. Scharifker and G. Hills, *Electrochim. Acta*, **28**, 879 (1983).

72. H. Liu, F. Favier, K. Ng, M. P. Zach, and R. M. Penner, *Electrochim. Acta*, **47**, 671 (2001).

73. M. Awada, J. W. Strojek, and G. M. Swain, *J. Electrochem. Soc.*, **142**, L42 (1995).

74. J. Wang, Ph.D. Dissertation, *Fabrication, Characterization, And Electrocatalytic Activity of Metal/Diamond Composite Electrodes*, Michigan State University, East Lansing, MI, (2002).

75. G. Siné and C. Comninellis, *Electrochim. Acta*, **50**, 2249 (2005).

76. J.-S. Gao, T. Arunagiri, J.-J. Chen, P. Goodwill, and O. Chyan, *Chem. Mater.*, **12**, 3495 (2000).

77. J. Zak and M. Kolodziej-Sadlok, *Electrochim. Acta*, **45**, 2803 (2000).

78. C. Prado, S. J. Wilkins, P. Gründler, F. Marken, and R. G. Compton, *Electroanalysis*, **15**, 1011 (2003).

79. L. C. Hian, K. J. Grehan, C. H. Goeting, R. G. Compton, J. S. Foord, and F. Marken, *Electroanalysis*, **15**, 169 (2003).

80. M. E. Hyde, R. M. J. Jacobs, and R. G. Compton, *J. Electroanal. Chem.*, **562**, 61 (2004).

81. N. Vinokur, B. Miller, Y. Avyigal, and R. Kalish, *J. Electrochem. Soc.*, **146**, 125 (1999).

82. Y. Zhang, S. Yoshihara, and T. Shirakashi, *Electrochim. Acta*, **51**, 1008 (2005).

83. B. Riedo, G. Dietler, and O. Enea, *Thin Solid Films*, **488**, 82 (2005).

84. O. Enea, B. Riedo, and G. Dietler, *Nano Letters*, **2**, 241 (2002).

85. F. Montilla, E. Morallón, I. Duo, C. Comninellis, and J. L. Vázquez, *Electrochim. Acta*, **48**, 3891 (2003).

86. J. V. Zoval, R. M. Stiger, P. R. Biernacki, and R. M. Penner, *J. Phys. Chem.*, **100**, 837 (1996).

87. J. L. Fransaer and R. M. Penner, *J. Phys. Chem. B*, **103**, 7643 (1999).

88. S. Gorer, H. Liu, R. M. Stiger, M. P. Zach, J. V. Zoval, and R. M. Penner, in *Metal Nanoparticles*, D. L. Feldheim and C. A. Foss Jr., Editors, p. 237, Marcel Dekker, Inc., New York, New York, (2002).

89. R. M. Penner, *J. Phys. Chem. B*, **106**, 3339 (2002).

90. H. Liu and R. M. Penner, *J. Phys. Chem. B*, **104**, 9131 (2000).

91. G. Gunawardena, G. Hills, I. Montenegro, and B. Scharifker, *J. Electroanal. Chem.*, **138**, 225 (1982).

92. P. Allongue and E. Souteyrand, *J. Electroanal. Chem.*, **286**, 217 (1990).

93. H. Kim, N. P. Subramanian, and B. N. Popov, *J. Power Sources*, **138**, 14 (2004).

94. S. Wang and G. M. Swain, *Manuscript in preparation.*

95. L. Carrette, K. A. Friedrich, and U. Stimming, *Fuel Cells*, **1**, 5 (2001).

96. J. Y. Lucisano, J. C. Armour, and D. A. Gough, *Anal. Chem.*, **59**, 736 (1987).

97. A. Damjanovic and V. Brusic, *Electrochim. Acta*, **12**, 615 (1967).

98. N. Giordano, E. Passalacqua, L. Pino, A. S. Aricó, V. Antonucci, M. Vivaldi, and K. Kinoshita, *Electrochim. Acta*, **36**, 1979 (1991).

99. N. M. Markovic, T. J. Schmidt, V. Stamenkovic, and P. N. Ross, *Fuel Cells*, **1**, 105 (2001).

100. H.-H. Yang and R. L. McCreery, *J. Electrochem. Soc.*, **147**, 3420 (2000).

101. T. Yano, E. Popa, D. A. Tryk, K. Hashimoto, and A. Fujishima, *J. Electrochem. Soc.*, **146**, 1081 (1999).

102. T. Yano, D. A. Tryk, K. Hashimoto, and A. Fujishima, *J. Electrochem. Soc.*, **145**, 1870 (1998).

103. E. Yeager, *Electrochim. Acta*, **29**, 1527 (1984).

104. I. Morcos and E. Yeager, *Electrochim. Acta*, **15**, 953 (1970).

105. E. Yeager, J. A. Molla, and S. Gupta, in *Electrochemistry of Carbon*, S. Sarangapani, J. R. Akridge, and B. Schumm, Editors, **PV 84-5**, p. 123, The Electrochemical Society Proceedings Series, Pennington, NJ, (1984).

106. E. Yeager and D. Tryk, in *Proceedings of the 33rd International Power Sources Symposium*, The Electrochemical Society, Inc., Cherry Hill, NJ, (1988).

107. J. A. Bennett, J. Wang, Y. Show, and G. M. Swain, *J. Electrochem. Soc.*, **151**, E306 (2004).

108. B. C. H. Steele and A. Heinzel, *Nature*, **414**, 345 (2001).

109. F. El Kadiri, R. Faure, and R. Durand, *J. Electroanal. Chem.*, **301**, 177 (1991).

110. H. Kita, H.-W. Lei, and Y. Gao, *J. Electroanal. Chem.*, **379**, 407 (1994).

111. T. Abe, G. M. Swain, K. Sashikata, and K. Itaya, *J. Electroanal. Chem.*, **382**, 73 (1995).

112. Z. W. Zhang, D. Tryk, and E. Yeager, in *The Electrochemical Society Extended Abstracts*, **83-2**, p. Abstract 394, Washington, D.C., (October, 1983).

113. J. Zhang, F. H. B. Lima, M. H. Shao, K. Sasaki, J. X. Wang, J. Hanson, and R. R. Adzic, *J. Phys. Chem. B*, **109**, 22701 (2005).

114. J. Zhang, M. B. Vukmirovic, K. Sasaki, A. U. Nilekar, M. Mavrikakis, and R. R. Adzic, *J. Am. Chem. Soc.*, **127**, 12480 (2005).

115. J. Zhang, M. B. Vukmirovic, K. Sasaki, F. Uribe, and R. R. Adzic, *J. Serb. Chem. Soc.*, **70**, 513 (2005).

116. K. Kinoshita, *Electrochemical Oxygen Technology*, John Wiley & Sons, Inc., New York (1992).

117. F. Jaouen, F. Charreteur, and J. P. Dodelet, *J. Electrochem. Soc.*, **153**, A689 (2006).

118. V. Raghuveer, A. Manthiram, and A. J. Bard, *J. Phys. Chem. B*, **109**, 22909 (2005).

119. P. J. Bouwman, W. Dmowski, J. Stanley, G. B. Cotten, and K. E. Swider-Lyons, *J. Electrochem. Soc.*, **151**, A1989 (2004).

120. L. Xiong and A. Manthiram, *J. Electrochem. Soc.*, **152**, A697 (2005).

121. R. G. González-Huerta, J. A. Chávez-Carvayar, and O. Solorza-Feria, *J. Power Sources*, **153**, 11 (2006).

CHAPTER 2

Experimental Methods

2.1 Diamond Thin-Film Deposition

Boron-doped microcrystalline (BMD) and nanocrystalline (BND) diamond thin-film electrodes were deposited using microwave-assisted plasma chemical vapor deposition (CVD; 1.5 kW, 2.54 GHz, Model AX3120, Astex, Inc., Lowell, MA) on highly conducting p-Si(100) substrates (< 0.001 Ω-cm, Virginia Semiconductor, Inc.). The substrates were pretreated by hand polishing on a felt pad for 5 min using a 0-2 μm diameter diamond powder (GE Superabrasives, Worthington, OH) slurried with ultrapure water (18 MΩ). The scratched substrates were then rinsed with ultrapure water and 2-propanol and sequentially cleaned by ultrasonication in acetone, 2-propanol and ultrapure water (5 min each). The clean substrates were dried and examined under an Olympus BX60M optical microscope (Olympus America, Inc.) to check for surface cleanliness. If needed, the substrates were resonicated in acetone until the surface was visibly devoid of polishing debris. This procedure served to microscopically scratch the substrate and embed small diamond particles; both of which served as the initial diamond nucleation sites.

The microcrystalline films were deposited for 10 h using a methane-to-hydrogen (CH_4 in H_2) source gas ratio of 0.50%, except those discussed in Chapter 3, which were deposited using CH_4 in H_2 source gas ratios of 0.3, 0.5, 1, 2, 3, and 5%. The total gas

Fig
No

flow was 200 sccm with the microwave power, pressure and temperature held constant at 1 kW, 45 torr and ~800 °C, respectively. The nanocrystalline films were deposited using gas flow rates of 1, 94 and 5 sccm for CH_4, Ar, and H_2, respectively. These films were grown for 2 h using a microwave power of 800 W, a deposition pressure of 140 torr, and a temperature of ~800 °C. All gases were ultrahigh purity (99.999%) grade (CH_4 and H_2 from AGA Specialty Gas, Cleveland, OH; Ar from BOC Group, Inc., Murray Hill, NJ). The thickness was 3-7 μm for both film types. Figure 2.1 presents a schematic of the CVD reactor used to grow the diamond. Note that the Ar was only used when growing the nanocrystalline film types. The growth conditions for the two types of diamond films and some of the film properties are summarized in Tables 2.1 and 2.2, respectively.

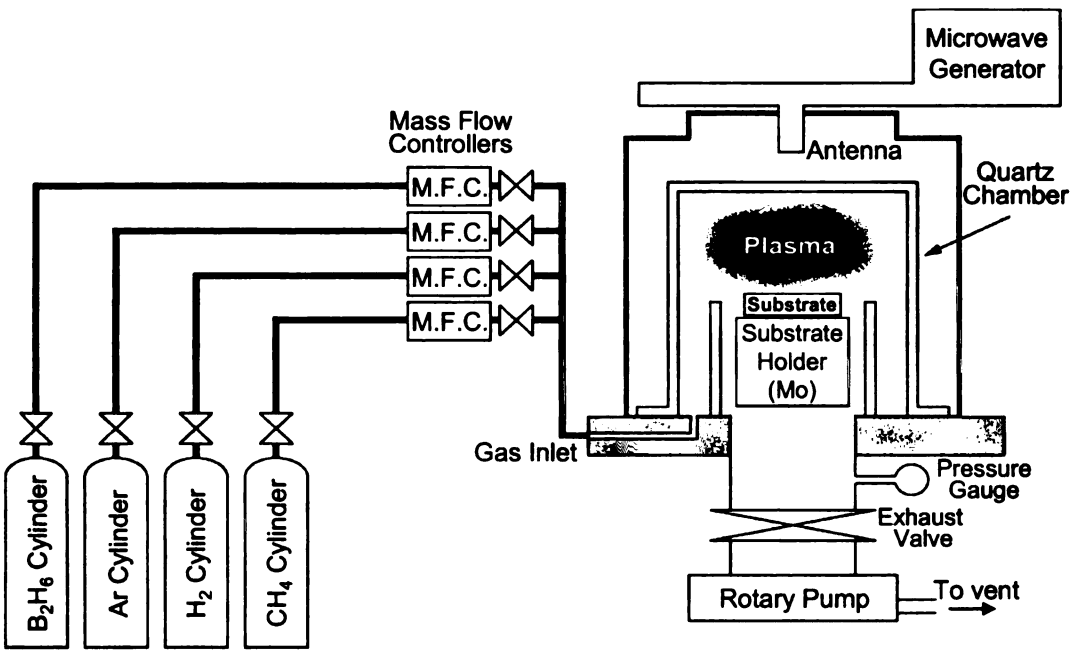

Figure 2.1. Schematic of MPCVD reactor used to grow polycrystalline diamond films. Note Ar was only used for nanocrystalline diamond growth.

Table 2.1. Conditions Used for Microcrystalline and Nanocrystalline Boron-Doped Diamond Thin Film Deposition on Si

Parameter	Microcrystalline	Nanocrystalline
Source Gases (sccm)	CH_4/H_2 (1/199)	CH_4/H_2/Ar (1/5/94)
Methane Concentration	0.5 %	1 %
Dopant	10 ppm B_2H_6 [a]	10 ppm B_2H_6
Microwave Power	1000 W	800 W
Growth Pressure	45 Torr	140 Torr
Substrate Temperature	~800 °C	~800 °C
Growth Time	10 h	2 h

[a] Microcrystalline diamond films discussed in Chapter 3 were doped using a B_2O_3 solid boron diffusion source

Table 2.2. Summary of Physical Properties of Microcrystalline and Nanocrystalline Boron-Doped Diamond Thin Films Deposited on Si

Diamond	Film Thickness (μm)	Resistivity (Ω-cm)	Carrier Concentration (B/cm^3)	Carrier Mobility ($cm^2/V\ s$)
Microcrystalline	~5-7	~0.001	~5×10^{19}	*ca.* 5
Nanocrystalline	~4-6	~0.002	~5×10^{20}	*ca.* 0.5

The microcrystalline diamond films, discussed in Chapter 3, that were deposited using varying CH_4/H_2 source gas ratios were doped using a solid boron diffusion source, B_2O_3 (GS-126, BoronPlus, Techniglas, Inc., Perrysburg, OH).[1] After these films were grown, our group switched to a gaseous source of boron, B_2H_6. Both the microcrystalline and nanocrystalline diamond films discussed in the subsequent chapters were doped from the gas phase by adding 10 ppm B_2H_6 (0.1% B_2H_6 diluted in H_2, Matheson Gas Products, Inc.) to the source gas mixture. The actual flow of B_2H_6 into the growth chamber was 2.0

sccm for microcrystalline and 1.0 sccm for nanocrystalline. However, the actual boron concentration incorporated into the film is much higher. Figures 2.2 and 2.3 show plots relating the B_2H_6 concentration in the source gas to the actual boron concentration in the thin-film determined using boron nuclear reaction analysis (•) and the film resistivity determined using 4-pt. probe measurements (✳) for microcrystalline and nanocrystalline diamond thin films, respectively. The film resistivity was calculated using equation 2.1.1 where R is the resistivity (in Ω-cm), t is the film thickness in cm (estimated to be 0.0006 and 0.0005 cm for microcrystalline and nanocrystalline, respectively) and r is the resistance measured using a 4-pt. probe. The reactor was thoroughly cleaned prior to any diamond growth via acetone-soaked KimWipes and having the quartz chamber dipped in an HF bath and baked to minimize residual boron in the reactor.

$$R = 4.532tr \qquad (2.1.1)$$

It is obvious from the plots that the actual amount of boron incorporated into each type of diamond film is larger than the gas phase concentration despite growing inside a clean reactor. We also measured the thin-film boron concentration and resistivity for 10 ppm films grown several months later after many diamond growths in order to have a better understanding of the types of films used in our studies. The microcrystalline film exhibited a [B] of 2036 ppm and a 4-pt. resistivity of ~0.001 Ω-cm. The nanocrystalline film exhibited a [B] of 906 ppm and a resistivity of ~0.002 Ω-cm.

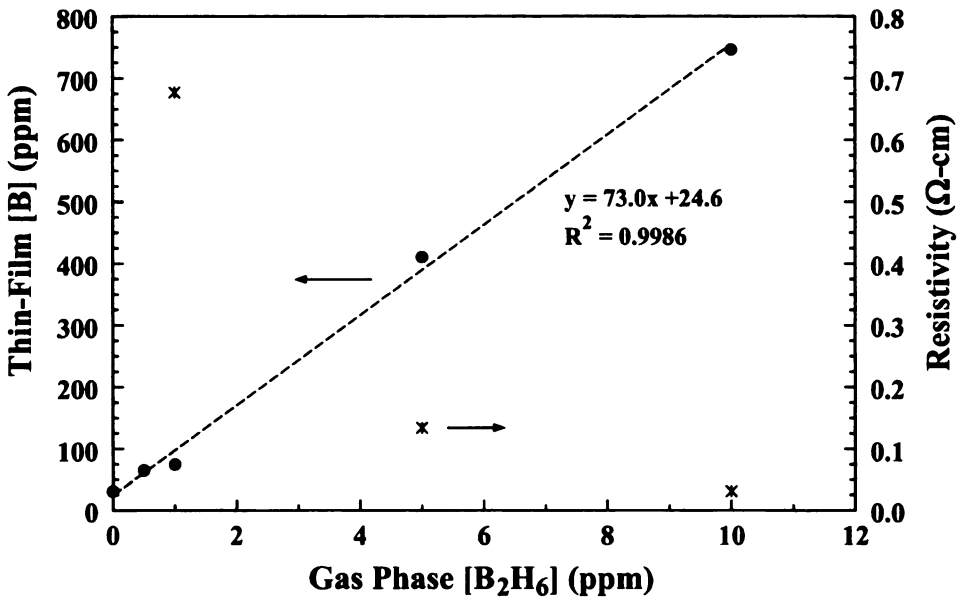

Figure 2.2. Plot relating the concentration of B_2H_6 in the gas phase to that incorporated into the microcrystalline diamond thin-film (•) and the film resistivity (✳).

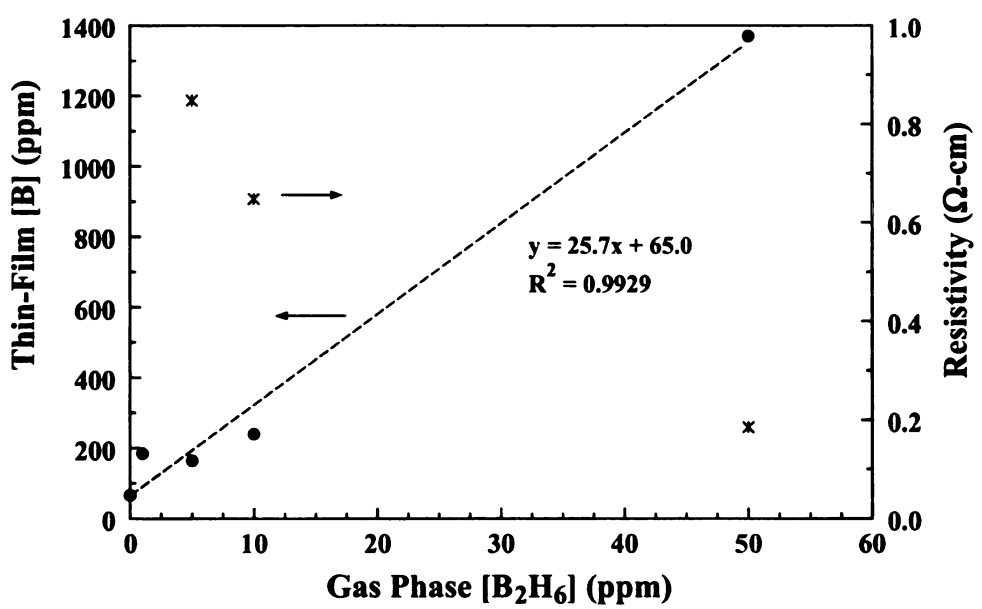

Figure 2.3. Plot relating the concentration of B_2H_6 in the gas phase to that incorporated into the nanocrystalline diamond thin-film (•) and the film resistivity (✳).

Following the deposition, the CH_4 and B_2H_6 flows were stopped, and the films remained exposed to the H_2 (microcrystalline) or H_2/Ar (nanocrystalline) plasma for an additional 10 min. They were then gradually cooled over several minutes to less than 400 °C in the presence of atomic hydrogen by reducing the microwave power and system pressure. This post-growth annealing in atomic hydrogen served to etch away adventitious nondiamond sp^2 carbon impurity, minimize dangling bonds, and ensure maximum hydrogen termination. Both film types had a nominal boron dopant concentration of *ca.* 10^{20} B/cm^3 and a film resistivity of < 0.005 Ω-cm.

2.2 Electrochemical Methods

2.2.1 Electrochemical Measurements

All electrochemical measurements were performed at room temperature in a single compartment glass cell using either a CH Instruments Model 650A or 650B Electrochemical Workstation (CH Instruments, Inc., Austin, TX). The design of the electrochemical cell was reported previously and is shown in Figure 2.4.[2] The diamond electrodes were clamped against the bottom of a glass cell. A Viton™ O-ring was used to define the exposed geometric area, 0.2 cm^2. All currents were normalized to this geometric area unless otherwise noted. In aqueous media, a Ag/AgCl reference electrode was positioned in close proximity to the working electrode using a cracked-glass capillary filled with 4 M KCl. All potentials reported herein are referenced to this electrode. A large-area carbon rod served as the auxiliary electrode and was positioned normal to the working electrode. In non-aqueous media, a Ag/Ag$^+$ quasi-reference electrode (QRE) was used in conjunction with a Pt foil auxiliary electrode. Electrical

contact was made to the diamond working electrode by scratching the backside of the Si substrate with a diamond scribe and then cleaning and coating the area with graphite from a rod. The graphite-coated substrate was then placed in contact with a Cu plate current collector. Once mounted in the cell, the electrode surface was typically cleaned by soaking in distilled 2-propanol for 20 min.[3]

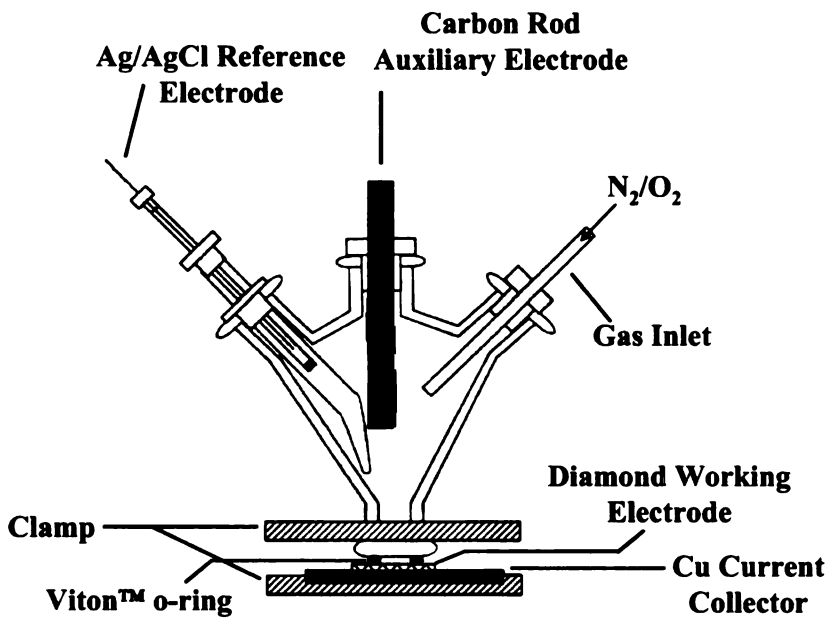

Figure 2.4. Schematic of the single compartment electrochemical cell used in the experiments.

2.2.2 Pulsed Galvanostatic Deposition of Pt

After evaluating an electrode's response for several well known redox systems, the cell was thoroughly rinsed with ultrapure water and filled with 1 mM potassium hexachloroplatinate (IV) (98%, Aldrich) dissolved in 0.1 M $HClO_4$. The solution was purged with N_2 for 20 min prior to deposition. Nanometer-sized Pt particles were deposited under an N_2 blanket using the pulsed galvanostatic method. The hardware

consisted of a homemade galvanostat, configured from an OMNI 90 potentiostat (Cypress Systems, Inc., Lawrence, KS) that was interfaced with a PCI-5401 signal generating controller board (National Instruments, Austin, TX). A block diagram of the instrument is shown in Figure 2.5. Note that the electrochemical cell only has the diamond working electrode and carbon rod auxiliary electrode exposed to the solution. The pulse generation was computer-controlled using National Instruments LabVIEW software (version 6.1). The LabVIEW code for the potential pulsing program can be found in Appendix A. All potential pulses were 1 s in length with a 1 s delay time between each, yielding a 50% duty cycle (pulse time/period). A constant current (pulsed format) was delivered to the cell by applying the voltage (outputted from the PCI-5401 card) between the working and reference OMNI 90 leads across a precision resistor. The pulse number and current density were systematically investigated to determine the optimum deposition conditions in terms of nominal metal particle size and density.

After the Pt was deposited, the galvanostat was disconnected and the platinate solution was removed. This was followed by a gentle rinse of the cell with ultrapure water that was applied by flowing down the sides of the glass cell. Metal particles are sometimes weakly attached to the hydrogen-terminated diamond surface and vigorous rinsing can result in significant metal phase loss.[4,5] The cell was then filled with a fresh 0.1 M $HClO_4$ solution, again by pouring the solution down the sides of the cell, and purged with N_2 for 30 min. The gas was introduced far enough from the surface so as to not disturb the catalyst particles. Under the N_2 blanket, the potential was cycled 10 times between -200 and 1300 mV vs. Ag/AgCl at a rate of 50 mV/s to clean the Pt deposits.

The potential was kept within this window to avoid significant gas evolution, which can physically dislodge the particles.[4,5] The voltammetric *i-E* curve usually stabilized within 5 cycles. The voltammetric charge for H^+ adsorption was used to determine the electrochemically-active Pt surface area, assuming a 1H:1Pt surface interaction and a coulombic charge of 210 $\mu C/cm^2$ for hydrogen adsorption on an atomically flat Pt(111) surface.[6-8]

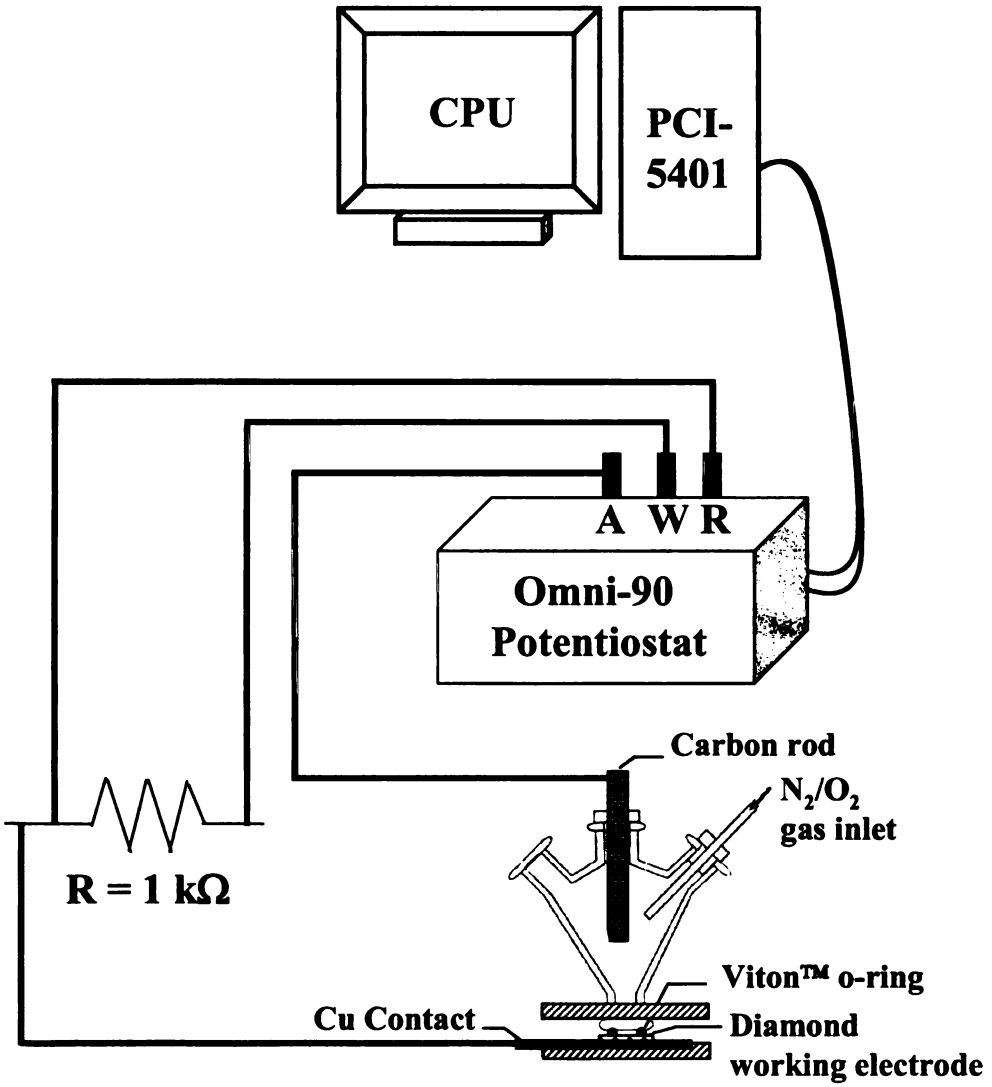

Figure 2.5. Experimental set-up used for pulsed galvanostatic deposition of Pt.

2.2.3 Reagents

2.2.3.1 Aqueous Solutions

All chemicals were reagent-grade quality or better and used without additional purification. The electrochemical response of the electrodes was assessed using some or all of the following: 1 mM solutions of potassium ferrocyanide ($Fe(CN)_6^{3-/4-}$, Aldrich), hexaammineruthenium (III) chloride ($Ru(NH_3)_6^{3+/2+}$, Aldrich), 4-*tert*-butylcatechol (4-*t*BC, Aldrich), and ferric sulfate ($Fe^{3+/2+}$, Fisher) prepared fresh daily. The supporting electrolyte was either 1 M KCl (Spectrum) or 0.1 M $HClO_4$ (redistilled, 99.999%, Aldrich). The oxygen reduction reaction measurements were performed in either 0.1 M $HClO_4$ (C and Pt/C) or 0.1 M NaOH (C only) after purging the solution with O_2 for 30 min.

2.2.3.2 Non-aqueous Solutions

The films were exposed to either 1 mM 4-nitrobenzenediazonium tetrafluoroborate (4-NBD) (97%, Aldrich) or 4-methoxybenzediazonium tetrafluoroborate (4-MBD) (98%, Aldrich) dissolved in 0.1 M tetrabutylammonium tetrafluoroborate (NBu_4BF_4) (99%, Aldrich) plus acetonitrile (ACN). The 4-NBD salt was recrystallized following a procedure presented previously.[9] The salt was dissolved in cold ACN (0 °C) and recrystallized by adding cold (0 °C) diethyl ether. The crystals were then collected via vacuum filtration, allowed to dry, placed in a glass vial and purged with N_2. The vial was then sealed and placed in a freezer for storage. The 4-MBD salt was used as received and, after opening, was also stored in a freezer.[10] The NBu_4BF_4 salt was purified by dissolving in ethyl acetate and precipitating one time using

pentane. The salt was collected and dried at *ca.* 120 °C overnight (>10 h) under vaccum.[11] The ACN was dried using 3 Å molecular sieves that were activated by heating at 300 °C for 15 h followed by cooling in a dessicator. The ACN was treated with the activated sieves (5-10% w/v) for several days and then transferred to a clean amber bottle and allowed to stand over a second batch of molecular sieves.[11]

2.3 Physical Characterization Methods

The physical properties of the microcrystalline and nanocrystalline diamond films were routinely monitored using atomic force microscopy (AFM), scanning electron microscopy (SEM), Raman spectroscopy, and powder X-ray diffraction spectroscopy.

2.3.1 Atomic Force Microscopy

2.3.1.1 Contact Mode AFM

The film morphology was investigated by AFM using a Nanoscope III instrument (Veeco Metrology Group, Inc., Santa Barbara, CA) operated in the contact mode. Pyramidal-shaped Si_3N_4 tips, mounted on gold cantilevers (100 mm legs, 0.38 N/m spring constant), were used in air to acquire the topographical images.

2.3.1.2 Conductive Probe-AFM (CP-AFM)

CP-AFM measurements were performed by Shiua Wang in our group using a NanoScope IIIa instrument (Veeco Instruments, CA). A Au-coated silicon tip was used in the contact mode. A homemade electrical circuit was used to measure the current flowing between the conductive tip and the electrode surface as the tip was rastered over

an area. The diamond samples were placed on a metal stage and electrical contact was made to the bottom of the conducting Si substrate using carbon tape. A bias voltage of either ±0.2 or ±2 V was applied between the tip and the substrate. Conductivity maps were generated simultaneously with the topographical images.

2.3.2 Scanning Electron Microscopy

The films were also physically characterized using either a JSM-6400V (LaB_6) or JSM-6300F (field emission) scanning electron microscope (JEOL LTD., Tokyo, Japan, Center for Advanced Microscopy at MSU). Micrographs were recorded using both secondary and backscattered electrons generated with an accelerating voltage of 10 or 20 kV. Particle analysis was performed with the AnalySIS imaging software (Software Imaging System Corp., Lakewood, CO). In the cases where Pt deposition was investigated, the presence of Pt was verified by energy dispersive x-ray (EDX) analysis (Noran Instruments Inc., Middleton, WI) in conjunction with the JSM-6400V.

2.3.3 Raman Spectroscopy

The film microstructure was studied using Raman spectroscopy. Spectra were acquired at room temperature using a Chromex RAMAN 2000 spectrograph (Chromex, Inc., Albuquerque, NM) consisting of a diode-pumped, frequency-doubled CW Nd:yttirium aluminum garnet (YAG) laser (500 mW at 532 nm, COHERENT), a Chromex 500is spectrometer (f/4, 600 grooves/mm holographic grating, 50 μm slit width), and a thermoelectrically cooled, 1024 x 256 element charge-coupled device (CCD) detector (ANDOR Tech., Ltd.). Spectra were collected with an incident power

density of *ca.* 500 kW/cm^2 (100 mW at the sample and a 5 μm diameter spot size), a 10 s integration time and an approximate spectral resolution of 4 cm^{-1}. A white-light spectrum was collected and used as the background for spectral correction.

2.3.4 X-ray Diffraction Spectroscopy (XRD)

The crystallinity of diamond films grown using different CH_4/H_2 source gas ratios was investigated using powder XRD. Spectra were obtained by scanning 2θ from 20 to 100° on a Rikagu Rotaflex RTP300 RC instrument. X-rays were produced at 1.540 Å from a Cu anode.

2.4 Chapter-Specific Experimental Methods

2.4.1 Chapter 3

This chapter describes an investigation into the effect of nondiamond sp^2 carbon impurity on the physical and electrochemical response of diamond thin-film electrodes. The electrochemical measurements were performed in a single compartment glass cell as described above and shown in Figure 2.2. Once mounted in the cell, the electrode surface was cleaned by soaking in distilled 2-propanol for 10 min. All measurements were performed at room temperature. Prior to the oxygen reduction reaction (ORR) measurements, the solution was saturated with O_2 (99.5% purity, BOC Group, Inc., Murray Hill, NJ) by bubbling the gas through the solution for 20 min. All other cyclic voltammograms (CVs) were obtained after solution degassing with bubbling N_2 for 15 min and then maintaining a blanket of N_2 over the solution during the measurements.

2.4.2 Chapter 4

This chapter presents an investigation of the microstructural stability of both microcrystalline and nanocrystalline diamond thin films during exposure to harsh conditions similar to those of a phosphoric acid fuel cell (PAFC). The electrode was mounted in the single compartment electrochemical cell, as described above. The electrode surface was first rinsed copiously with ultrapure H_2O and then the cell was filled with 85 wt% H_3PO_4 (99.999+%, Aldrich) and heated to *ca.* 180-185 °C using heating tape connected to a variac. The heating was performed in a ventilated hood, and the instrumentation was covered with cling wrap to keep the corrosive vapor out of the lab and instrumental circuitry. The set-up was insulated with cotton and aluminum foil to maintain temperature consistency. Upon reaching the desired temperature, +20 mA of current (or 0.1 A/cm^2) was applied for 2 h. After 2 h, the solution was allowed to cool to room temperature. The cell was then emptied and rinsed thoroughly with ultrapure water.

In addition to probing the cyclic voltammetric background current in N_2-saturated 0.1 M $HClO_4$, the electrode response toward several well known redox systems ($Fe(CN)_6^{-3/-4}$, $Ru(NH_3)_6^{+3/+2}$, and $Fe^{+3/+2}$) was evaluated before and after the anodic polarization.[2,12,13]

The extent of surface oxidation was assessed from contact angle measurements performed with a FTÅ200 (first ten angstroms) contact angle analyzer. Ultrapure H_2O with a drop volume of 10 μL was used and both the left and right contact angles between

the drop and the diamond surface were measured in triplicate. The reported value is the average of these 6 values.

2.4.3 Chapter 5

This chapter presents an in-depth investigation into the nucleation mechanism of Pt on different diamond surfaces. The electrodes were mounted in the single compartment electrochemical cell shown in Figure 2.2. Chonoamperometric *i-t* curves were obtained at applied overpotentials (η) ranging from -312 to -1012 mV based on the redox reaction shown in 2.4.1.[14]

$$PtCl_6^{2-} + 2e^- \rightleftarrows PtCl_4^{2-} + 2Cl^- \qquad (E^o = 530 \text{ mV vs. Ag/AgCl}) \qquad (2.4.1)$$

This value is used as the reduction potential even though, as shown, the reduction does not proceed to Pt^0. However, as shown in equation 2.4.2, the next step in the reduction process occurs at a more positive reduction potential.[14] Therefore, we assume that once the initial 2 electrons are transferred, the reduction quickly proceeds to completion.

$$PtCl_4^{2-} + 2e^- \rightleftarrows Pt^0 + 4Cl^- \qquad (E^o = 561 \text{ mV vs. Ag/AgCl}) \qquad (2.4.2)$$

The resulting chronoamperometric *i-t* curves were then compared to those predicted by Scharifker and Hills for instantaneous and progressive nucleation.[15]

This chapter also contains a discussion of the effect of the pulse parameters (*i.e.*, pulse number and current density) and diamond film morphology on the particle size, shape and dispersion. Glassy carbon was used for comparison measurements. The electrode (GC-30, Tokai, Ltd., Japan) was manually polished on separate felt polishing cloths using aqueous slurries of 1.0, 0.3 and 0.05 μm diameter deagglomerated alumina powder (Buehler, Ltd., Lake Bluff, Il). After each polishing step, the electrode was copiously rinsed with ultrapure water and ultrasonically cleaned in this medium for 10-15 min. After the final polishing and sonication step, the electrode was dried in a stream of N_2 and placed in the electrochemical cell where it was exposed to distilled 2-propanol for 10 min as a final cleaning step.

Atomic absorption spectroscopy (AAS) was used to determine the catalyst loading for a given set of deposition conditions. For these measurements, the Pt particles were deposited onto a separate set of diamond films as a function of the current density and pulse number. After deposition, the Pt metal was then dissolved from the electrode by soaking for 1 h in 4 mL of warm aqua-regia, which consisted of 3 mL HCl (36.5 – 38.0%, Columbus Chemical Industries, Inc., Columbus, WI) and 1 mL HNO_3 (70%, Columbus Chemical Industries, Inc., Columbus, WI). Pt is known to dissolve in warm aqua-regia, while the diamond lattice is quite stable in this solution and undergoes no morphological alteration.[16,17] Upon cooling to room temperature, the electrode was removed from the solution and rinsed thoroughly with ultrapure water. The rinses were collected and mixed with the original solution to collect all the dissolved metal. The total solution volume was 50 mL. AAS was performed directly on this solution using a

Hitachi Z-9000 Atomic Absorption Spectrophotometer (Hitachi, Ltd., Tokyo, Japan) with a graphite tube furnace. The metal ion concentration in each solution was determined from multiple measurements in order to estimate the metal loading.

2.4.4 Chapter 6

This chapter describes the effect of surface chemistry on the formation of Pt metal phases on microcrystalline and nanocrystalline diamond. Four different surface chemistries were investigated: H-terminated, chemically oxidized and modified with aryl-adlayers using either 4-nitrobenzene or 4-methoxybenzene diazonium salts.

The oxygen-terminated microcrystalline (BMD_{ox}) and nanocrystalline (BND_{ox}) films were prepared by gentle refluxing in warm aqua-regia (3:1 $HCl:HNO_3$) for 30 min followed by refluxing in 30% H_2O_2 for 30 min and cooling in air to room temperature. This procedure introduces oxygen functionalities on the surface while leaving the bulk microstructure of the diamond unaltered. X-ray photoelectron spectroscopy was performed by Wayne Jennings at Case Western Reserve University and used to quantify the O/C ratio of the diamond. The H-terminated microcrystalline and nanocrystalline diamond surfaces both exhibited an atomic O/C ratio of *ca.* 0.05 as some oxygen is slowly picked up during air exposure. Assuming that 5 layers of carbon were sampled (*ca.* 5×10^{15} atoms/layer), this ratio corresponds to a surface coverage of approximately 25% of a monolayer.[18] However, atomic O/C ratios of *ca.* 0.13 and 0.10 were observed for the oxidized microcrystalline and nanocrystalline diamond surfaces, respectively. This corresponds to a surface coverage of 65 and 48% of a monolayer, respectively, for

the two diamond surfaces. Therefore, the diamond surfaces possess approximately 2 – 3 times more surface oxygen following the chemical oxidation treatment.

The diazonium modified surfaces were prepared using a well known electrochemical reduction procedure.[19,20] The overall modification process for the two diazonium salts used is depicted in Scheme 2.1. H-terminated diamond films were mounted in the single compartment electrochemical cell presented in Figure 2.2. A CHEMRAZ® o-ring (Greene, Tweed & Co., Inc., Kulpsville, PA) was used to confine the solution and define the electrode area of 0.2 cm^2. The films were exposed to the non-aqueous solutions described above and the surface modification was performed by cycling the potential once from 600 mV to a value slightly negative of the diazonium reduction peak (-600 or -1300 mV for 4-NBD and 4-MBD, respectively). A Ag/Ag^+ quasi-reference (QRE) and Pt foil counter electrode were used, and the potential sweep rate was 200 mV/s. After modification, the cell was thoroughly rinsed with clean ACN and a cyclic voltammogram was obtained after filling the cell with the NBu_4BF_4/ACN electrolyte solution. The 4-NBD modified surface exhibited a reversible couple for the $1e^-$ redox reaction to form $NO_2^{\bullet-}$ at *ca.* -1200 mV indicating that the diamond surface had indeed been modified. These films will be denoted as $BMD_{4\text{-}NBD}$ and $BND_{4\text{-}NBD}$. The 4-MBD modified electrode showed a single reduction peak at *ca.* -900 mV, again signifying that the diamond surface had indeed been modified. In either case, the cell was then sequentially rinsed with ACN, a 50/50 ACN/ultrapure H_2O mixture and ultrapure H_2O.

The 4-MBD modified surface underwent an additional modification step to change the charge of the diamond surface. This procedure was presented by Yan and coworkers and is illustrated in Scheme 2.1.[10] The cell containing the 4-MBD modified electrode was filled with conc. H_2SO_4 (98%, Columbus Chemical Industries, Inc., Columbus, WI) and heated to ~80 °C. Once 80 °C was reached, the temperature was held constant for 1 hr. According to Yan and coworkers, this results in the addition of sulfonic acid groups to the ring at the ortho positions to the methoxy group.[10] After an hour, the solution was allowed to cool to room temperature. The cell was then emptied, rinsed copiously with ultrapure water, and filled with the Pt salt solution for the metal phase formed as described above.

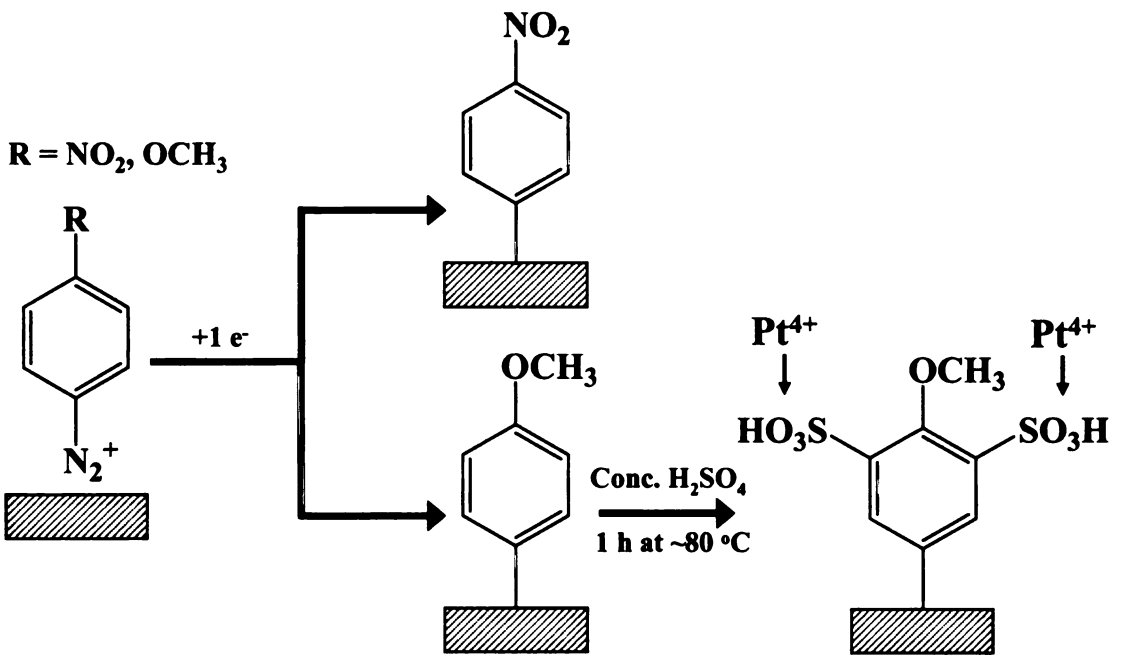

Scheme 2.1. Diazonium surface modification process. The potential was cycled once from 600 to either -600 (4-NBD) or -1300 mV (4-MBD) vs. Ag/Ag^+ QRE at a rate of 200 mV/s. The 4-MBD modified diamond surface was then exposed to concentrated H_2SO_4 for 1 h at a temperature of ~ 80 °C.

REFERENCES

1. J. A. Bennett, J. Wang, Y. Show, and G. M. Swain, *J. Electrochem. Soc.*, **151**, E306 (2004).

2. M. C. Granger, M. Witek, J. Xu, J. Wang, M. Hupert, A. Hanks, M. D. Koppang, J. E. Butler, G. Lucazeau, M. Mermoux, J. W. Strojek, and G. M. Swain, *Anal. Chem.*, **72**, 3793 (2000).

3. S. Ranganathan, T.-C. Kuo, and R. L. McCreery, *Anal. Chem.*, **71**, 3574 (1999).

4. N. Vinokur, B. Miller, Y. Avyigal, and R. Kalish, *J. Electrochem. Soc.*, **146**, 125 (1999).

5. S. Nakabayashi, D. A. Tryk, A. Fujishima, and N. Ohta, *Chem. Phys. Lett.*, **300**, 409 (1999).

6. J. Perez, A. A. Tanaka, E. R. Gonzalez, and E. A. Ticianelli, *J. Electrochem. Soc.*, **141**, 431 (1994).

7. A. Essalik, K. Amouzegar, and O. Savadogo, *J. Appl. Electrochem.*, **25**, 404 (1995).

8. J. M. D. Rodríguez, J. A. H. Melián, and J. P. Peña, *J. Chem. Ed.*, **77**, 1195 (2000).

9. A. O. Solak, L. R. Eichorst, W. J. Clark, and R. L. McCreery, *Anal. Chem.*, **75**, 296 (2003).

10. M. M. Waje, X. Wang, W. Li, and Y. Yan, *Nanotechnology*, **16**, S395 (2005).

11. A. J. Fry, in *Laboratory Techniques in Electroanalytical Chemistry: Second Edition, Revised and Expanded*, P. T. Kissinger and W. R. Heineman, Editors, Marcel Dekker, Inc., New York, (1996).

12. Y. Show, M. A. Witek, P. Sonthalia, and G. M. Swain, *Chem. Mater.*, **15**, 879 (2003).

13. A. E. Fischer, Y. Show, and G. M. Swain, *Anal. Chem.*, **76**, 2553 (2004).

14. A. J. Bard and L. R. Faulkner, *Electrochemical Methods: Fundamentals and Applications*, John Wiley & Sons, Inc., New York (2001).

15. B. Scharifker and G. Hills, *Electrochim. Acta*, **28**, 879 (1983).

16. J. Wang and G. M. Swain, *Electrochem. Solid-State Lett.*, **5**, E4 (2002).

17. J. Wang and G. M. Swain, *J. Electrochem. Soc.*, **150**, E24 (2003).

18. G. M. Swain, in *Electroanalytical Chemistry*, A. J. Bard and I. Rubinstein, Editors, **22**, p. 181, Marcel Dekker, Inc., New York, (2004).

19. M. Delamar, R. Hitmi, J. Pinson, and J. M. Savéant, *J. Am. Chem. Soc.*, **114**, 5883 (1992).

20. J. Pinson and F. Podvorica, *Chem. Soc. Rev.*, **34**, 429 (2005).

CHAPTER 3

Effect of sp^2-Bonded Nondiamond Carbon Impurity on Boron-Doped Polycrystalline Diamond Thin-Film Electrodes

3.1 Introduction

Research in our group is focused on understanding how the physical, chemical and electronic properties of boron-doped diamond thin films affect the electrode response in both aqueous and nonaqueous media.[1-7] Several factors can influence the electrode response (*i.e.*, electrode reaction kinetics): potential-dependent density of electronic states, surface chemistry, morphology and microstructure, defect density, nondiamond sp^2 carbon impurity content and double-layer structure.

Common to all electrodes is the fact that the rate of heterogeneous electron transfer is influenced, among other things, by the density of electronic states (DOS) at a given potential. The surface concentration of electrons is important for reduction reactions, while the concentration of unoccupied states (*i.e.*, acceptors) is important for oxidations.[8] For metals, the number of electronic states available at the surface is greater than the number of molecules in solution being electrolyzed, therefore, electron transfer rates being limited by DOS is not an issue. However, the number of charge carriers for semiconductor electrodes can be of the same order of magnitude as the number of molecules in solution, and therefore, is a factor that will limit the current flow (*i.e.*, rate

of reaction). The density of states (DOS) for chemical vapor deposited (CVD) diamond is influenced in a complex manner by the boron-doping level, lattice hydrogen, adventitious nitrogen impurity, nondiamond sp^2 carbon impurity and the defect density. Undoped diamond films deposited by CVD, using conventional CH_4/H_2 source gas mixtures, are generally electrically insulating, if they are free of significant levels of nondiamond carbon and lattice hydrogen. However, incorporated nondiamond carbon impurity can function electronically by providing charge carriers and pathways of high carrier mobility and/or physically by catalyzing redox reactions, providing adsorption sites for reactant and reaction intermediates, providing sites for the formation of carbon-oxygen functionalities and modifying the electrode double-layer structure.

The electrochemical properties of polycrystalline CVD diamond have been investigated in some detail in recent years.[1-4,6,7,9-13] These electrodes can be viewed as having a composite architecture consisting of micrometer-sized grains, or crystallites, of sp^3-bonded carbon (nanometer-sized grains for nanocrystalline diamond), incorporated dopant atoms such as boron, extended and point defects and grain boundaries where sp^2-bonded carbon can form. The deposition conditions are usually selected to minimize the incorporation of sp^2-bonded nondiamond carbon impurity; however, this impurity can be introduced in a controlled manner by adjusting the deposition conditions. Presently, the sp^2-bonded carbon was introduced by increasing the CH_4/H_2 source gas mixture used to deposit the films. Increasing this ratio generally leads to more impurity incorporation. It has been known for some time that the cyclic voltammetric background current increases and the working potential window for aqueous electrolytes decreases with increasing sp^2-

bonded nondiamond carbon content.[2,3,7,9] However, there has been no systematic study of how the electrode response toward various solution redox analytes is affected by the incorporation of the impurity. One study by Scherson and coworkers showed the positive influence of nondiamond carbon impurity on solvent reduction processes in lithium-ion battery solvents.[14] In another more recent work, Duo *et al.* attempted to study the effect of sp^2-carbon impurity by mechanically abrading diamond with graphite particles.[15] Our films have the nondiamond carbon impurity incorporated into the diamond matrix, and this is far different from simply placing graphite particles on the surface. In related work, Shi and coworkers have deposited N-incorporated amorphous carbon films that have a mixed sp^3/sp^2 microstructure.[16] The sp^2 carbon domains play a key role in the electrode activity.

The effect of nondiamond sp^2-bonded carbon impurity on the physical and electrochemical properties of boron-doped diamond electrodes fabricated by CVD is reported on herein. Several aqueous-based redox analytes [$Fe(CN_6)^{3-/4-}$, $Ru(NH_3)_6^{3+/2+}$, $Fe^{3+/2+}$, 4-*tert*-butylcatechol (4-*t*BC), and O_2/H_2O_2] were used to evaluate the electrode response. The electrodes were comprehensively characterized by *ex situ* atomic force microscopy (AFM), scanning electron microscopy (SEM), Raman and powder X-ray diffraction spectroscopy, and voltammetric methods of analysis. The results demonstrate that for some redox analytes, nondiamond carbon impurity has a relatively minor effect, while for others, like the oxygen reduction reaction, the impurity type and relative amount exhibit a strong influence on the electrode-reaction kinetics.

3.2 Results & Discussion

3.2.1 Effect of CH_4/H_2 Ratio on the Physical Properties

Diamond films were deposited on p-Si(100) substrates using CH_4/H_2 source gas ratios of 0.3, 0.5, 1, 2, 3 and 5% (% = (sccm CH_4/sccm H_2) x 100). Figure 3.1 shows representative atomic force microscopic (AFM) images (*ex situ*) of films deposited from different CH_4/H_2 source gas ratios. Clearly, the grain size decreases with increasing CH_4/H_2 ratio resulting in macroscopically smoother films. The extent of secondary nucleation increases with increasing CH_4/H_2 ratio, and this leads to a decrease in the nominal grain size (*i.e.*, smoother films) and an increase in the fraction of grain boundary. It is at these grain boundaries that much of the nondiamond sp^2 carbon impurity exists. Raman imaging has revealed that the nondiamond carbon impurity in polycrystalline films often exists locally at the grain boundaries.[17] These trends are reflected in the data presented in Table 3.1. At the high CH_4/H_2 ratios, the rate of renucleation exceeds the rate of crystal growth, and this leads to the smooth texture.

Table 3.1. Nominal Diamond Crystallite Diameter and Height for Films Deposited from Different Methane-to-Hydrogen Source Gas Ratios

CH_4/H_2 Ratio (%)	Nominal Crystallite Diameter (μm)	Maximum Grain Height (μm)
0.3	2.7 ± 0.6	1.0 ± 0.2
0.5	2.0 ± 0.2	1.3 ± 0.2
1	1.8 ± 0.3	1.0 ± 0.3
2	1.5 ± 0.1	0.72 ± 0.08
3	1.4 ± 0.1	1.0 ± 0.1
5	0.5 ± 0.1	0.47 ± 0.08

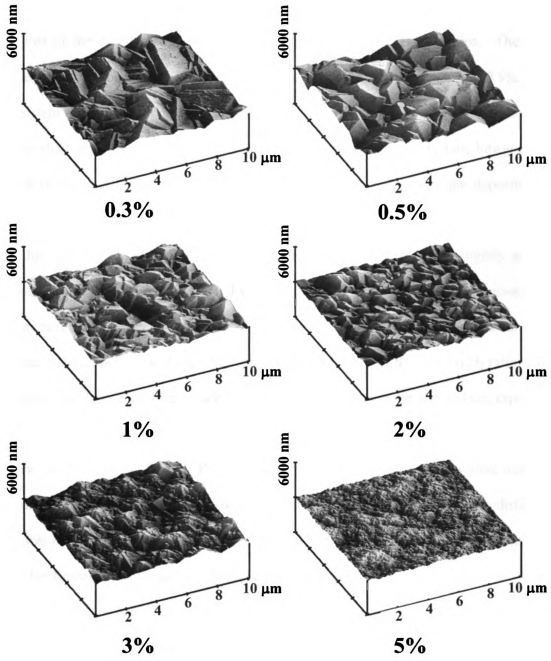

Figure 3.1. Atomic force micrographs of diamond films deposited from different CH_4/H_2 source gas mixtures.

Scanning electron microscopy (SEM) was also used to assess the physical features of the diamond films deposited using the different CH_4/H_2 ratios. These are presented in Figure 3.2. There is little difference between the 0.3 and 0.5% films consistent with the AFM images. Both possess large crystals with extremely smooth facets and little defect density. The 1% film also possesses large crystals; however, the facets of the crystals are notably rougher. This ratio may be where the deposition of nondiamond sp^2-bonded carbon begins. This is in agreement with the Raman spectrum for this film presented in Figure 3.3. The 2% CH_4/H_2 ratio film has slightly smaller crystals than the 1% film. Additionally, the facets are increasingly rougher, possessing a large number of defects. Interestingly, the Raman spectrum indicates minimal nondiamond carbon impurity residing within this film. Increasing the CH_4/H_2 ratio to 3% results in the deposition of nondiamond sp^2-bonded carbon all over the surface, especially within the grain boundaries. As with the AFM images, diamond crystals are still visible on the surface. When the CH_4/H_2 ratio is increased to 5%, there are no visible diamond crystals in the film. Instead, the surface is macroscopically smooth with dendritic-like features and likely possesses mostly nondiamond sp^2-bonded carbon. This is consistent with the Raman spectrum for this film presented in Figure 3.3.

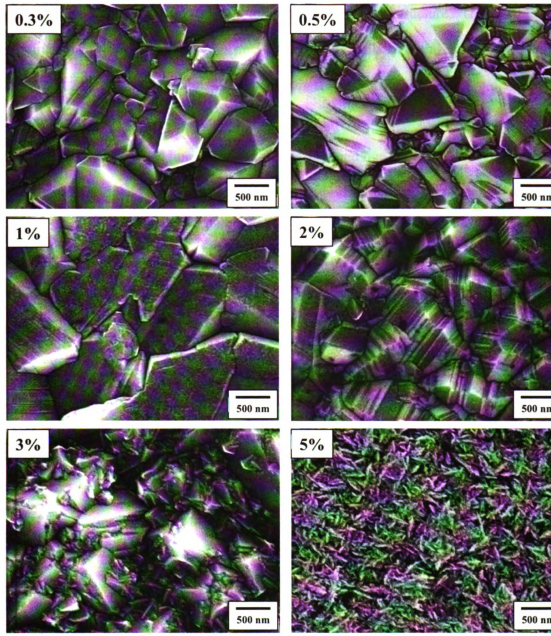

Figure 3.2. Scanning electron micrographs (secondary electron) of diamond films deposited from different CH_4/H_2 source gas mixtures.

Raman spectroscopy was used to probe the film microstructure. This technique is routinely used to characterize the microstructure of both sp^2- and sp^3-bonded carbon materials.[18-22] Spectra for films deposited from different CH_4/H_2 ratios are displayed in Figure 3.3. The first-order phonon modes for Si at 514 cm^{-1} and diamond at 1332 cm^{-1} are denoted by the dotted lines. The first-order diamond line intensity, width and position are sensitive to such factors as the crystallite size, optical density, boron doping level, net stress, defect density and film quality.[18,19,23] One evident trend in Figure 3.3 is the decrease in peak amplitude and increase in peak width of the diamond phonon line with increasing CH_4/H_2 ratio. These phenomena are better illustrated by the inset in Figure 3.3 which shows an enlargement of the spectral region surrounding the diamond phonon peak. Table 3.2 summarizes the line position and linewidth data for films deposited from the different source gas ratios.

Table 3.2. Raman Spectroscopic Data for Films Deposited from Different Methane-to-Hydrogen Source Gas Ratios

CH_4/H_2 Ratio (%)	**Average Diamond Peak Position (cm^{-1})**	**Average Diamond Linewidth (FWHM, cm^{-1})**
0.3	1333.7 ± 0.2	12.7 ± 0.3
0.5	1332.4 ± 0.5	15 ± 2
1	1332.6 ± 0.3	16 ± 2
2	1333.0 ± 0.8	17 ± 2
3	1332.8 ± 0.1	40 ± 20
5	NA	NA

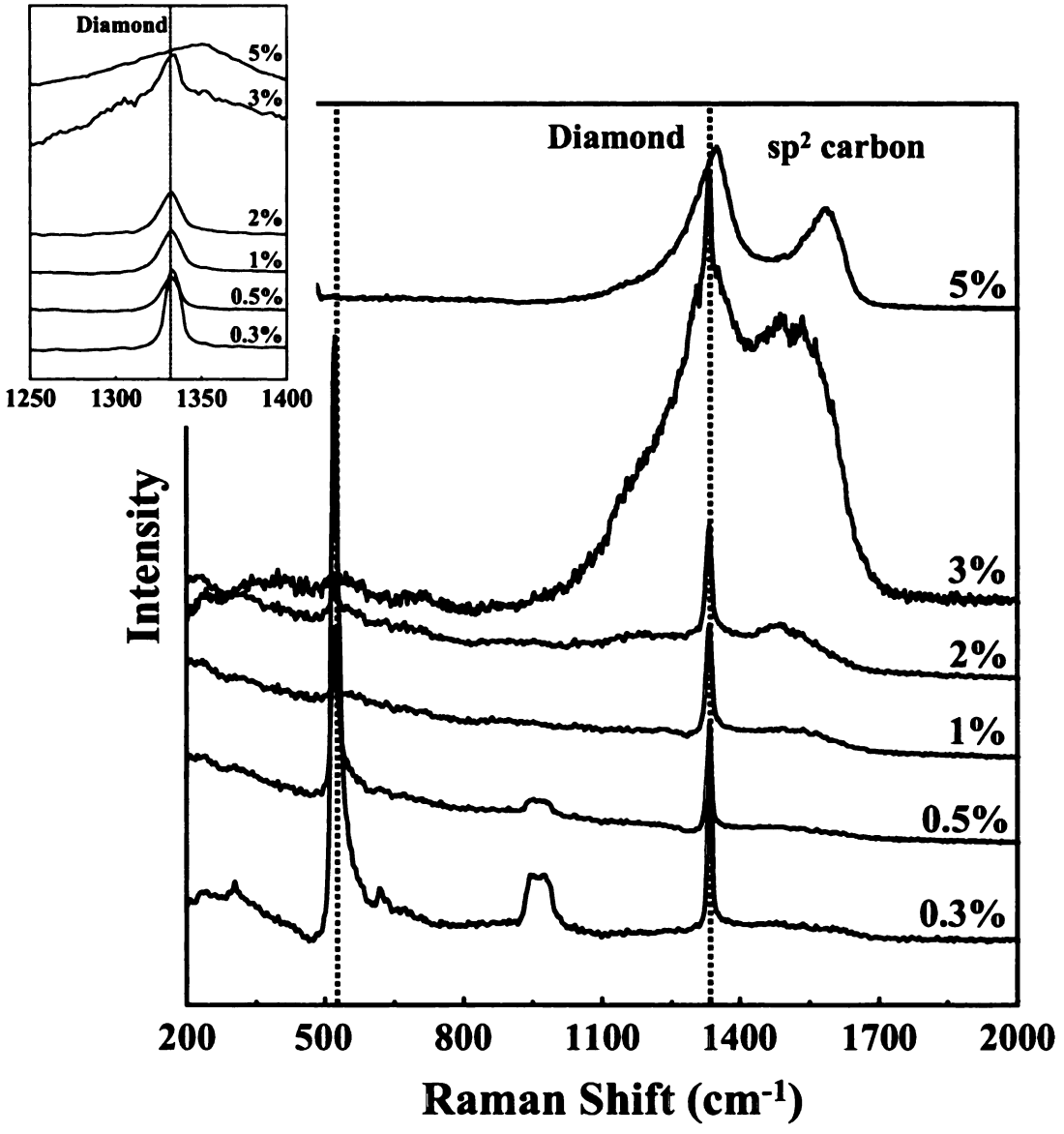

Figure 3.3. Raman spectra of diamond films deposited from different CH_4/H_2 source gas mixtures. Inset is enlarged region around diamond peak.

The diamond linewidth is a qualitative indicator of the crystalline film quality.[3,17] For comparison, the linewidth (FWHM) for a high pressure high temperature piece of diamond used to calibrate the instrument was *ca.* 5-7 cm^{-1} (a perfect single crystal sample should be *ca.* 2-3 cm^{-1}). To a first approximation, the linewidth is inversely related to the

phonon lifetime and is a measure of the defect density. The Si line intensity decreased as the CH_4/H_2 ratio was increased, due to increasing diamond film thickness as the growth rate scales with carbon concentration in the gas phase. The diamond line intensity decreased because the films became more opaque due to the increasing levels of sp^2-bonded nondiamond carbon impurity. The elevated level of sp^2-bonded carbon is evidenced by the scattering intensity between 1500 and 1590 cm^{-1}, which increased with increasing CH_4/H_2 ratio.[3,9,17-19,24-29] The nondiamond carbon impurity most likely consists of a mixture of sp^2- and sp^3-bonded carbon. Scattering intensity for the nondiamond carbon is most pronounced for the 3 and 5% CH_4/H_2 films but is also observed for the 2% film and even minimally for the 1% film. This is in agreement with the SEM data above. Interestingly, the 2 and 3% films exhibit a peak maximum at *ca.* 1500 cm^{-1} (1487 and 1495 cm^{-1}, respectively). Scattering at this wavenumber is characteristic of amorphous carbon (*i.e.*, a mixture of sp^3- and sp^2-hybridized bonding).[17,18,24,27,28]

As previously mentioned, the first-order diamond phonon line was not detected for the 5% CH_4/H_2 film. Rather, two peaks were observed at 1350 and 1589 cm^{-1}; peaks that are characteristic of glassy carbon.[18,22,25,28,30] The peak at 1350 cm^{-1} is due to disorder in the material (*i.e.*, "D" band), while the peak at 1589 cm^{-1} is attributed to the graphitic sp^2 nondiamond carbon (*i.e.*, "G" band) in the material.[18,19,21] Though this spectrum closely resembles that for glassy carbon, Marcus *et al.* noted that the presence of these spectral features does not necessarily indicate the complete absence of diamond.[28] For example, the authors observed a Raman spectrum for a sample in which

the first-order diamond line was absent even though X-ray diffraction (XRD) showed reflections characteristic of cubic diamond. The Raman scattering by nondiamond carbon can mask the scattering intensity from diamond because the cross-sectional scattering coefficient for the former (graphite as a model microstructure) is ~50 times larger than that for diamond.[19,29] Therefore, a small amount of nondiamond carbon near the surface can mask the spectral response for diamond. Interestingly, the D/G ratio, discussed in Chapter 1 for GC (θ_{edge} = 0.1-0.18), for the 5% CH_4/H_2 ratio film was *ca.* 1.3 indicating the nondiamond carbon is highly disordered with significant fraction of edge plane exposed.

The carbon microstructure was also evaluated using powder X-ray diffraction analysis (XRD). The XRD spectra were obtained using a Cu primary target (1.5407 Å) and scanning 2-theta from 20 to 100°. XRD spectra of the diamond films deposited from the different CH_4/H_2 ratios, shown in Figure 3.4, can be compared to those of HOPG and GC, model sp^2-bonded carbon materials, shown in Figure 3.5. Table 3.3 compares measured peaks with standards from the American Society for Testing and Materials (ASTM) to identify resulting peaks. Reflections for the diamond crystallite orientations of (111), (220), and (311) are observed for each film and are marked along with the Si(400) substrate peak, the graphite (002) (G(002)) peak, and a peak due to non-orientated carbon (C), by the dotted lines, respectively. Note that the Si(400) peak is not observed for the 0.5% CH_4/H_2 film because there is a signal at a 2θ value of 28.54 corresponding to Si(111) (*i.e.*, Si substrate has different orientation). The broadness observed for the Si peak is likely due to Si-C formation at the beginning of the growth.

Perhaps the thickness of this layer influences the relative intensity and width of this peak as both generally increase with increasing CH_4/H_2. One would assume that the Si signal should decrease with increasing film thickness. Therefore it is unlikely that the film thickness increases appreciably with increasing CH_4/H_2 ratio.

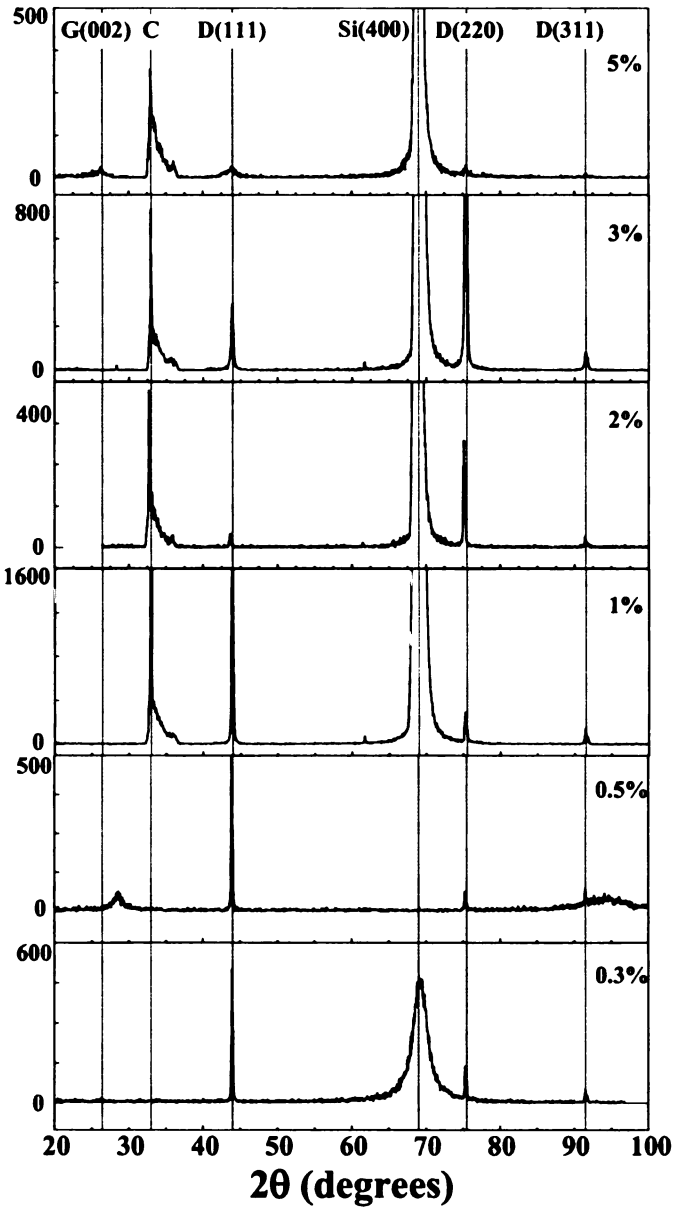

Figure 3.4. Powder X-ray diffraction spectra of diamond films deposited from different CH_4/H_2 source gas mixtures.

Table 3.3. Comparison Between Measured Powder X-ray Diffraction Data and Standard Values from ASTM 6-0675, 23-0064, and 46-0943

Measured Values				ASTM	
2θ (degree)	**Carbon Phase**	**Orientation**	**d-spacing (Å)**	**d-spacing (Å)**	**Relative Intensity**
26.50	Graphite	(002)	3.36	3.36	100
33.96	Carbon	None	2.72	2.70	50
43.92	Diamond	(111)	2.06	2.06	100
75.30	Diamond	(220)	1.26	1.26	25
91.50	Diamond	(311)	1.08	1.08	16

The intensity of the peak associated with the diamond (111) phase decreases and the relative intensity of the peak for the (220) phase increases with increasing CH_4/H_2 ratio suggesting that the incorporation of the nondiamond impurity also changes the crystalline orientation of the diamond. Table 3.4 shows the change in the full width at half maximum (FWHM) as well as the intensity ratio between the two peaks associated with the diamond (111) and (220) phases. The general increase in FWHM is consistent with a decrease in diamond quality. Interestingly, films that exhibited considerable nondiamond carbon impurity in the Raman spectra have a (111)/(220) intensity ratio value of 8-9, suggesting a change in the nature of the diamond growth with increasing CH_4/H_2 ratio. This value however decreased for the 5% film, presumably due to the large graphite presence observed in both the Raman and XRD spectra.

Table 3.4. Full Width at Half Maximum (FWHM) and Peak Intensity Ratio for the Diamond (111) and (220) Peaks

CH_4/H_2 Ratio	FWHM (degrees)		$I_{(220)}/I_{(111)}$ Ratio
	D(111)	D(220)	
0.3	0.181	0.182	0.241
0.5	0.190	0.203	0.119
1	0.226	0.254	0.134
2	0.196	0.192	8.13
3	0.307	0.249	8.92
5	0.546	0.156	1.26

The powder XRD spectra for the different diamond films can be compared to the spectra of two model sp^2-bonded carbon materials, HOPG and GC, which are shown in Figure 3.5. The dotted lines are the same as those in Figure 3.4 and are inserted as reference points. Only the 5% CH_4/H_2 film possesses an appreciable amount of graphite of the (002) orientation. Interestingly, despite not exhibiting a Raman signal corresponding to diamond, the XRD spectrum does show some diamond signal for both the (111) and (220) orientation. This is in agreement with the work of Marcus *et al.* and discussed above.[28]

The signal at a 2θ value of 33° becomes more prominent with increasing CH_4/H_2 ratio, suggesting that it is due to a nondiamond form of carbon. The corresponding d-spacing value correlates well with that of non-orientated (possibly amorphous) carbon (ASTM 46-0943). However, interestingly this signal was not observed for HOPG, GC, or tetrahedral amorphous carbon (TAC, spectrum not shown because the only peak

observed was due to the Si substrate). Perhaps the signal is due to a mixed sp^3/sp^2 carbon incorporation resulting in a signal located between that for graphite and diamond, respectively.

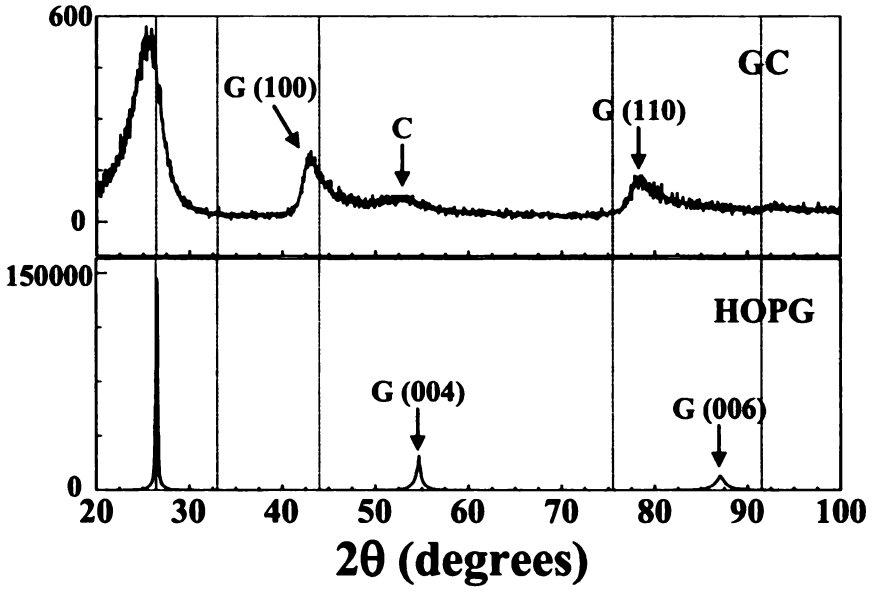

Figure 3.5. Powder X-ray diffraction spectra for highly orientated pyrolytic graphite (HOPG) and glassy carbon (GC). The dotted lines are the same as those in Figure 3.4, and inserted as reference points.

3.2.2 Effect of CH_4/H_2 Ratio on the Electrochemical Properties

The diamond electrodes were mounted in a single compartment glass cell, as described in Chapter 2 and exposed to potential cycling in N_2-saturated 0.1 M $HClO_4$ solution at a scan rate of 100 mV/s. Background CV current-potential (*i-E*) curves for films deposited from different CH_4/H_2 ratios are shown in Figure 3.6. The potential window clearly decreases and the background current magnitude increases with increasing CH_4/H_2 ratio. The potential window, defined as the difference between the anodic and cathodic potentials at which the current reaches ±50 μA (or ±250 $\mu A/cm^2$), is

presented in Table 3.5. The values range from 3.3 V for the 0.3% CH_4/H_2 film to 2.3 V for the glassy carbon-like 5% CH_4/H_2 film.

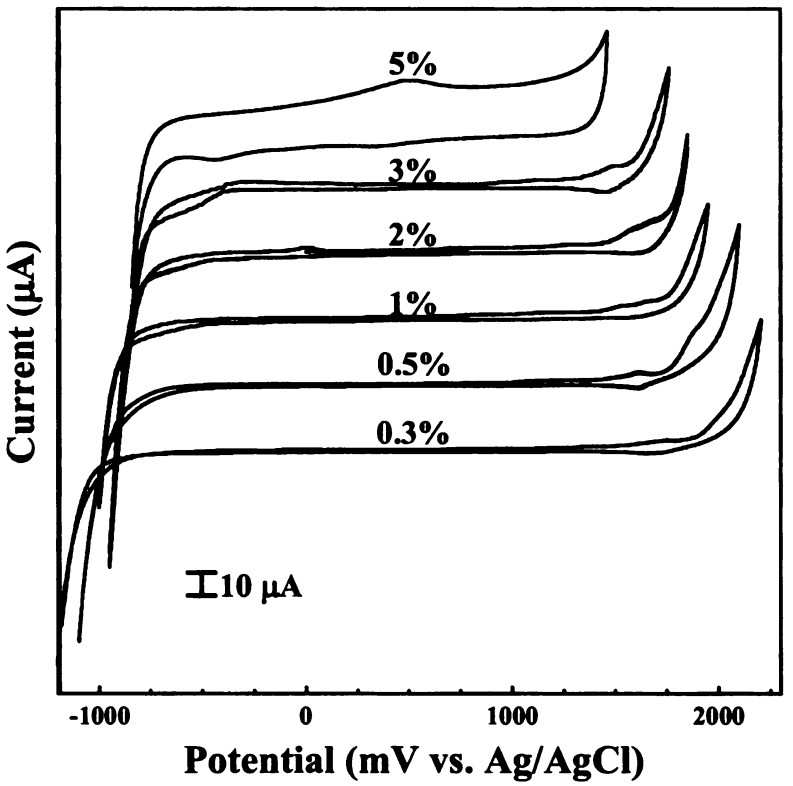

Figure 3.6. Background cyclic voltammetric *i-E* curves in degassed 0.1 M $HClO_4$ for diamond films deposited from different CH_4/H_2 source gas mixtures. Scan rate = 100 mV/s.

Table 3.5. CV Working Potential Window (i = ±50 μA) for Films Deposited from Different Methane-to-Hydrogen Source Gas Ratios

Methane-to-Hydrogen Ratio (%)	Potential Window (V)
0.3	3.3
0.5	3.0
1	2.9
2	2.7
3	2.6
5	2.3[a]

[a] Anodic limit was only +200 μA/cm^2

The voltammograms for the 0.3-3% films are largely featureless between -500 and 1000 mV, a potential region where surface redox processes associated with electroactive carbon-oxygen functionalities occur.[1,3,4,31-35] Although the Raman spectrum for the 3% CH_4/H_2 film indicates a large presence of sp^2-bonded nondiamond carbon impurity, the background voltammogram shows no evidence for any redox-active carbon-oxygen functional groups that tend to populate the edge-plane sites of sp^2-bonded carbon. This suggests that the nondiamond carbon contains a mixed sp^2/sp^3 microstructure with a limited number of sites where redox-active carbon-oxygen functionalities can exist.

One or more oxidation peaks can be seen prior to the onset current for oxygen evolution, and these have been linked to the oxidation of sp^2-bonded carbon impurity at the diamond surface.[11] Again, this impurity is likely localized at the surface and consists of a mixture of sp^2- and sp^3-carbon bonding. There is a general trend of increasing peak charge (anodic) with increasing CH_4/H_2 ratio, consistent with the increased presence of oxidizable nondiamond carbon impurity.

A significant change is seen for the 5% film, which exhibits a reduced potential window and an enlarged background current. A reversible redox couple is observed near 400 mV (more visible in Figure 3.7), which is consistent with the presence of redox-active carbon-oxygen functionalities at the nondiamond carbon impurity sites (*e.g.*, quinone/hydroquinone type of couple).[33-36] Based on the Raman spectral data, the nondiamond carbon impurity in this film is largely sp^2-bonded, much like the turbostratic microstructure of glassy carbon. In fact, this CV greatly resembles one for freshly

polished glassy carbon. It would appear that the edge-plane carbon impurity sites are highly susceptible to oxidation during exposure to the laboratory O_2/H_2O environment and to these electrochemical polarization conditions.

Figure 3.7 compares the background voltammetric *i-E* curve for a 5% film as-deposited with that for the same film following an acid-washing/rehydrogenation procedure. This treatment involved cleaning the diamond surface in warm aqua-regia (3:1 $HCl:HNO_3$) and then in warm 30% H_2O_2 for 30 min each. The film was then exposed to a H_2 plasma for 30 min at a pressure of 35 torr and a power of 1 kW. This procedure serves to clean the diamond of both inorganic and organic impurities and to chemically etch away the surface sp^2-bonded nondiamond carbon impurity.

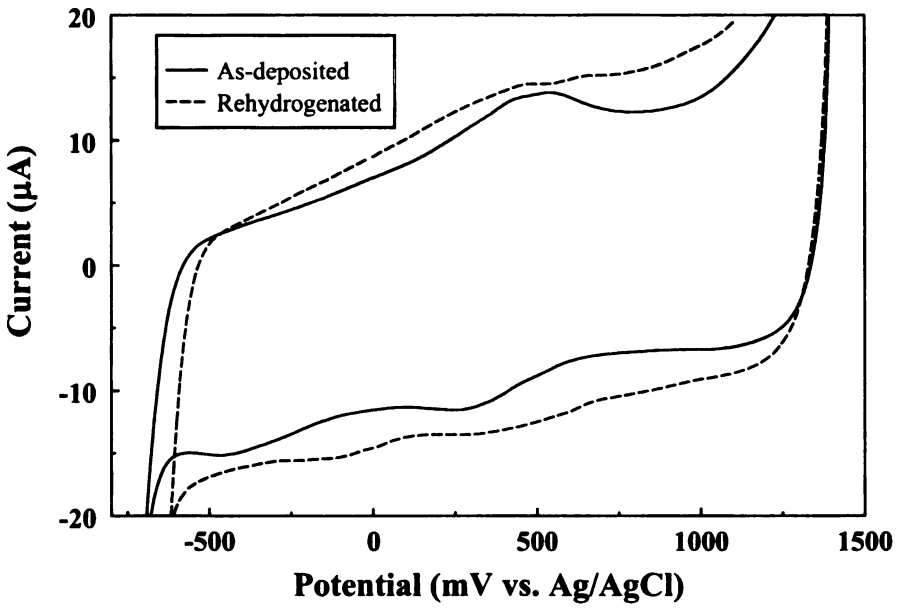

Figure 3.7. Background cyclic voltammetric *i-E* curves in degassed 0.1 M $HClO_4$ for 5% CH_4/H_2 diamond film as-deposited and following an acid-washing/rehydrogenation procedure. Scan rate = 100 mV/s.

There are two things worth noting here. One is the slight increase in background current upon rehydrogenation. This is possibly due to the removal of the sp^2-bonded carbon, mainly within the grain boundaries, resulting in a slightly rougher surface and larger exposed surface area. This large background current also suggests that the large nonfaradaic current observed in the background is not due solely to surface functionalities produced by the nondiamond carbon. It is likely that the large double-layer capacitance observed (C_{dl}) is due to the π-bonding possessed by the sp^2-bonded nondiamond carbon incorporated within the film microstructure. It is also worth mentioning that it is also possible that the lattice hydrogen introduced via the H_2 plasma increases the surface conductivity resulting in an increase in electrode capacitance. The second observation to note is the decrease in the signal of the redox couple near 400 mV. This is consistent with the signal observed in the original *i-E* curve being due to carbon-oxygen functionalities on the surface, which would be expected to decrease in concentration after rehydrogenation.

SEM images were taken of the 5% CH_4/H_2 ratio film following the acid-washing/rehydrogenation procedure and compared to the as-deposited film. These are shown in Figure 3.8A and B. The large images were obtained at a magnification of 30K, while the insets for both were obtained at a magnification of 70K. The as-deposited film (A) is the same as that shown in Figure 3.2, just enlarged for comparison. There is no significant difference observed between the two images. Therefore, it appears that an increased surface area is not the reason for the increased background current.

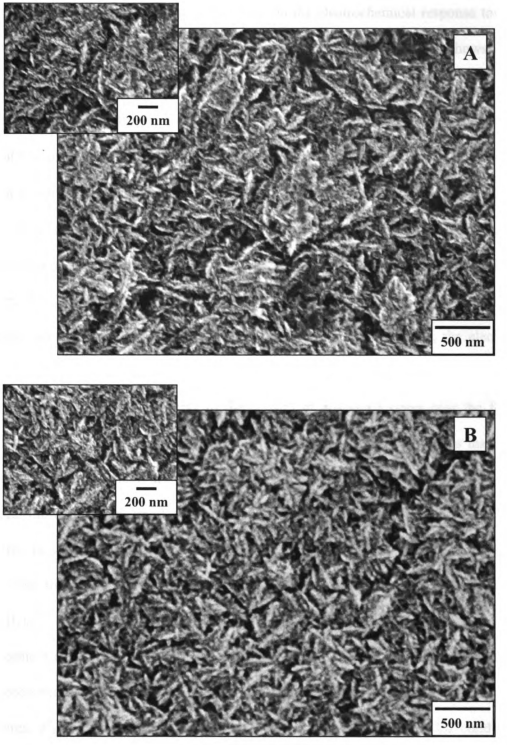

Figure 3.8. SEM images (secondary electron) of the 5% CH_4/H_2 ratio diamond film (A) as-deposited and (B) following acid-washing and rehydrogenation. Insets are high resolution images of the center region of each figure.

The effect of the nondiamond impurity on the electrochemical response towards several well known redox analytes was also investigated. Figure 3.9A-D shows cyclic voltammetric *i-E* curves (scan rate = 100 mV/s) for several redox test analytes at films deposited from different CH_4/H_2 ratios. A summary of the peak potential separations, ΔE_p, at a scan rate of 100 mV/s (n = 4 electrodes) is presented in Table 3.6. The values are not *i*R corrected. There is a rationale for studying these particular redox systems, one that originates largely from the work of McCreery and coworkers with glassy carbon.[37-40] Redox reactions generally fall under two classifications. One type includes reactions that proceed by simple diffusion of the analyte to the electrode-solution interface, with the electrode serving solely as a source or sink for electrons. In this case, the electrode-reaction kinetics is relatively insensitive to factors such as the surface chemistry and microstructure but is very sensitive to the density of electronic states near the formal potential (so-called outer-sphere reaction). The other type includes reactions that occur via some specific interaction with the electrode surface; for example, reactions that proceed through an adsorbed state. In this case, the electrode-reaction kinetics is sensitive to surface chemistry and microstructure as well as the density of electronic states near the formal potential (so-called inner-sphere reaction). The redox systems, $Ru(NH_3)_6^{3+/2+}$, methyl viologen, $IrCl_6^{2-/3-}$, $Ru(bpy)_3^{3+/2+}$ and chlorpromazine, all undergo outer-sphere electron transfer and the electrode kinetics are relatively insensitive to the physicochemical properties of diamond. Apparent heterogeneous electron-transfer rate constants, k^0_{app}, between 0.01 and 0.2 cm/s, are commonly observed for conducting polycrystalline films (both microcrystalline or nanocrystalline) without extensive pretreatment.[3,4,6,7,9,41] Normally, carbon and metal electrodes must be pretreated (*e.g.*,

polishing) to achieve such a large rate constant. $Fe(CN)_6^{3-/4-}$ proceeds through a more inner-sphere electron-transfer pathway, and the electrode-reaction kinetics are highly sensitive to the surface termination of diamond.[41,42] Presumably, the reaction proceeds through a specific surface site that is blocked by surface oxygen, although this needs further study. k^0_{app} values ranging from 0.01 to 0.1 cm/s are commonly observed for clean, hydrogen-terminated films, but the rate constants decrease by over two orders of magnitude for oxygen-terminated films.[4,5,41,43] For sp^2-carbon electrodes, the electrode kinetics are strongly influenced by the fraction of exposed, clean edge plane.[37-40] It should be emphasized that $Fe(CN)_6^{3-/4-}$ is not a simple, outer-sphere redox system on carbon (both diamond and glassy carbon) as researchers often supposes. Rather, it is a surface sensitive redox system that is quite useful for probing the electronic properties, surface cleanliness and surface chemistry of electrodes, particularly of diamond.

Table 3.6. Summary of the Cyclic Voltammetric Peak Potential Separations (ΔE_p) for Different Redox Analytes at Films Deposited from Different Methane-to-Hydrogen Source Gas Ratios

CH_4/H_2 Ratio (%)	Peak Potential Separation, ΔE_p (mV)			
	$Fe(CN)_6^{3-/4-}$	$Ru(NH_3)_6^{3+/2+}$	$Fe^{3+/2+}$	4-*t*BC
0.3	80 ± 6	90 ± 10	890 ± 60	750 ± 150
0.5	69 ± 8	76 ± 8	780 ± 50	500 ± 100
1	70 ± 1	73 ± 1	730 ± 60	530 ± 100
2	71 ± 7	73 ± 3	760 ± 50	520 ± 30
3	66 ± 2	68 ± 2	690 ± 50	470 ± 50
5	60 ± 1	62 ± 3	120 ± 20	68 ± 9

Scan rate = 100 mV/s

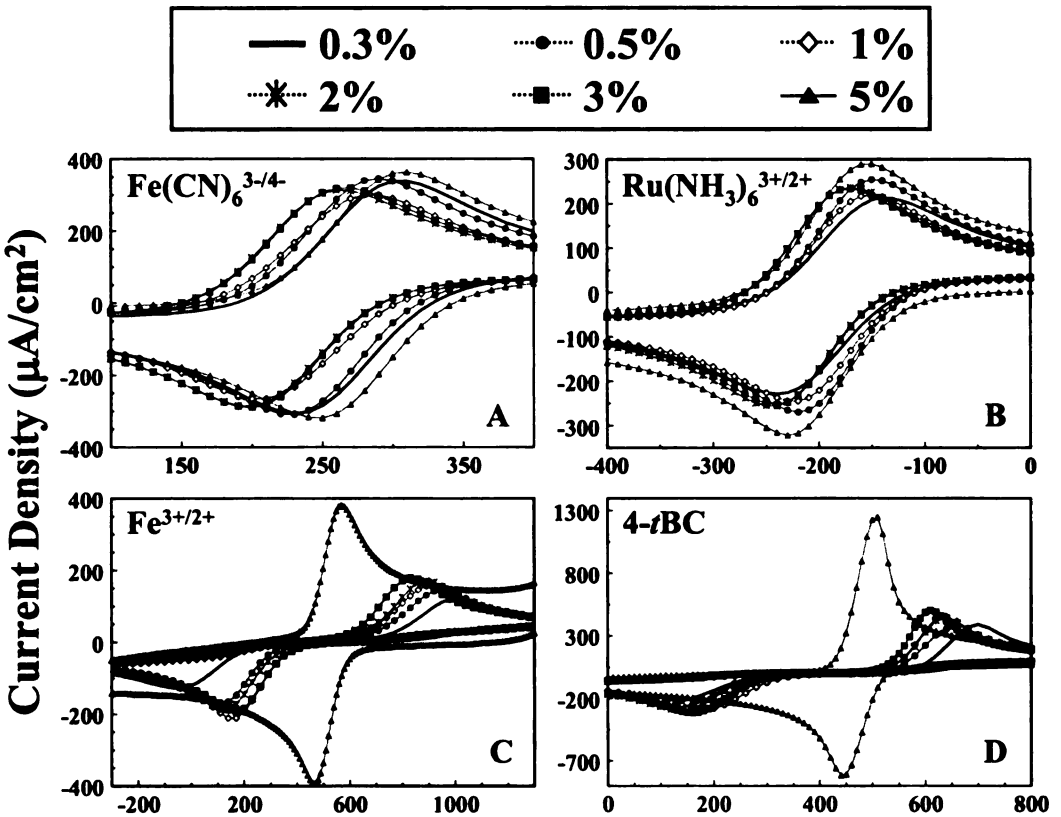

Figure 3.9. Cyclic voltammetric *i-E* curves at diamond films deposited from different CH_4/H_2 source gas mixtures for 1 mM concentrations of (A) $Fe(CN)_6^{3-/4-}$, (B) $Ru(NH_3)_6^{3+/2+}$, (C) $Fe^{3+/2+}$ and (D) 4-*t*BC dissolved in either 1 M KCl (A and B) or 0.1 M $HClO_4$ (C and D). Scan rate = 100 mV/s.

Well-defined symmetric curves are observed for both $Fe(CN)_6^{3-/4-}$ and $Ru(NH_3)_6^{3+/2+}$ (Figure 3.9A and B), with ΔE_p values ranging from 60 to 90 mV, depending on the CH_4/H_2 ratio. It is clear from the voltammetric *i-E* curves that ΔE_p for either redox system is not significantly affected by the presence of sp^2-bonded nondiamond carbon impurity, regardless of the level or type. There is a general trend of decreasing ΔE_p with increasing CH_4/H_2 ratio; however, only over a relatively small range of *ca.* 20-30 mV. The low ΔE_p (theoretical value of 59/n mV) for some films reflects

relatively rapid electrode-reaction kinetics. The fact that the kinetics are rapid, even though the electrodes were exposed to the laboratory atmosphere for an extended period of time and no conventional pretreatment was applied prior to use, reflects the material's activity and resistance to fouling. The electrodes were only soaked in clean IPA for 10 min to clean the surface prior to use. There is some random variation in $E_{p/2}$ for $Fe(CN)_6^{3-/4-}$ but nothing that follows a predictable trend. The peak currents, i_p^{ox} and i_p^{red}, are nearly equal for all the electrodes, with an i_p^{ox}/i_p^{red} ratio near unity for both analytes. The peak currents for the 5% CH_4/H_2 film do appear slightly larger than the others, but this is due to the larger background current, as the curves shown were not background corrected. When background corrected, the i_p^{ox} and i_p^{red} values are all nominally the same.

The ΔE_p for $Fe^{3+/2+}$, shown in Figure 3.9C, decreases from 890 to 690 mV as the CH_4/H_2 ratio increases from 0.3 to 3%. There is, however, a more marked decrease for the 5% film, as ΔE_p drops to 120 mV. Clearly, this redox reaction undergoes electron transfer that is site dependent and faster at a more sp^2-bonded microstructure; presumably sites with more surface oxygen. The question is, how does this microstructure influence the reaction rate? $Fe^{3+/2+}$ is of the inner-sphere type, with k^0_{app} being very sensitive to the presence of surface carbon-oxygen functionalities, specifically carbonyl types, for both glassy carbon and diamond.[41,42,44] Carbonyl functional groups have been shown to catalyze this redox reaction, thereby improving the electrode kinetics.[44] We suppose the nondiamond carbon impurity, particularly that with more sp^2 bonding character, contains dangling bonds at the surface that react with O_2 and/or H_2O in the air or solution. Based

on the great reduction in ΔE_p for the 5% CH_4/H_2 film, it appears that the mixed sp^2/sp^3 carbon microstructure up to the 3% level has a limited number of oxidizable sites so that the oxygen incorporation is relatively low. However, the glassy carbon-like microstructure of the nondiamond carbon in the 5% film has a much higher number of oxidizable sites. This surface is the most extensively oxidized and probably contains carbonyl functionalities. Therefore, we suppose that the nondiamond carbon impurity influences this particular redox system by providing sp^2 sites where carbon-oxygen functional groups can readily form, specifically catalyzing carbonyls.[44] The catalysis may involve lowering of the reorganization energy of the H_2O solvation sphere surrounding the $Fe^{3+/2+}$ couple. Interestingly, acid-washing and rehydrogenating one of the 5% films did not significantly alter the electrode response towards this analyte. The ΔE_p was 136 mV at a scan rate of 100 mV/s. While this could be due to incomplete removal of the oxygen functional groups or quick oxidation of the oxygen-free surface upon air exposure, it is possible that the remaining π-π interactions are enough to catalyze the reaction through promoting molecular adsorption. All these would be consistent with the narrow potential window observed in the background voltammetric *i-E* curve for this film.

Figure 3.9D shows cyclic voltammetric *i-E* curves for 4-*t*BC at the various films. Clearly, nondiamond carbon impurity significantly influences the electrode response for this analyte as there is a progressive decrease in ΔE_p from 750 to 70 mV with increasing CH_4/H_2 ratio. The more complicated organic redox analytes, dopamine, 4-methylcatechol, and 4-*t*BC, are inner-sphere systems with k^0_{app} values of 10^{-4} to 10^{-6}

cm/s, common for hydrogen-terminated diamond.[3,4,6,7,9] It is postulated that the slow kinetics for these polar aromatic analytes result because of weak adsorption on the diamond surface. It is possible that π-π interactions, through the extended electronic conjugation, are perhaps more influential than surface oxides in promoting molecular adsorption for these analytes. This conclusion comes, in part, from our past work with low-oxygen, hydrogenated glassy carbon.[45,46] We suppose that the sp^2-bonded carbon impurity provides adsorption sites for 4-*t*BC, with the adsorption lowering the activation barrier for charge transfer. The nondiamond carbon impurity content grows with increasing CH_4/H_2, as determined by Raman spectroscopy and this leads to an increased number of adsorption sites. The greater peak current seen for the 5% CH_4/H_2 film, as compared to the others, is consistent with increased adsorption. Interestingly, the ΔE_p observed for a rehydrogenated 5% film only increased slightly compared to an as-deposited film. The ΔE_p was found to be 94 mV at a scan rate of 100 mV/s for the rehydrogenated film compared to *ca.* 70 mV for the as-deposited film. This again could be attributed to incomplete removal of the oxygen functional groups, quick oxidation of the oxygen-free surface or, if the oxide content is minimal, significant influence from the π-π interactions in the film which promote molecular adsorption of the analyte.

3.2.3 Effect of CH_4/H_2 Ratio on the Oxygen Reduction Reaction (ORR)

The ORR in 0.1 M $HClO_4$ (Figure 3.10 and Table 3.7) and 0.1 M NaOH (Figure 3.11 and Table 3.8) for select CH_4/H_2 ratios was also used to probe the electrochemical effects of the incorporated nondiamond carbon impurity. The carbon surface chemistry and microstructure are known to play key roles in the electrode kinetics for this surface-

sensitive redox reaction.[47-51] At carbon electrodes, the reduction reaction product ($2e^-/2H^+$) is usually H_2O_2 or HO_2^-, depending on the pH, and the kinetics are generally much slower than at metals.[44,50,51] These products are formed via reactions 3.2.1 and 3.2.2 below, respectively.[50]

$$O_2 + 2H^+ + 2e^- \rightleftarrows H_2O_2 \qquad (3.2.1)$$

$$E^o \text{ (pH 0)} = 498 \text{ mV } \textit{vs.} \text{ Ag/AgCl (3 M NaCl)}^{50}$$

$$O_2 + H_2O + 2e^- \rightleftarrows HO_2^- + OH^- \qquad (3.2.2)$$

$$E^o \text{ (pH 13)} = -262 \text{ mV } \textit{vs.} \text{ Ag/AgCl (3 M NaCl)}^{50}$$

Diamond is known to possess a large kinetic overpotential for this reaction.[52,53] One possible cause for this is weak adsorption of the reactant, O_2, or the primary reaction intermediate, $O_2^{\bullet -}$ (super oxide), on the hydrogen-terminated surface. Yang and McCreery found that when there are available adsorption sites (*i.e.*, clean GC), the electrogenerated $O_2^{\bullet -}$ adsorbs to the electrode surface. However, when these adsorption sites are blocked or unavailable, the $O_2^{\bullet -}$ species cannot adsorb and remains in aqueous solution.[47] The mechanistic aspects of this reaction on diamond are not fully understood at present. The linear sweep voltammetric (LSV) *i-E* curves shown in Figure 3.10 reveal a positive shift in the onset potential for the reduction current with increasing CH_4/H_2. The maximum current increases with CH_4/H_2 from 0.3 to 2% but occurs within the same

potential region from -600 to -800 mV. For example, the maximum current increases from *ca.* -60 $\mu A/cm^2$ for the 0.3% CH_4/H_2 film to *ca.* -137 $\mu A/cm^2$ for the 2% film. The most positive onset potential is seen for the 3 and 5% CH_4/H_2 films. The current for both is approximately the same, -90 $\mu A/cm^2$, and is lower than that for the 2% film. The most positive onset and peak potentials are seen for the 5% film-the "glassy carbon-like" electrode. The positive-shifting onset potential indicates that the nondiamond carbon impurity catalyzes this reaction in some manner. The sp^2 carbon sites involved in this reaction are clearly more active for ORR than sites on the diamond surface. The number of active sites increases proportionally with CH_4/H_2. Interestingly, the change in microstructure for the 2 and 3% CH_4/H_2 films, as seen in the Raman spectroscopic data, does not cause much of a shift in the reduction peak position but does lead to a sizeable decrease in the peak current. The reason for the current decrease is unknown.

One possibility is that the reaction mechanism could be changing, depending on the type and fraction of nondiamond carbon exposed. For example, the reaction might be proceeding via the $4e^-$ pathway to water for the 0.3-2% CH_4/H_2 films, given the large cathodic overpotential. In this case, the current increase observed might simply be due to an increase in the number of available reaction sites. The microstructure changes, particularly for the 3 and 5% CH_4/H_2 films, as seen in the Raman data. Even though the relative fraction of nondiamond carbon increases with CH_4/H_2, this change in microstructure might lead to a reduction in the number of active sites. A change in the reaction mechanism from a $4e^-$ (higher η) to a $2e^-$ (lower η) pathway is also possible. This is pure speculation at this point, because we did not test for the presence of H_2O_2.

One final point that should be made is that for all the films, particularly those with more nondiamond carbon impurity, the kinetically controlled current (*i.e.*, rising portion of the voltammogram) increases gradually rather than sharply over a wide potential range. We suppose that this gradual slope reflects the heterogeneity of the composite electrode architecture, as regions of higher activity at the nondiamond carbon sites are isolated from regions of lesser activity at the diamond sites.

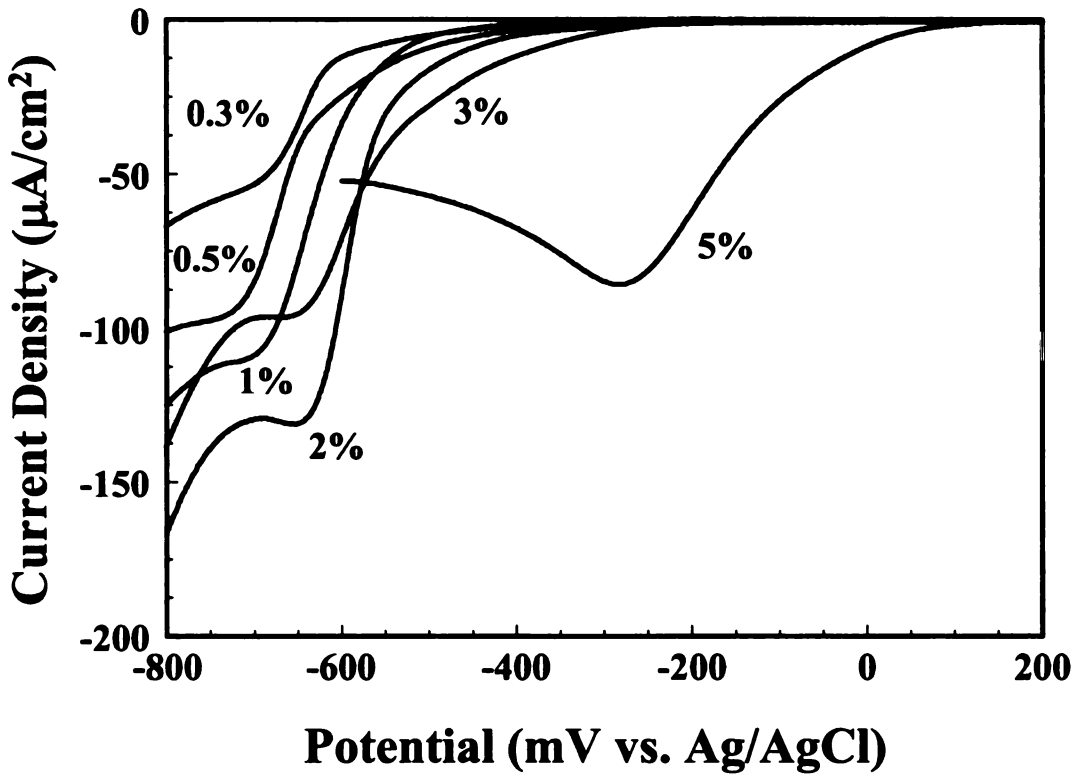

Figure 3.10. Linear sweep voltammetric *i-E* curves for the oxygen reduction reaction (ORR) in 0.1 M $HClO_4$ at diamond films deposited from different CH_4/H_2 source gas mixtures. Scan rate = 1 mV/s.

Table 3.7. Data for ORR in 0.1 M $HClO_4$ for Films Deposited from Different Methane-to-Hydrogen Source Gas Mixtures

CH_4/H_2 Ratio (%)	Reduction Onset Potential (E (V) at -25 μA/cm^2)	Tafel Slope (V/dec)	αn	j_o (A/cm^2)
0.3	-0.63	-0.10	0.60	4.15×10^{-16}
0.5	-0.60	-0.13	0.46	2.43×10^{-13}
1	-0.58	-0.14	0.44	1.31×10^{-12}
2	-0.53	-0.19	0.31	1.80×10^{-10}
3	-0.48	-0.26	0.23	6.76×10^{-9}
5	-0.01	-0.28	0.28	7.23×10^{-8}

Table 3.7 presents a summary of the Tafel analysis data for the ORR in 0.1 M $HClO_4$. Tafel analysis can be performed for irreversible reactions at large overpotentials ($\eta > 118$ mV) (*i.e.*, slow reaction kinetics) and in the absence of mass transfer effects. A plot of η vs. log i is known as a Tafel plot where the slope equals $-2.3RT/n\alpha F$ and the y-intercept equals $(2.3RT/n\alpha F) \log i_o$. The Tafel slope provides information about the mechanism of the reaction as αn can be found, while the y-intercept provides information about the rate of the reaction as the exchange current or "idling" current can be found.

A trend of a more positive onset potential with increasing CH_4/H_2 is evident in the data. The onset potentials for the 0.3-2% CH_4/H_2 films are within a 100 mV range (-0.63 to -0.53 V) of each other. The most positive shifts are seen for the 3 and 5% films. Clearly, the sp^2 microstructure present in the 3 and 5% films is the most active. The Tafel slopes, uncorrected for mass-transport effects, generally increase with increasing

CH_4/H_2. Good linearity was observed over at least one order of magnitude in current, with least-squares correlation coefficients of 0.985, or better. The Tafel slopes for the 0.3, 0.5 and 1% CH_4/H_2 films are approximately the same with values ranging from -0.10 to -0.14 V/dec. These values are close to the -0.12 V/dec value expected for $n = 1$ and a transfer coefficient, α, of 0.5. The slopes for the 2, 3, and 5% CH_4/H_2 films increase with values of -0.19, -0.26, and -0.22 V/dec, respectively. The higher slopes reflect a decrease in the αn product. The calculated αn values are shown in the table. There is a progressive decrease from 0.60 to 0.28 with increasing CH_4/H_2. The transfer coefficient decreases with increasing CH_4/H_2, if $n = 1$ is assumed. Fujishima *et al.* previously reported large Tafel slopes and small α values for the ORR at diamond electrodes.[52,53] The transfer coefficients obtained for the 3 and 5% CH_4/H_2 films are similar to those reported by Yang and McCreery for polished glassy carbon (0.29) at a pH below 9.[47] Because these Tafel slopes were not corrected for mass-transfer effects, we cannot rule out the possibility that the values are influenced from this to some extent. We do not think that the electrode-reaction kinetics are influenced by the electronic properties of the electrode (*i.e.*, potential-dependent density of electronic states), because prior work in our group has revealed that the diamond electrodes, boron-doped at the 10^{20} to 10^{21} cm^{-3} level, behave as a semimetal over a wide potential range.[4,6,7] Outer-sphere redox systems in this same potential region (*e.g.*, $Ru(NH_3)_6^{3+/2+}$ and methyl viologen) have relatively large heterogeneous electron-transfer rate constants, 0.05-0.2 cm/s, and α values near 0.5. We suppose the increasing Tafel slopes (decreasing α values) are caused by heterogeneity in the electrode reactivity (variable reaction sites). The ORR is a surface-sensitive reaction and the kinetic overpotential is dependent on the sites available.

Multiple reaction sites, with different activation energies, are probably present, which vary with CH_4/H_2. The exchange current density, j_o, increases considerably with CH_4/H_2, as the values range from 10^{-16} to 10^{-8} A/cm^2 (geometric area) for the 0.3-5% CH_4/H_2 films.

The ORR reaction kinetics at carbon tend to be faster in alkaline than in acidic media (less η as can be seen by comparing the onset potentials with the standard reduction potentials for Reactions 3.2.1 and 3.2.2). Figure 3.11 shows linear sweep voltammetric *i-E* curves for the ORR in 0.1 M NaOH. The onset potential shifts positive and the maximum cathodic current increases with increasing CH_4/H_2. Again, these shifts occur presumably because of a larger fraction of exposed low-energy reaction sites, which are associated with the sp^2-bonded carbon. The response for the 5% CH_4/H_2 film, in terms of the peak current and potential, is nearly identical to that in 0.1 M $HClO_4$, even though the solution pH is quite different. The absence of a significant pH effect for this reaction at diamond has also been reported by Fujishima *et al.*[52,53] This may mean that the rate-determining step is the 1e$^-$ reduction of O_2 to form superoxide, a pH-independent reaction shown below in equation 3.2.3.

$$O_2 + e^- \rightleftarrows O_{2\,(ads)}^{\bullet -} \qquad (3.2.3)$$

This electrochemical reaction could then be followed by subsequent chemical and electrochemical reaction such as 3.2.4 and 3.2.5 below.[52,53]

$$O_2^{\bullet -}{}_{(ads)} + H_2O \rightleftarrows HO_{2(ads)}^{\bullet} + OH^- \quad (3.2.4)$$

$$HO_{2(ads)}^{\bullet} + e^- \rightleftarrows HO_{2(aq)}^- \quad (3.2.5)$$

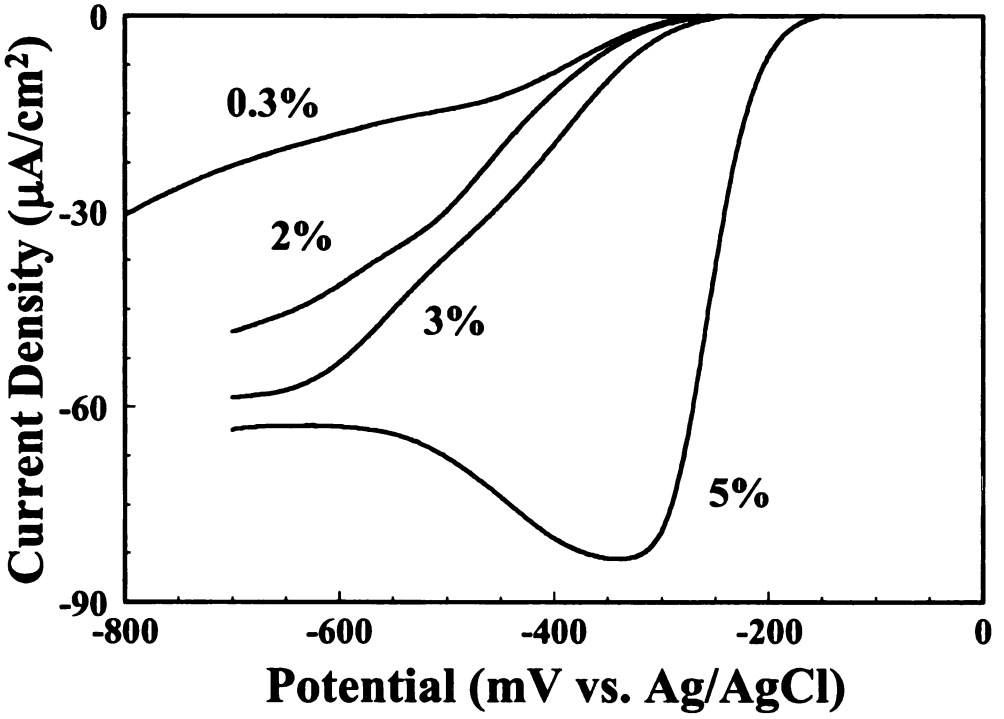

Figure 3.11. Linear sweep voltammetric *i-E* curves for the oxygen reduction reaction (ORR) in 0.1 M NaOH at diamond films deposited from different CH_4/H_2 source gas mixtures. Scan rate = 1 mV/s.

Table 3.8 presents a summary of the Tafel analysis data for ORR in 0.1 M NaOH. The trend of more positive onset potential with increasing CH_4/H_2 is evident. The Tafel slopes range from -0.064 to -0.11 V/dec, but there is no clear trend with CH_4/H_2. These slopes are certainly in the range of those reported for other types of carbon electrodes in alkaline media.[47,49,51] In contrast with the data for $HClO_4$, the lowest slope in NaOH is

seen for the 5% CH_4/H_2 film. The αn values range from 0.55 to 0.70, except for the 5% film for which the value increases to 0.93. This value is similar to that reported for clean glassy carbon in alkaline media.[47] Importantly, the exchange current density, j_o, is several orders of magnitude larger in alkaline than in acidic media. The exchange current density progressively increases from 10^{-7} to 10^{-5} A/cm^2 with an increase in CH_4/H_2 from 0.3 to 5%.

Table 3.8. Data for ORR in 0.1 M NaOH for Films Deposited from Different Methane-to-Hydrogen Source Gas Mixtures

CH_4/H_2 Ratio (%)	Reduction Onset Potential (E (V) at -25 μA/cm^2)	Tafel Slope (V/dec)	αn	j_o (A/cm^2)
0.3	-0.73	-0.086	0.69	4.77×10^{-7}
2	-0.47	-0.11	0.54	8.86×10^{-7}
3	-0.43	-0.086	0.69	1.26×10^{-6}
5	-0.24	-0.064	0.93	8.05×10^{-5}

Rigorous kinetic and mechanistic analysis of the ORR is impossible from the data at hand. Further work is needed to understand this complicated redox reaction on diamond. However, there are several points to be made regarding the role of nondiamond carbon impurity on the reaction.

1. There appears to be a direct correlation between the amount and type of nondiamond carbon impurity present at the surface and the most positive onset potential and largest exchange current density for the reaction. The nondiamond carbon microstructure, specifically, the "glassy carbon-like" structure, is the most active for

ORR. Presumably, the diamond surface exhibits sluggish electrode kinetics for this reaction because of weak adsorption of O_2 or the primary reaction intermediate $O_2^{\bullet -}$

2. There appears to be a minimal pH effect on the ORR at the most active electrode, the 5% film. This may suggest that the rate-determining step for the reaction, in both media, is the $1e^-$ reduction to superoxide, $O_2^{\bullet -}$.

3. Large Tafel slopes are observed for all the diamond electrodes in acidic media, while the slopes in alkaline media are more similar to those reported for other types of carbon. The large Tafel slopes, and correspondingly small values of αn, at least in acid, may reflect a very heterogeneous electrode surface possessing multiple reaction sites with different activities.

3.2.4 Probing the Oxygen Reduction Reaction Mechanism on Carbon

In an attempt to further investigate the ORR mechanism on the thin-film electrodes, the reaction was investigated voltammetrically in both 0.1 M $HClO_4$ and 0.1 M NaOH at scan rates ranging from 1 mV/s to 10 V/s, and amperometrically. All data were background corrected. Unfortunately, only the 5% film was able to be investigated as the ORR overpotential was too large on the other films and no peak was able to be observed at scan rates above 1 mV/s despite background subtracting.

Investigating the ORR by increasing the potential scan rate allows one to assess several parameters. As expected for an irreversible reaction, the reduction peak potential, E_p, shifted negative in a linear fashion with the natural log of the square root of the scan rate, $\ln \nu^{1/2}$, as shown by equation 3.2.6 below.

$$E_p = E^{o'} - \frac{RT}{\alpha n_a F}\left[0.780 + \ln\left(\frac{D_o^{1/2}}{k^0}\right) + \ln\left(\frac{\alpha F \nu}{RT}\right)^{1/2}\right] \quad (3.2.6)$$

Assuming the reaction is irreversible, the peak current, i_p, can be shown to be proportional to the square root of the scan rate, $\nu^{1/2}$, as shown in equation 3.2.7:[54]

$$i_p = 2.99 \times 10^5 n(\alpha n_a)^{1/2} A D_o^{1/2} C_o^* \nu^{1/2} \quad (3.2.7)$$

where n is the stoichiometric number of electrons involved in the reaction, α is the transfer coefficient, n_a is the number of electrons in the rate-determining step, A is the electrode area (assumed here to be 0.2 cm^2, the geometric area), D_o is the diffusion coefficient (1.82 and 2.0 x 10^{-5} cm^2/s in 0.1 M $HClO_4$ and 0.1 M NaOH at 25 °C, respectively),[55,56] and C_o^* is the bulk oxygen concentration (1.3 and 1.15 x 10^{-6} mol/cm^3 in 0.1 M $HClO_4$ and 0.1 M NaOH at 25 °C, respectively).[55,56] Figure 3.12 shows a plot of i_p vs. $\nu^{1/2}$ for the ORR at the 5% CH_4/H_2 film in both acidic and alkaline media. Both plots are relatively linear over the entire range (R^2 = 0.969). Solving equation 3.2.7 to find $n(\alpha n_a)^{1/2}$ results in values of 0.419 and 0.416 for the acidic and alkaline media, respectively.

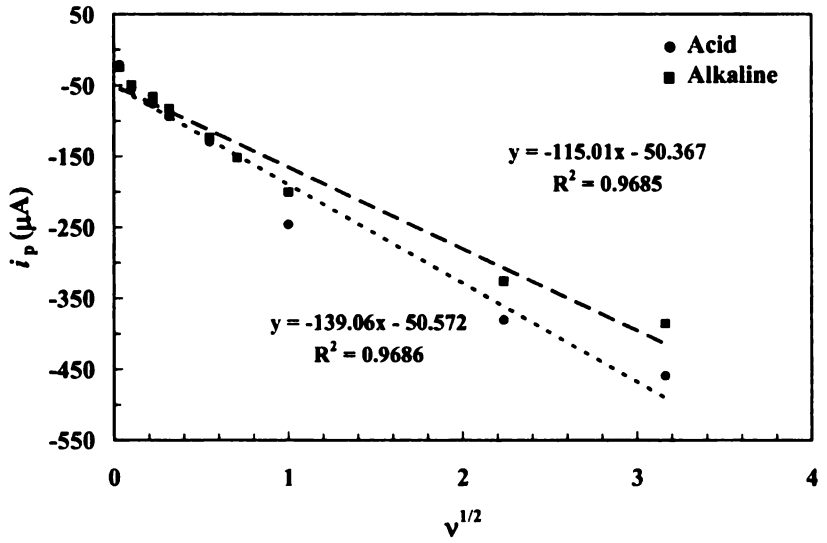

Figure 3.12. Plot of i_p vs. $v^{1/2}$ for ORR in acidic and alkaline media at 5% CH_4/H_2 film.

For an irreversible reaction, the peak current is also known to depend on the standard heterogeneous rate constant, k^0, as shown in equation 3.2.8.

$$i_p = 0.227nFAC_o^* k^0 \exp\left[-\left(\frac{\alpha n_a F}{RT}\right)\left(E_p - E^{o'}\right)\right] \qquad (3.2.8)$$

This equation can then be rearranged to arrive at equation 3.2.9 below.

$$\ln i_p = \ln 0.227nFAC_o^* k^0 - \left(\frac{\alpha n_a F}{RT}\right)\left(E_p - E^{o'}\right) \qquad (3.2.9)$$

Therefore plotting ln i_p vs. ($E_p - E^{o'}$) results in a linear trend with a slope equal to $-(\alpha n_a F/RT)$ and a y-intercept proportional to the rate constant k^0. Assuming the activity coefficient of the two solutions is unity, the E^o values given in equations 3.2.1 and 3.2.2

can be used in place of $E^{o'}$, respectively. The αn_a value can then be calculated using the slope and substituted into the $n(\alpha n_a)^{1/2}$ solution from equation 3.2.7 to find n. Additionally, using the y-intercept, and the calculated n value, k^0 can also be found. All of these quantities are listed in Table 3.9.

Table 3.9. ORR Parameters Obtained from Linear Sweep Voltammetric *i-E* Curves in Acidic and Alkaline Media at a 5% CH_4/H_2 Film

Parameter	0.1 M $HClO_4$	0.1 M NaOH
αn_a	0.24	0.33
n	0.85	0.73
k^0 (cm/s)	1.44×10^{-6}	2.64×10^{-3}

The experimental n value determined for each solution is nearly 1 suggesting that 1-electron is transferred in the irreversible step in the ORR process. The question is why a value of 1 is observed if the literature indicates that $n = 2$ on carbon surfaces? One possibility is that the reaction does not go to completion under these conditions. Perhaps only the initial 1-electron reduction to $O_2^{\bullet -}$ occurs. Another possibility is a surface area less than the assumed area of 0.2 cm^2 participates in the reaction. For example, an active surface area of *ca.* 0.05 cm^2 (or 25% of the geometric area) would yield an αn_a value of ~0.5 assuming $n = 2$. This does not appear likely since n values calculated using chronoamperometric *i-t* curves (discussed below) was found to be ~2 using an assumed area of 0.2 cm^2.

A final source of error is that theory does not adequately describe the ORR process. Equation 3.2.7 is intended for an irreversible 1-electron transfer under semi-

infinite linear diffusion limitations. It is obvious that this reaction is much more complicated and perhaps equations 3.2.7 – 3.2.9 oversimplify the situation. According to the proposed mechanism above, equation 3.2.3 is the only equation limited by semi-infinite linear diffusion. Equations 3.2.4 and 3.2.5 both assume an adsorbed species. Since only the initial 1-electron transfer is limited by semi-infinite linear diffusion, an n value of 1 is perhaps reasonable if the reaction proceeds via reaction 3.2.3. Obviously it is difficult to fit a mixed diffusion/adsorption reaction to a theoretical situation of only semi-infinite linear diffusion.

Additionally, if one assumes $n_a = 1$, then α for the acidic and alkaline media is 0.24 and 0.33, respectively. Since these equations are intended for an oxidation reaction, the value $(1 - \alpha)$ would be more appropriate in this instance. This value for the two media would then be 0.76 and 0.67, respectively. The α in alkaline agrees well with that found by Yang and McCreery for polished GC at a similar pH.[47] The rate constant in the alkaline solution agrees well with that previously determined in solutions of similar pH.[48,52] The reaction rate is several orders slower in the acid solution compared to that of the alkaline solution in agreement with previous reports.[53] Yang and McCreery also noted a decrease in k^0 with decreasing pH. They concluded that at high pH, the rate-determining step (rds) in the reaction was equation 3.2.4. However, at pH < 9, the adsorbed $O_2^{\bullet -}$ protonates to form a relatively stable hydroperoxide analog of ROOH. This species appears to occupy adsorption sites, thus preventing further $O_2^{\bullet -}$ adsorption.

This means that reaction 3.2.3 becomes the rds and proceeds via an outer sphere route.[47] The inhibition for $O_2^{\bullet -}$ to adsorb to the surface results in a decrease in rate constant.

Alternatively, the total number of electrons transferred in the ORR reaction can be determined using a large amplitude potential step technique and fitting the resulting *i-t* profile to the well known Cottrell equation shown in equation 3.2.10 below.

$$i(t) = \frac{nFAD_o^{1/2}C_o^*}{\pi^{1/2}t^{1/2}} \qquad (3.2.10)$$

If the reaction rate is limited by semi-infinite linear diffusion, plotting *i* vs. $t^{-1/2}$ results in a curve with a linear region whose slope is proportional to *n*, and a y-intercept ideally of zero. Using this technique, the value of *n* in both the acidic and alkaline media was found to be 1.8, and 2.2, respectively. These values were found assuming A is the geometric area and are close to the predicted value of 2. This suggests that overestimating the surface area was not the cause of $n = 1$ determined using voltammetric sweeps. These results are consistent with the reaction mechanism proposed in equations 3.2.3 – 3.2.5, with an overall $2e^-$ reduction proceeding through an initial irreversible $1e^-$ step independent of pH.

Exposing the 5% CH_4/H_2 film to the cleaning and rehydrogenating procedure did not significantly affect most of these quantities. The quantities determined from linear sweep voltammetric *i-E* curves in both media after acid-washing and rehydrogenation are

shown in Table 3.10. Cleaning the sp^2-bonded nondiamond carbon off the surface did not alter any of the values in the table to a great extent. This means that the nondiamond carbon removed from the surface does not affect the reaction in either solution. This possibly suggests that the π–π interactions likely promote O_2 adsorption and not the surface nondiamond carbon. This is similar to what was found with the 4-*t*BC redox analyte above. It should be mentioned however, that it is possible that the procedure changes the surface termination but not the bonded carbon. Therefore one can only say that the surface oxygen is definitely removed while possibly some or all of the sp^2 carbon remains.

Table 3.10. ORR Parameters Obtained from Linear Sweep Voltammetric *i-E* Curves in Acidic and Alkaline Media at a 5% CH_4/H_2 Film After Acid-Washing and Rehydrogenating

Parameter	0.1 M $HClO_4$	0.1 M NaOH
αn_a	0.22	0.42
n	1.1	0.75
k^0 (cm/s)	2.93×10^{-6}	1.26×10^{-3}

3.3 Conclusions

The physical and electrochemical properties of boron-doped polycrystalline diamond thin-film electrodes, prepared with varying levels of sp^2-bonded nondiamond carbon impurity, were systematically investigated. This impurity was introduced through adjustment of the CH_4/H_2 source gas ratio used during the deposition. Variations in the morphology and microstructure were monitored using AFM, SEM and Raman spectroscopy. Proportional increases in the fraction of grain boundary, the extent of

secondary nucleation and the sp^2-bonded carbon impurity content occurred with increasing CH_4/H_2 ratio. Additionally, the increased rate of secondary nucleation resulted in progressively smoother films with increasing CH_4/H_2 ratio.

The electrode response was assessed using $Fe(CN)_6^{3-/4-}$, $Ru(NH_3)_6^{3+/2+}$, $Fe^{3+/2+}$, and 4-*tert*-butycatechol (4-*t*BC). While the increasing sp^2-bonded carbon content had little effect on the CV peak separation (ΔE_p) or peak current for the first two redox systems, the impurity had a significant impact on the latter two, as ΔE_p decreased proportionally with the increased sp^2-bonded carbon content. Specifically, the 5% CH_4/H_2 film exhibited a marked improvement in the electrochemical response towards both $Fe^{3+/2+}$ and 4-*t*BC, as compared to the other films. The ΔE_p for this film towards these analytes was several hundred mV less than the ΔE_p for the other films towards these redox couples. It is obvious that the sp^2-bonded nondiamond carbon in this film is quite different from the nondiamond carbon present in the other films, consistent with the Raman spectral data. In fact, supposable removal of the surface nondiamond carbon from the 5% CH_4/H_2 film did not significantly alter the electrochemical response of the electrode towards either $Fe^{3+/2+}$ or 4-*t*BC. This means that the electrochemical response is a constituent of the microstructure (sp^3/sp^2 carbon mixture) and not just a surface impurity. It is also possible that the hydrogen plasma either failed to completely remove the nondiamond carbon or the oxygen-free surface completely oxidized upon air exposure. It is clear that the nondiamond carbon affects the reaction kinetics, likely by providing sites for strong adsorption and sites where catalyzing carbon-oxygen functional groups can form.

The effect of the nondiamond carbon impurity on the ORR in 0.1 M $HClO_4$ and 0.1 M NaOH was also investigated. A direct correlation was found between the relative amount of the impurity, as estimated from Raman spectroscopy, and the overpotential for the reaction. The greater the nondiamond content, the lower the kinetic overpotential for the reduction reaction and the higher the exchange current density were. The composite electrodes exhibited greater activity in alkaline solutions than in acid. The microstructure of the nondiamond carbon appears to influence the reaction, particularly in acid, as removing nondiamond carbon from the surface of the 5% CH_4/H_2 film did not significantly alter the ORR mechanism. Tafel plots yielded an apparent exchange current density that increased and a transfer coefficient that decreased with the increased nondiamond carbon content. The results indicate that the grain boundaries, and the sp^2 carbon impurity presumably residing there, can have a profound impact on the electrode-reaction kinetics for certain redox systems, while for others this impurity has little influence on the diamond electrode response.

REFERENCES

1. J. Xu, M. C. Granger, Q. Chen, J. W. Strojek, T. E. Lister, and G. M. Swain, *Anal. Chem.*, **69**, 591A (1997).

2. G. M. Swain, A. B. Anderson, and J. C. Angus, *MRS Bull.*, **23**, 56 (1998).

3. M. C. Granger, J. Xu, J. W. Strojek, and G. M. Swain, *Anal. Chim. Acta*, **397**, 145 (1999).

4. M. C. Granger, M. Witek, J. Xu, J. Wang, M. Hupert, A. Hanks, M. D. Koppang, J. E. Butler, G. Lucazeau, M. Mermoux, J. W. Strojek, and G. M. Swain, *Anal. Chem.*, **72**, 3793 (2000).

5. A. E. Fischer, Y. Show, and G. M. Swain, *Anal. Chem.*, **76**, 2553 (2004).

6. Y. Show, M. A. Witek, P. Sonthalia, and G. M. Swain, *Chem. Mater.*, **15**, 879 (2003).

7. M. Hupert, A. Muck, J. Wang, J. Stotter, Z. Cvackova, S. Haymond, Y. Show, and G. M. Swain, *Diamond and Rel. Mater.*, **12**, 1940 (2003).

8. H. Gerischer, *Electrochim. Acta*, **35**, 1677 (1990).

9. J. Wang, G. M. Swain, M. Mermoux, G. Lucazeau, J. Zak, and J. W. Strojek, *New Diamond Front. Carbon Technol.*, **9**, 317 (1999).

10. T. N. Rao, T. A. Ivandini, C. Terashima, B. V. Sarada, and A. Fujishima, *New Diamond Front. Carbon Technol.*, **13**, 79 (2003).

11. H. B. Martin, A. Argoitia, U. Landau, A. B. Anderson, and J. C. Angus, *J. Electrochem. Soc.*, **143**, L133 (1996).

12. J. Wang and G. M. Swain, *J. Electrochem. Soc.*, **150**, E24 (2003).

13. Y. V. Pleskov, *Russ. Chem. Rev.*, **68**, 381 (1999).

14. L.-F. Li, D. A. Totir, N. Vinokur, B. Miller, G. Chottiner, E. A. Evans, J. C. Angus, and D. A. Scherson, *J. Electrochem. Soc.*, **145**, L85 (1998).

15. I. Duo, A. Fujishima, and C. Comninellis, *Electrochem. Commun.*, **5**, 695 (2003).

16. K. Yoo, B. Miller, K. Rafi, and X. Shi, *Electrochem. Solid-State Lett.*, **2**, 233 (1999).

17. M. Mermoux, B. Marcus, G. M. Swain, and J. E. Butler, *J. Phys. Chem. B*, **106**, 10816 (2002).

18. W. A. Yarbrough and R. Messier, *Science*, **247**, 688 (1990).

19. D. S. Knight and W. B. White, *J. Mater. Res.*, **4**, 385 (1989).

20. R. E. Shroder, R. J. Nemanich, and J. T. Glass, *Phys. Rev. B*, **41**, 3738 (1990).

21. M. Silveira, M. Becucci, E. Castellucci, F. Polla Mattiot, V. Barbarossa, R. Tomaciello, and F. Galluzzi, *Diamond and Rel. Mater.*, **2**, 1257 (1993).

22. K. G. Ray III and R. L. McCreery, *J. Electroanal. Chem.*, **469**, 150 (1999).

23. K. Ushizawa, K. Watanabe, T. Ando, I. Sakagucki, M. Nishitani-Gamo, Y. Sato, and H. Kanada, *Diamond and Rel. Mater.*, **7**, 1719 (1998).

24. J. R. Dennison, M. Holta, and G. M. Swain, *Spectroscopy (Amsterdam)*, **11**, 38 (1996).

25. M. C. Rossi, *Appl. Phys. Lett.*, **73**, 1203 (1998).

26. C. S. Feigerle and R. W. Shaw, *Opt. Photonics News*, **7**, 24 (1996).

27. L. H. Robins, E. N. Farabaugh, and A. Feldman, *J. Mater. Res.*, **5**, 2456 (1990).

28. B. Marcus, L. Fayette, M. Mermoux, L. Abello, and G. Lucazeau, *J. Appl. Phys.*, **76**, 3463 (1994).

29. N. Wada, P. J. Gaczi, and S. A. Solin, *J. Non-Cryst. Solids*, **35 & 36**, 543 (1980).

30. R. L. McCreery and R. T. Packard, *Anal. Chem.*, **61**, 775A (1989).

31. R. L. McCreery, in *Neuromethods*, A. Boulton, G. Baker, and R. N. Adams, Editors, **27**, p. 1, Humana Press, Inc., Totowa, NJ, (1995).

32. I.-F. Hu, D. Karweik, and T. Kuwana, *J. Electroanal. Chem. Interfacial Electrochem.*, **188**, 59 (1985).

33. J. F. Evans and T. Kuwana, *Anal. Chem.*, **49**, 1632 (1977).

34. J. F. Evans and T. Kuwana, *Anal. Chem.*, **51**, 358 (1979).

35. C. W. Miller, D. H. Karwelk, and T. Kuwana, *Anal. Chem.*, **53**, 2319 (1981).

36. D. T. Fagan, I. F. Hu, and T. Kuwana, *Anal. Chem.*, **57**, 2759 (1985).

37. R. J. Rice, N. M. Pontikos, and R. L. McCreery, *J. Am. Chem. Soc.*, **112**, 4617 (1990).

38. K. R. Kneten and R. L. McCreery, *Anal. Chem.*, **64**, 2518 (1992).

39. P. Chen, M. A. Fryling, and R. L. McCreery, *Anal. Chem.*, **67**, 3115 (1995).

40. P. Chen and R. L. McCreery, *Anal. Chem.*, **68**, 3958 (1996).

41. H.-H. Yang and R. L. McCreery, *Anal. Chem.*, **71**, 4081 (1999).

42. S. H. DuVall and R. L. McCreery, *J. Am. Chem. Soc.*, **122**, 6759 (2000).

43. M. C. Granger and G. M. Swain, *J. Electrochem. Soc.*, **146**, 4551 (1999).

44. C. A. McDermott, K. R. Kneten, and R. L. McCreery, *J. Electrochem. Soc.*, **140**, 2593 (1993).

45. Q. Chen and G. M. Swain, *Langmuir*, **14**, 7017 (1998).

46. J. Xu, Q. Chen, and G. M. Swain, *Anal. Chem.*, **70**, 3146 (1998).

47. H.-H. Yang and R. L. McCreery, *J. Electrochem. Soc.*, **147**, 3420 (2000).

48. J. Xu, W. Huang, and R. L. McCreery, *J. Electroanal. Chem.*, **410**, 235 (1996).

49. I. Morcos and E. Yeager, *Electrochim. Acta*, **15**, 953 (1970).

50. E. Yeager, *Electrochim. Acta*, **29**, 1527 (1984).

51. A. J. Appleby and J. Marie, *Electrochim. Acta*, **24**, 195 (1979).

52. T. Yano, D. A. Tryk, K. Hashimoto, and A. Fujishima, *J. Electrochem. Soc.*, **145**, 1870 (1998).

53. T. Yano, E. Popa, D. A. Tryk, K. Hashimoto, and A. Fujishima, *J. Electrochem. Soc.*, **146**, 1081 (1999).

54. A. J. Bard and L. R. Faulkner, *Electrochemical Methods: Fundamentals and Applications*, John Wiley & Sons, Inc., New York (2001).

55. N. Wakabayashi, M. Takeichi, M. Itagaki, H. Uchida, and M. Watanabe, *J. Electroanal. Chem.*, **574**, 339 (2005).

56. B. Case, *Electrochim. Acta*, **18**, 293 (1973).

CHAPTER 4

Investigating Microcrystalline and Nanocrystalline Boron-Doped Diamond as a Corrosion Resistant Advanced Electrocatalyst Support Material

4.1 Introduction

Electrocatalytic electrodes are used in industrial processes (*e.g.*, electrosynthesis) and energy conversion devices (*e.g.*, fuel cells).[1,2] Such electrodes consist of nanometer-sized metallic (*e.g.*, Pt) or metal alloy particles supported on a chemically inert, electrically conductive support material. The current support material, at least for fuel cells, is sp^2 bonded carbon (*e.g.*, physically or chemically activated carbon or carbon black).[3] An ideal electrocatalyst support material possesses several properties including (*i*) electrical conductivity (>10 S/cm), (*ii*) high surface area (>100 m^2/g), (*iii*) chemical stability in aqueous environments, (*iv*) thermal stability up to 200 °C and (*v*) morphological and microstructural stability at high potentials and current densities (*e.g.*, >1 V vs. the standard hydrogen electrode (SHE) and several A/cm^2, respectively).[4] Additionally, the materials used should not be overly expensive. Current sp^2 carbon support materials possess the first four properties; however, they are limited by both their microporosity and susceptibility to microstructural degradation (*i.e.*, oxidation and corrosion) at high temperatures, potentials and currents.[3,5] The microporosity of some supports limits the accessibility of the electrochemical reactant gases to all of the surface. Support degradation leads to decreased catalytic activity because of catalyst detachment,

aggregation, and/or fouling by gasification products. If the degradation is severe enough, complete electrode failure can result.

Ongoing research in our laboratory is focused in the long-term on developing electrically conducting polycrystalline diamond as an advanced electrocatalyst support material.[6-10] Diamond possesses several properties desirable for a support material including: (*i*) electrical conductivity when highly doped with boron atoms, (*ii*) low cost due to advances in diamond production, (*iii*) thermal stability at elevated temperatures, (*iv*) corrosion resistance and (*v*) dimensional stability at high potentials and current densities (*e.g.*, >1 V and 1-10 A/cm^2, respectively).[11-14] In order to make diamond a viable support material, two technical challenges remain to be overcome: the formation of electrically conducting diamond in a high surface area architecture and establishment of a protocol for depositing and stabilizing highly dispersed electrocatalyst particles on the diamond surface.

There are currently two types of polycrystalline diamond being investigated in our laboratory: microcrystalline (>1 μm crystallite size) and nanocrystalline (~10 to 20 nm crystallite size). Each possesses a different morphology and microstructure but both exhibit similar electrical conductivity and electrochemical activity when highly doped with boron. Our group has previously investigated metal phase formation on microcrystalline diamond using both dc sputtering and electrochemical deposition at constant potential or current.[6-9] Electrodeposition was found to be the superior method because it allowed for better control of the deposition process (*i.e.*, particle properties)

and placed particles solely in areas of the diamond that were electrically conductive. The particles were then physically anchored to the surface via a short secondary microcrystalline diamond growth procedure. These films were tested during exposure to conditions commonly experienced by the carbon electrodes in phosphoric acid fuel cells (PAFCs) and were found to exhibit stability far superior to that of commonly used sp^2 carbon support material.[8]

Additionally, very recent findings in our laboratory suggest that nanocrystalline diamond may be a more promising support material then microcrystalline diamond for several reasons. First, depositing metal using a pulsed galvanostatic approach (see Chapters 5 and 6) produced particles with more desirable properties in terms of size, density and electrocatalytic activity towards the oxygen reduction reaction (the cathode reaction in fuel cells) in acidic media compared to similarly deposited particles on the microcrystalline diamond.[15,16] Additionally, metal phase formation on nanocrystalline diamond has been shown to be better for anodic stripping voltammetric applications.[17,18]

Second, while a short secondary microcrystalline diamond growth procedure proved effective in stabilizing metal particles that were 50-300 nm in size, a similar secondary microcrystalline diamond growth procedure used to stabilize particles that were an order of magnitude smaller resulted in complete coverage of several particles (*i.e.*, lost catalyst activity) as well as some particle agglomeration.[15] This will be presented in detail in section 5.2.5 of this dissertation. Nanocrystalline diamond is composed of diamond crystallites (*i.e.*, grains) that are much smaller than those possessed

by microcrystalline diamond. If the nanocrystalline diamond is indeed stable, than perhaps it could also serve to physically anchor the smaller particles to the diamond surface without completely covering them. Additionally, the lower growth temperatures and higher nucleation rate for nanocrystalline diamond deposition could also inhibit particle agglomeration during the secondary diamond growth.

Finally, we have recently taken a step toward our quest to develop electrically conductive diamond possessing a high surface area. We coated sp^2 carbon paper with boron-doped nanodiamond to produce a diamond electrode with considerably higher surface area.[19] This material, shown in Figure 4.1, was stable during 1 h potentiostatic polarization in 0.1 M $HClO_4$ at 1.6 V vs. Ag/AgCl and 25 °C.[19] The low H_2 content in the gas phase of the nanocrystalline diamond growth made it possible to coat the sp^2 carbon paper due to the rate of diamond deposition being higher than the rate of carbon etching due to H_2. It is likely that with smaller carbon fibers, the diamond surface area could be further increased. While the surface area of this material is still too low for practical applications, it is a step in the right direction.

We report herein on a comprehensive investigation of the morphological and microstructural stability of both microcrystalline and nanocrystalline boron-doped diamond thin films (n = 3 different films for each diamond type). Each diamond electrode was exposed to polarization conditions commonly observed in PAFCs (85 wt% H_3PO_4, 180 °C, 0.1 A/cm^2) for 2 h. The films were characterized using atomic force (AFM) and scanning electron (SEM) microscopy and Raman spectroscopy. Changes in

the diamond surface chemistry were indirectly tracked using contact angle measurements with ultrapure H_2O. Changes in the electrochemical properties of the films were investigated using cyclic voltammetry in supporting electrolyte (0.1 M $HClO_4$) and in the presence of several common redox systems (*e.g.*, $Fe(CN)_6^{3-/4-}$, $Ru(NH_3)_6^{3+/2+}$, and $Fe^{3+/2+}$).

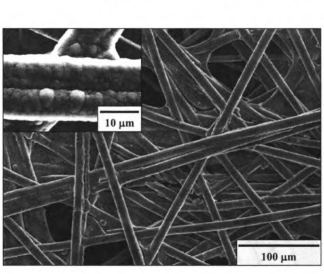

Figure 4.1. Scanning electron micrograph of Toray carbon paper coated with boron-doped nanocrystalline diamond. Inset is of similar growth at higher magnification.

4.2 Microcrystalline Diamond Results & Discussion

The stability of the physical, chemical, and electrochemical properties of microcrystalline diamond thin film was assessed. Specifically, the electrodes were characterized initially, after a 2 h anodic polarization treatment at 0.1 A/cm^2 and *ca.* 180 ^oC in 85 wt% H_3PO_4, and after a 30 min H_2 plasma treatment.

4.2.1 Physical Properties

The surface morphology of microcrystalline diamond was investigated before and after anodic polarization using scanning electron and atomic force microscopy. Figure

4.2 shows scanning electron micrographs of a microcrystalline diamond film before (A) and after (B) the anodic polarization treatment. As expected, there is no catastrophic degradation of the diamond microstructure; however there is some roughening of the facets and the grain edges as can be seen in the slightly higher magnification image (Figure 4.2B).

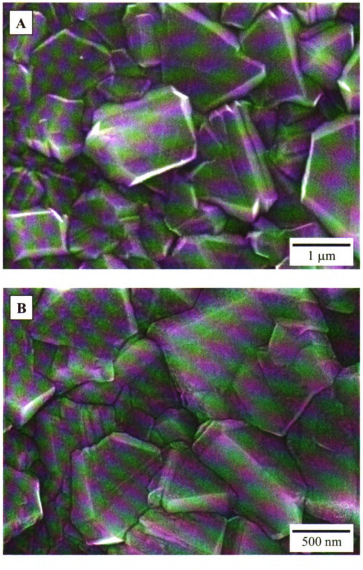

Figure 4.2. Scanning electron micrographs of boron-doped microcrystalline diamond (A) before and (B) after anodic polarization.

Figure 4.3 shows 2 x 2 μm atomic force micrographs obtained (A) before and (B) after anodic polarization. Clearly, the exposure to the corrosive conditions results in some minor film roughening of the facet surfaces, but there is no gross morphological damage or film debonding. This agrees well with the SEM images. Two parameters that quantitate the surface roughness are the real image surface area (as opposed to the geometric surface area) and the image RMS roughness which is defined as the absolute value of the average height and depth away from the zero line (set point *ca.* -2 V). The average value for the roughness factor (RF = real area/geometric area) as a function of image size before and after anodic polarization, is summarized in Table 4.1. On average, the real surface area was 15 ± 2% larger than the geometric area (RF_{avg} = 1.15). This did not significantly increase after anodic polarization as a value of 18 ± 3% was observed (RF_{avg} = 1.18). The RMS roughness also showed little change before and after polarization. The RMS roughness value was initially 110 ± 16 nm and after anodic polarization changed little with a value of 105 ± 23 nm. These microscopic data suggest that the diamond is dimensionally stable under these conditions as there was no film debonding, pitting or cracking.

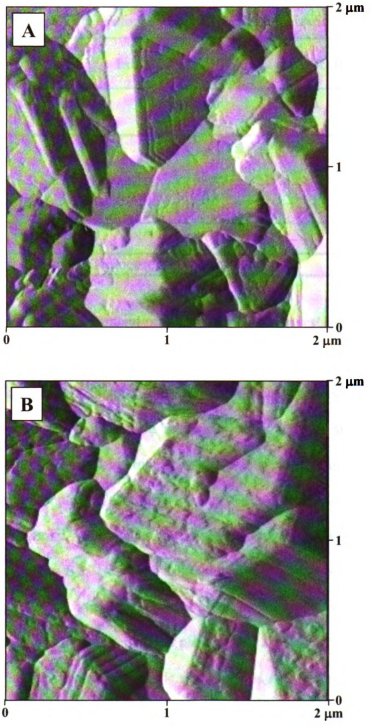

Figure 4.3. Atomic force micrographs (2 x 2 µm) of a boron-doped microcrystalline diamond thin film (A) before and (B) after anodic polarization.

Table 4.1. Comparison of the Real and Geometric Areas of Boron-Doped Microcrystalline Diamond Films Before and After Anodic Polarization

Geometric Surface Area (μm^2)	Initial		Anodically Polarized	
	Real SA (μm^2)	Roughness Factor[a]	Real SA (μm^2)	Roughness Factor[a]
4	4.6 ± 0.1	1.15	4.8 ± 0.1	1.20
25	29.0 ± 0.6	1.16	29.5 ± 0.3	1.18
100	115 ± 1	1.15	116.7 ± 0.8	1.17
RF_{avg}	–	**1.15**	–	**1.18**

[a] Roughness Factor = Real SA/Geometric SA

The microcrystalline diamond microstructure was investigated using Raman spectroscopy. Figure 4.4 shows representative spectra for a film before and after anodic polarization. As discussed in Chapter 3, Raman spectroscopy is sensitive to changes in the diamond microstructure including the relative levels of sp^2- and sp^3-bonded carbon, the atomic ordering and residual internal stress. These spectra are quite different from the one presented in Figure 3.2 for high quality (*i.e.*, low nondiamond sp^2 carbon impurity content) diamond. This is due to the significantly higher doping level in this particular film, as gaseous B_2H_6 was used as the dopant source instead of the solid B_2O_3 diffusion source. The high boron-doping level increases the tensile stress in the film as evidenced by the down-shift in the diamond phonon peak from 1332 to *ca.* 1323 cm^{-1}.[20] Wang *et al.* attributed this increase in tensile stress to a high defect density introduced by the blocking of grain boundary sliding during polycrystalline diamond growth.[20] The asymmetry of the diamond phonon band is possibly due to a Fano interference induced

by quantum mechanical interference between the discrete phonon state and the electronic continuum.[21]

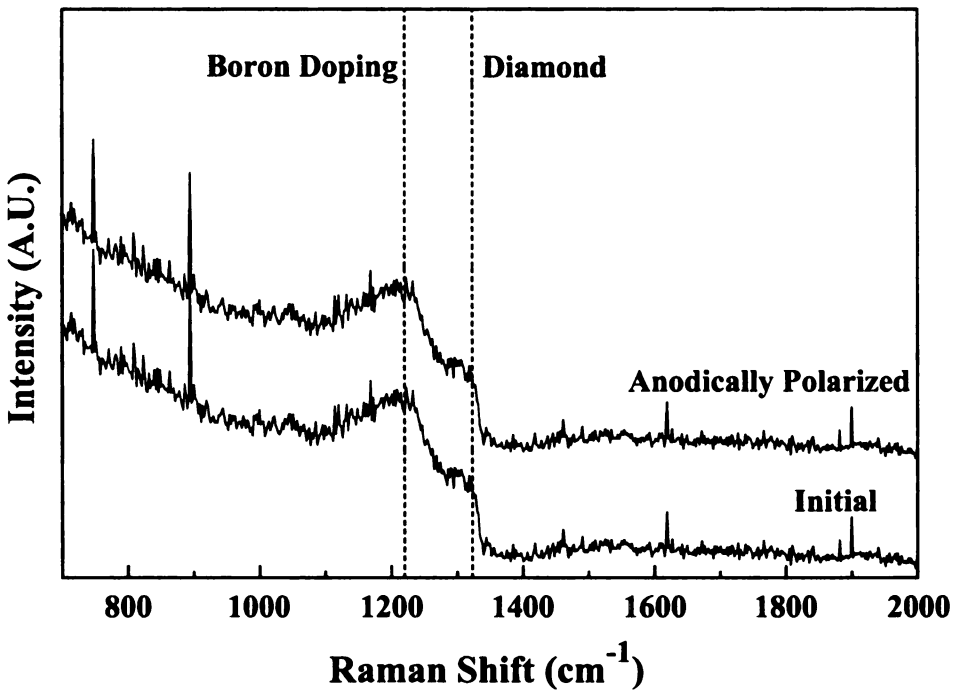

Figure 4.4. Raman spectra of heavily boron-doped microcrystalline diamond initially and after anodic polarization. Dotted lines correspond to boron doping and diamond signals, respectively. Spectra are off-set for viewing clarity.

The spectrum for a highly doped diamond film shown in Figure 4.4 also displays a broad band at ~1220 cm^{-1}. This band has been previously observed along with a down-shift of the diamond phonon peak for films possessing boron concentrations $>10^{20}$ B/cm^3.[22] Gonon *et al.* attributed this band to a maxima in the phonon density of states originating from disordered regions or regions of very small crystallite size.[22] The dotted lines in Figure 4.4 denote the down-shifted diamond phonon band and high boron concentration band at 1323 and 1220 cm^{-1}, respectively.

There is no observable difference in the spectral features before and after anodic polarization, specifically in terms of the diamond peak position or the presence of sp^2-bonded nondiamond carbon. This indicates that the diamond microstructure and optical properties were largely unaffected by the polarization. The initial average diamond peak position for the film was 1320 ± 3 cm^{-1}. Anodic polarization did not significantly alter this value as the average position was 1324 ± 3 cm^{-1}. The down-shifted peak is consistent with the region of the film probed being under tensile stress. The line width (FWHM) of the diamond phonon peak is a qualitative indicator of the crystalline film quality.[23,24] However, the presence of the boron signal in the higher doped films makes it difficult to measure. Regardless, efforts were made to estimate this value as best as possible. Values of 31 ± 6 cm^{-1} and 30 ± 5 cm^{-1} were obtained before and after anodic polarization, respectively. Comparatively, the FWHM measured for a piece of single crystal diamond under the same settings was 5-7 cm^{-1}. According to Gonon *et al.*, FWHM values of 16 and 40 cm^{-1} were measured for CVD diamond/Si samples possessing boron concentrations of 1.8 x 10^{20} and 1.1 x 10^{21} B/cm^3, respectively.[22]

We recently measured the boron concentration in a microcrystalline diamond film grown with 10 ppm B_2H_6 in the source gas using boron nuclear reaction analysis (BNR). The B/C concentration was determined to be 2036 ppm. Assuming an atomic density of 1.76 x 10^{23} $atoms/cm^3$ for diamond, this equates to a value of 3.6 x 10^{20} B/cm^3. This value agrees well with that deduced from the FWHM analysis discussed above. Additionally, powder x-ray diffraction spectra identified diamond crystallite orientations of (111), (220) and (311) for films grown in our laboratory. This means our value also

agrees well with that of Ushizawa *et al.* who found the boron concentration in the (111) facet of a 2000 ppm CVD diamond/Si sample to be 2.3 x 10^{21} B/cm^3 using secondary ion mass spectrometry (SIMS).[21]

4.2.2 Surface Chemistry

The surface chemistry (*i.e.*, oxide content) was investigated by measuring the instantaneous contact angle for a 10 μL drop of ultrapure water interacting with the diamond surface. Initially, the hydrogen-terminated diamond surface was hydrophobic and, as expected, exhibited a high instantaneous contact angle of 69 ± 4°. The diamond surface was expected to become more hydrophilic after anodic polarization. Such a change should be manifested in a decreased water contact angle. However, the contact angle did not decrease significantly, only to a value of 61 ± 4°. These values agree well with those of Ostrovskaya *et al.*[25] However, following the rehydrogenation procedure, the contact angle substantially increased to 101 ± 7°, suggesting the original surface contained some carbon-oxygen functionalities. Again this is in agreement with Ostrovskaya *et al.* and Pinzari *et al.*[25,26] Based on this indirect measurement, the surface oxygen content increased some, but not significantly, after polarization. The values are summarized in Table 4.2. The difference in the contact angles for the film before and after rehydrogenation is likely due to exposure of the electrode to the laboratory atmosphere. As described in Chapter 2, our diamond deposition procedure involves a slow cool down in an H_2 plasma (*i.e.*, atomic hydrogen) in order to etch away adventitious nondiamond carbon impurity, minimize dangling bonds, and terminate the diamond surface with hydrogen atoms. Prior to the initial contact angle measurements,

the diamond films had been exposed to the laboratory atmosphere for a considerable period of time (*i.e.*, days or even weeks) and slowly oxidized. Recent XPS data revealed that films exposed to atmospheric conditions for a similar amount of time exhibited an O/C ratio of ~0.05. Assuming a sampling depth of 5 layers, this is consistent with a surface coverage of 0.25. Additionally, Ostrovskaya *et al.* obtained similar contact angles for naturally oxidized diamond films.[25] The final set of contact angle data was obtained immediately following the rehydrogenation process, before the diamond surface had a chance to oxidize.

Table 4.2. Summary of Contact Angle Measurements for Ultrapure Water on Boron-Doped Microcrystalline Diamond Thin Film as a Function of the Surface Chemistry

Diamond Condition	Initially	Anodically Polarized	Rehydrogenated
Contact Angle	69 ± 4°	61 ± 4°	101 ± 7°
Percent Change	–	-12%	+66%

4.2.3 Electrochemical Response

Cyclic voltammetric *i-E* curves in 0.1 M $HClO_4$ (N_2 purged) were obtained before, after anodic polarization and after rehydrogenation. Representative examples are shown in Figure 4.5. All the curves are flat and featureless between the regions of solvent breakdown. The potential window data, determined from measurement of three microcrystalline electrodes at ±50 μA or ±250 μA/cm^2, are summarized in Table 4.3. Prior to polarization, the average potential window was 2.9 ± 0.1 V. Anodically polarizing the diamond surface did not affect the potential window as the average remained 3.0 ± 0.2 V. The similarity of these values suggests that the diamond films

possessed minimal sp^2 carbon content on the surface initially. Nondiamond sp^2 carbon phases tend to reduce the potential window.[27] Anodic polarization removes such carbon resulting in an increased window. The potential window was also not altered much following the rehydrogenation as the nominal value was 3.05 ± 0.01 V.

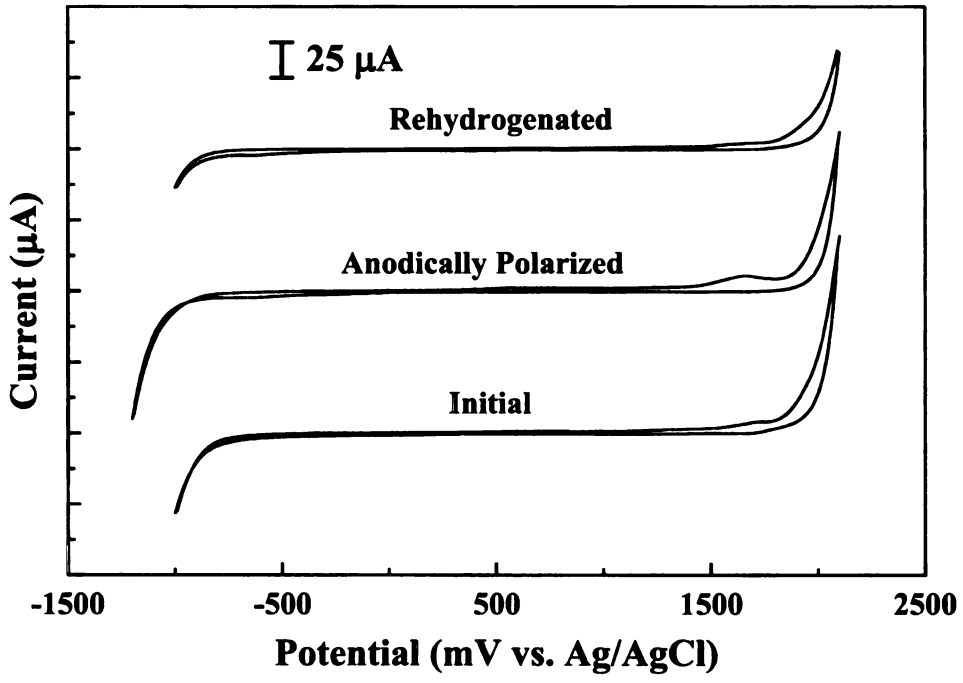

Figure 4.5. Background cyclic voltammetric *i-E* curves for microcrystalline diamond films in degassed 0.1 M $HClO_4$ as a function of the surface condition. Scan Rate = 100 mV/s.

The anodic background current was also recorded at a potential of 400 mV; a potential at which the current is mostly nonfaradaic. The background current magnitude for each film after the different treatment was quite similar. Values of 0.7 ± 0.1, 0.8 ± 0.1 and 0.72 ± 0.03 μA were obtained for the initial, anodically polarized, and rehydrogenated films, respectively. The similar values indicated that neither the anodic

polarization nor the rehydrogenation roughens the surface, consistent with the microscopy.

Table 4.3. Potential Window and Background Current Measured from Cyclic Voltammetric *i-E* Curves for a Boron-Doped Microcrystalline Diamond Thin Film in 0.1 M $HClO_4$ at a Scan Rate of 100 mV/s

Diamond Condition	Potential Window (V)[a]	Background Current (μA)
Initial	2.9 ± 0.1	0.7 ± 0.1
Anodically Polarized	3.0 ± 0.1	0.8 ± 0.1
Rehydrogenated	3.05 ± 0.01	0.72 ± 0.03

[a] Potential window is defined as ±50 μA or ±250 $\mu A/cm^2$

The electrochemical response for the microcrystalline diamond films towards several well known redox analytes was also measured before and after the treatments. Figure 4.6A-C shows representative cyclic voltammetric *i-E* curves for $Fe(CN)_6^{3-/4-}$, $Ru(NH_3)_6^{3+/2+}$ and $Fe^{3+/2+}$ at a microcrystalline diamond before, after anodic polarization and after rehydrogenation. The basis for the selection of these analytes as redox probes was given in section 3.2.2. Figure 4.6A shows voltammetric *i-E* curves for $Fe(CN)_6^{3-/4-}$. $Fe(CN)_6^{3-/4-}$ is an inner-sphere redox system (*i.e.*, specific analyte-surface interaction required for electron transfer) with a heterogeneous electron-transfer rate constant that is sensitive to the electronic properties, surface cleanliness and the presence of surface oxides on diamond electrodes.[14,27,28] In other words, ΔE_p increases from the reversible value of 60 mV if the film has poor electrical conductivity, an unclean surface or surface oxygen functionalities. The largest rate constant (*i.e.*, smallest ΔE_p) is seen for the clean hydrogen-terminated surface. The potential peak separation, ΔE_p, at each scan rate is displayed in Table 4.4. The ΔE_p at 100 mV/s before and after rehydrogenation were both

65 ± 2 mV, near Nernstian, suggesting that these surfaces were both clean and hydrogen-terminated. This value increased considerably to 91 ± 7 mV after anodic polarization, during which some surface oxygen functional groups are introduced.[28] It appears that oxides formed on the diamond surface somehow block sites that are active toward this reaction when H-terminated. Our group has previously determined this blocking effect to be of electrostatic origin as the ΔE_p for this reaction was directly proportional to the electrolyte pH for an oxidized diamond surface (*i.e.*, protonation of the surface oxides).[28]

Table 4.4. Cyclic Voltammetric Peak Potential Separation (ΔE_p) for 1 mM $Fe(CN)_6^{3-/4-}$ in 1 M KCl at Boron-Doped Microcrystalline Diamond as a Function of the Surface State

Scan Rate	ΔE_p for $Fe(CN)_6^{3-/4-}$ (mV)		
	Initially	**Anodically Polarized**	**Rehydrogenated**
50	65 ± 0	85 ± 6	64 ± 1
100	65 ± 2	91 ± 7	65 ± 2
300	71 ± 2	112 ± 7	73 ± 1
500	78 ± 3	129 ± 9	79 ± 2

Curves for $Ru(NH_3)_6^{3+/2+}$ at a diamond film before, after anodic polarization and after rehydrogenation are shown in Figure 4.6B. $Ru(NH_3)_6^{3+/2+}$ is an outer-sphere redox system (*i.e.*, no specific interaction with the surface) with a rate constant that is sensitive to the electronic properties but relatively insensitive to the surface cleanliness or oxide content. The data are summarized in Table 4.5. Clearly, ΔE_p is unchanged for all the films and is near the Nernstian value of 60 mV at 100 mV/s. This means that the electronic properties of the diamond are metallic-like and unaltered by the treatments.

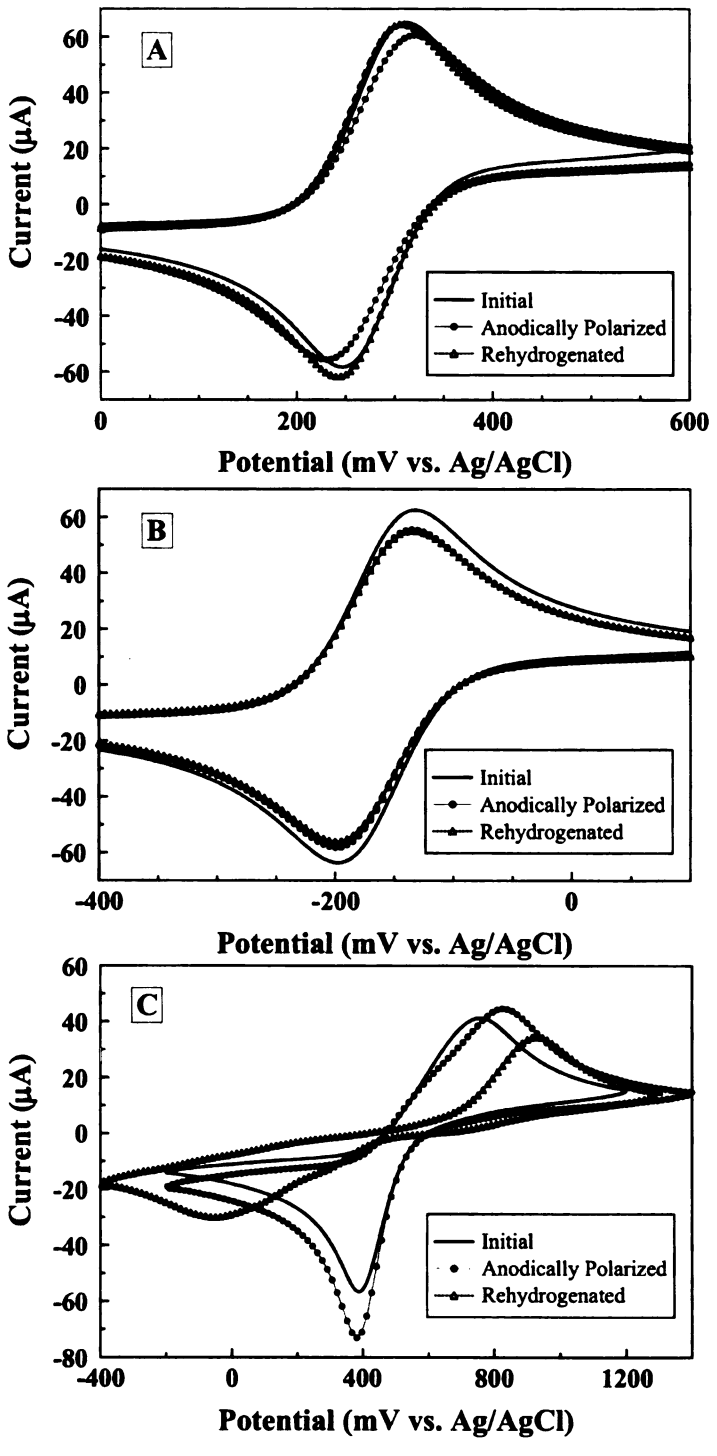

Figure 4.6. Cyclic voltammetric *i-E* curves for boron-doped microcrystalline diamond films before, after anodic polarization and after rehydrogenation in the presence of (A) $Fe(CN)_6^{3-/4-}$, (B) $Ru(NH_3)_6^{3+/2+}$ and (C) $Fe^{3+/2+}$. Scan Rate = 100 mV/s.

Table 4.5. Cyclic Voltammetric Peak Potential Separation (ΔE_p) for 1 mM $Ru(NH_3)_6^{3+/2+}$ in 1 M KCl at Boron-Doped Microcrystalline Diamond as a Function of the Surface State

Scan Rate	ΔE_p for $Ru(NH_3)_6^{3+/2+}$ (mV)		
	Initially	Anodically Polarized	Rehydrogenated
50	64 ± 1	66 ± 1	65 ± 1
100	65 ± 3	66 ± 2	66 ± 1
300	72 ± 2	72 ± 3	73 ± 4
500	76 ± 2	74 ± 2	80 ± 3

The voltammetric *i-E* curves for $Fe^{3+/2+}$ are shown in Figure 4.6C. The $Fe^{3+/2+}$ couple is an inner-sphere redox system with a rate constant that is known to be sensitive to electronic properties, surface cleanliness and surface oxide content, particularly carbonyl functional groups (*e.g.*, C=O). In general, the ΔE_p values for this redox system are much larger than for $Fe(CN)_6^{3-/4-}$ and $Ru(NH_3)_6^{3+/2+}$ reflecting slower electron transfer kinetics. There apparently is a large activation energy barrier to adjust the solvation sphere around the metal when going from the +2 to +3 oxidation state.[29,30] The data are summarized in Table 4.6. The peak separation for the film initially was 380 ± 60 mV. This separation increased some after anodic polarization to 460 ± 80 mV. This would be consistent with few carbonyl functional groups being introduced onto the surface, based on the work by McCreery.[31] The peak separation increased significantly after rehydrogenation to 700 ± 240 mV (note the large variance). Most, if not all, the oxygen functionalities present on the surface before or after anodic polarization were removed by the H_2 plasma treatment. Even though this surface is highly electrically conductive, the electron-transfer kinetics is quite sluggish for reasons that remain unclear. It could be

that the hydrophobic diamond surface provides an additional barrier to reorganization of the solvent sphere surrounding the metal center during the redox event.

Table 4.6. Cyclic Voltammetric Peak Potential Separation (ΔE_p) for 1 mM $Fe^{3+/2+}$ in 0.1 M $HClO_4$ at Boron-Doped Microcrystalline Diamond as a Function of the Surface State

Scan Rate	ΔE_p for $Fe^{3+/2+}$ (mV)		
	Initially	Anodically Polarized	Rehydrogenated
50	330 ± 60	390 ± 100	660 ± 220
100	380 ± 60	460 ± 80	700 ± 240
300	460 ± 60	530 ± 90	800 ± 250
500	500 ± 60	580 ± 80	840 ± 250

The forward reaction peak current for the $Fe(CN)_6^{3-/4-}$ and $Ru(NH_3)_6^{3+/2+}$ redox systems at all the surfaces varied proportionally with scan rate$^{1/2}$ ($\nu^{1/2}$) ($r^2 > 0.999$) consistent with a redox reaction rate limited by semi-infinite diffusional mass transport of reactant to the electrode surface. Since the reactions are nearly reversible for these two redox systems (ΔE_p is near 59 mV), the peak current ratio is 1.0, as expected. The i_p^{ox}/i_p^{red} ratio for $Fe^{3+/2+}$ couple however was less than 1.0, generally *ca.* 0.7. The forward oxidation peak current scaled linearly with $\nu^{1/2}$ ($r^2 > 0.999$) also expected for a kinetically irreversible reaction.

4.3 Nanocrystalline Diamond Results & Discussion

4.3.1 Physical Properties

The physical, chemical and electrochemical properties of boron-doped nanocrystalline diamond thin film were evaluated before, after anodic polarization and

after rehydrogenation. Figure 4.7 shows a typical SEM image of a nanocrystalline diamond thin film after anodic polarization. Clearly, there is no large scale bulk degradation or pitting on the surface. Macroscopically, the film looks the same before and after polarization.

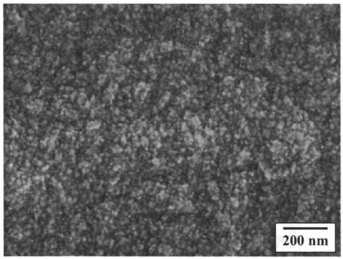

Figure 4.7. Scanning electron micrograph of boron-doped nanocrystalline diamond film after anodic polarization.

The atomic force micrographs shown in Figure 4.8A and B also do not indicate any visible morphological change to the film after the polarization. The images appear slightly grainy which may indicate some minor roughening or pitting. Atomic force micrographs were obtained over geometric areas of 0.25, 4, and 25 μm^2. The difference between the geometric area and actual surface area, summarized in Table 4.7, as well as the RMS roughness for the initial and polarized nanocrystalline diamond films were used to probe for changes in the microscopic surface roughness. Comprehensively, the real area for all the images was 8 ± 3% larger than the geometric image area (RF_{avg} = 1.09) for the film prior to any treatment. This value decreased slightly after anodic polarization to a value of 4 ± 3% (RF_{avg} = 1.05), presumably due to etching of some sp^2-bonded

carbon in the grain boundaries. The RMS roughness did not change significantly after anodic polarization as the value was 20 ± 6 before and 18 ± 6 nm after anodic polarization.

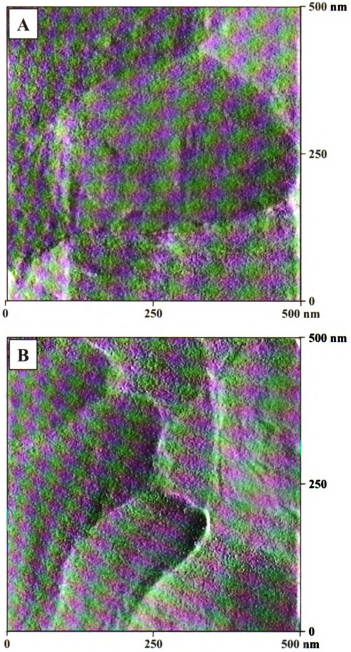

Figure 4.8. Atomic force micrographs (500 x 500 nm) of boron-doped nanocrystalline diamond thin film (A) before and (B) after anodic polarization.

Table 4.7. Comparison of the Real and Geometric Areas for Boron-Doped Nanocrystalline Diamond Films Before and After Anodic Polarization

Projected Surface Area (μm^2)	Initially		Anodically Polarized	
	Real SA (μm^2)	Roughness Factor[a]	Real SA (μm^2)	Roughness Factor[a]
0.25	0.28 ± 0.01	1.12	0.274 ± 0.001	1.10
4	4.3 ± 0.1	1.08	4.13 ± 0.01	1.03
25	26.5 ± 0.7	1.06	25.6 ± 0.1	1.02
RF_{avg}	–	**1.09**	–	**1.05**

[a] Roughness Factor (RF) = Real SA/Geometric SA

The microstructure of nanocrystalline diamond was investigated using Raman spectroscopy. The Raman spectra for nanocrystalline diamond films grown from argon-rich (Ar-rich) source gas mixtures are often characterized by broad peaks at ~1150, 1332, 1350, ~1480, and 1550 cm^{-1}.[13,32,33] Nanocrystalline diamond, grown from Ar-rich mixtures, consists of small clusters of sp^3-bonded diamond grains connected through sp^2 hybridized carbon bonds in the grain boundaries.[13,34,35] As with microcrystalline diamond, the peak at 1332 cm^{-1}, partially obscured by a large background scattering signal, is associated with the first-order phonon mode of sp^3-bonded diamond. The peak width (FWHM) for the diamond line is larger in nanocrystalline than in microcrystalline diamond (140 vs. 10 cm^{-1}) for two possible reasons. First, is the confinement model which states that the smaller the crystal size is, the larger the number of phonon modes (with different q vectors and energies) that can participate in the Raman process.[36] The larger number of modes of slightly different energy leads to the increased line width.

Second, is the phonon scattering by impurities and defects (*i.e.*, grain boundaries) which shortens the phonon lifetime and results in an increased line width.

The peak at 1150 cm^{-1} has often been used as an indicator for high-quality nanocrystalline diamond grown from Ar-rich mixtures.[37,38] However, Ferrari and Robertson have argued against this suggesting that the peak is attributable to sp^2-bonded carbon, specifically trans-polyacetylene segments at grain boundaries.[32,33 and refs. therein] This is based on their observations that (*i*) the peak position changes and the intensity decreases with decreasing excitation wavelength, something that is not possible for a density-of-states feature which should remain invariant, and (*ii*) the peak is always accompanied by the 1480 cm^{-1} peak, which behaves in a similar fashion. The former is due to increasing cross sectional scattering coefficient for diamond at the shorter excitation wavelengths (decreasing cross section for nondiamond sp^2 carbon). This has recently been confirmed by Birrel *et al.* who found a transition from nanocrystalline to microcrystalline morphology with increasing H_2 content (0 – 20%) in a $CH_4/Ar/H_2$ source gas mixture.[39] Thus, it was confirmed that despite consisting of mostly sp^3-bonded carbon (~95%), the Raman signal was due entirely to the sp^2-bonded carbon in the grain boundary.[39] Additionally, the peaks at 1120 and 1480 cm^{-1} were loosely attributed to C-H bonds in the grain boundaries, while the peaks at 1350 and 1560 cm^{-1} were attributed to the D- and G-bands, respectively, that are routinely observed for disordered sp^2-bonded carbon.[39]

Figure 4.9 shows representative Raman spectra for a nanocrystalline diamond film before and after anodic polarization. Each frequency of interest is denoted by a dotted line. The first-order diamond peak at 1332 cm^{-1}, as well as the D and G band peaks, remained unchanged in terms of peak position, intensity and width after the polarization. These trends are consistent with an unchanging microstructure. The Raman peaks at 1150 and 1480 cm^{-1} are represented by ν_1 and ν_3, respectively. These peaks become slightly less pronounced after polarization. This likely indicates a decrease in the amount of hydrogenated sp^2 carbon (*e.g.*, C–C–H) and possibly H atoms within the grain boundaries. Ferrari *et al.* have shown that the ν_1 and ν_3 modes of trans-polyacetylene are connected to the presence of hydrogen. Post-deposition annealing as well as growth of the films using deuterated and hydrogenated plasmas resulted in either a significant shift in the peak position or the complete loss of the peaks, depending on the experiment.[33 and refs. therein]

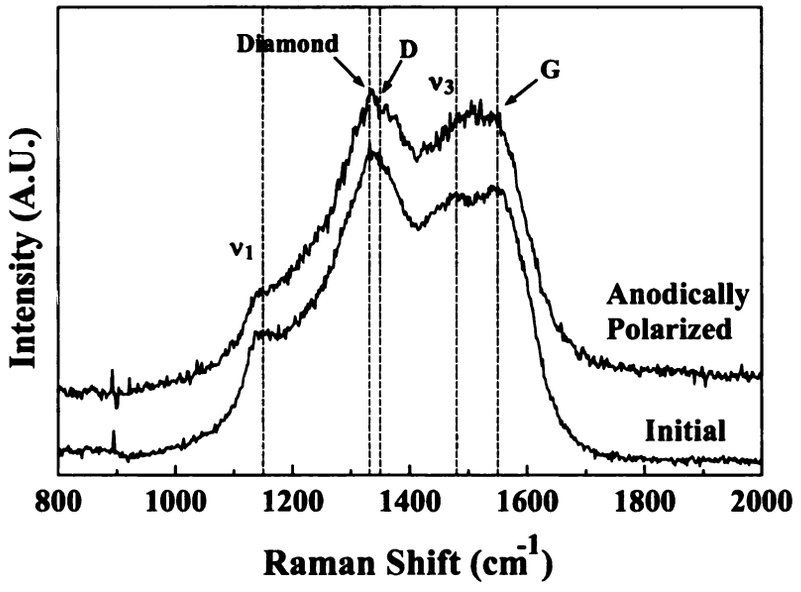

Figure 4.9. Raman spectra for a boron-doped nanocrystalline diamond film before and after anodic polarization. Spectra are off-set for viewing clarity.

4.3.2 Surface Chemistry

The surface chemistry, as assessed from the relative hydrophobicity/hydrophilicity, of the nanocrystalline diamond thin film was also evaluated before, after anodic polarization and after rehydrogenation. Again a 10 μL drop of ultrapure water was used in contact angle measurements. The measured instantaneous contact angles are summarized in Table 4.8. Initially, the nanocrystalline diamond film exhibited a contact angle of 82 ± 4°. This was slightly higher than the value initially obtained for the microcrystalline diamond surface and is likely due to the reduced surface roughness of the film. The contact angle decreased considerably after the anodic polarization to a value of 43 ± 6° consistent with increased surface oxygen content. The contact angle then increased for the rehydrogenated film to 64 ± 4°, but not quite to the original level.

Table 4.8. Summary of Contact Angle Measurements for Ultrapure Water on Boron-Doped Nanocrystalline Diamond Thin Film as a Function of the Surface Chemistry

Diamond Condition	Initially	Anodically Polarized	Rehydrogenated
Contact Angle	82 ± 4°	43 ± 6°	64 ± 4°
Percent Change	–	-48%	+49%

4.3.3 Electrochemical Response

The cyclic voltammetric background *i-E* curves for a film before, after anodic polarization and after rehydrogenation was measured in N_2 purged 0.1 M $HClO_4$. Typical curves, over a narrow potential range, are shown in Figure 4.10. The measured potential window (±50 μA or ± 250 μA/cm^2) and background current magnitude at 400

mV are displayed in Table 4.9. The voltammetric *i-E* curve for the film before any treatment was flat and featureless between the regions of gas evolution indicating a clean diamond surface void of any electroactive carbon. The nanocrystalline films exhibited an average potential window and background current of 3.0 ± 0.2 V and 1.7 ± 0.1 μA, respectively. After anodic polarization, the potential window decreased to 2.1 ± 0.2 V and the background current increased to 41 ± 16 μA. The voltammetric *i-E* curve is still flat suggesting the surface was largely void of electroactive surface functional groups. This change in potential window and background current is considerably greater than that observed for the microcrystalline diamond. These quantities did not recover with rehydrogenation as a potential window and background current were 2.2 ± 0.2 V and 39 ± 14 μA, respectively.

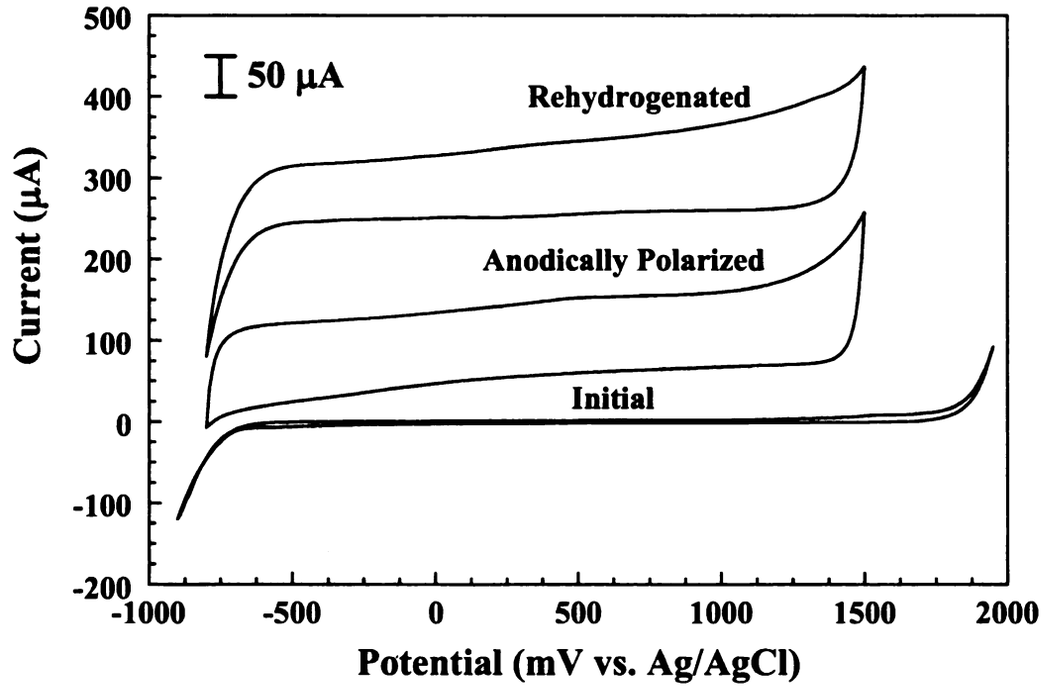

Figure 4.10. Background cyclic voltammetric *i-E* curves in degassed 0.1 M $HClO_4$ for boron-doped nanocrystalline diamond films as a function of the surface condition. Scan Rate = 100 mV/s.

Table 4.9. Potential Window and Background Current Measured from Cyclic Voltammetric *i-E* Curves for a Boron-Doped Nanocrystalline Diamond Thin Film in 0.1 M $HClO_4$ at a Scan Rate of 100 mV/s.

Diamond Condition	Potential Window (V)[a]	Background Current (μA)
Initially	3.0 ± 0.2	1.7 ± 0.1
Anodically Polarized	2.1 ± 0.2	41 ± 16
Rehydrogenated	2.2 ± 0.2	39 ± 14

[a] Potential window is defined as ±50 μA or ±250 μA/cm^2

The electrochemical response of the film towards $Fe(CN)_6^{3-/4-}$, $Ru(NH_3)_6^{3+/2+}$ and $Fe^{3+/2+}$ was recorded before and after the treatments. Typical voltammetric *i-E* curves for each of these analytes are presented in Figure 4.11A-C. The ΔE_p value for each at various scan rates is displayed in Tables 4.10, 4.11 and 4.12.

The ΔE_p for $Fe(CN)_6^{3-/4-}$ at the nanocrystalline film was initially 69 mV (100 mV/s), as shown in Table 4.10. After anodic polarization, ΔE_p increased to 120 mV consistent with an increase in surface oxygen content. Also note the increase in background current in the voltammetric *i-E* curve in Figure 4.11A. After rehydrogenation, ΔE_p returned to near the original value of 65 mV. The voltammetric *i-E* curve though still exhibits the large background current. The oxidation peak current varied linearly with the scan rate$^{1/2}$ ($r^2 > 0.999$) indicating the rate of the redox reaction is limited by diffusional mass transport to the surface.

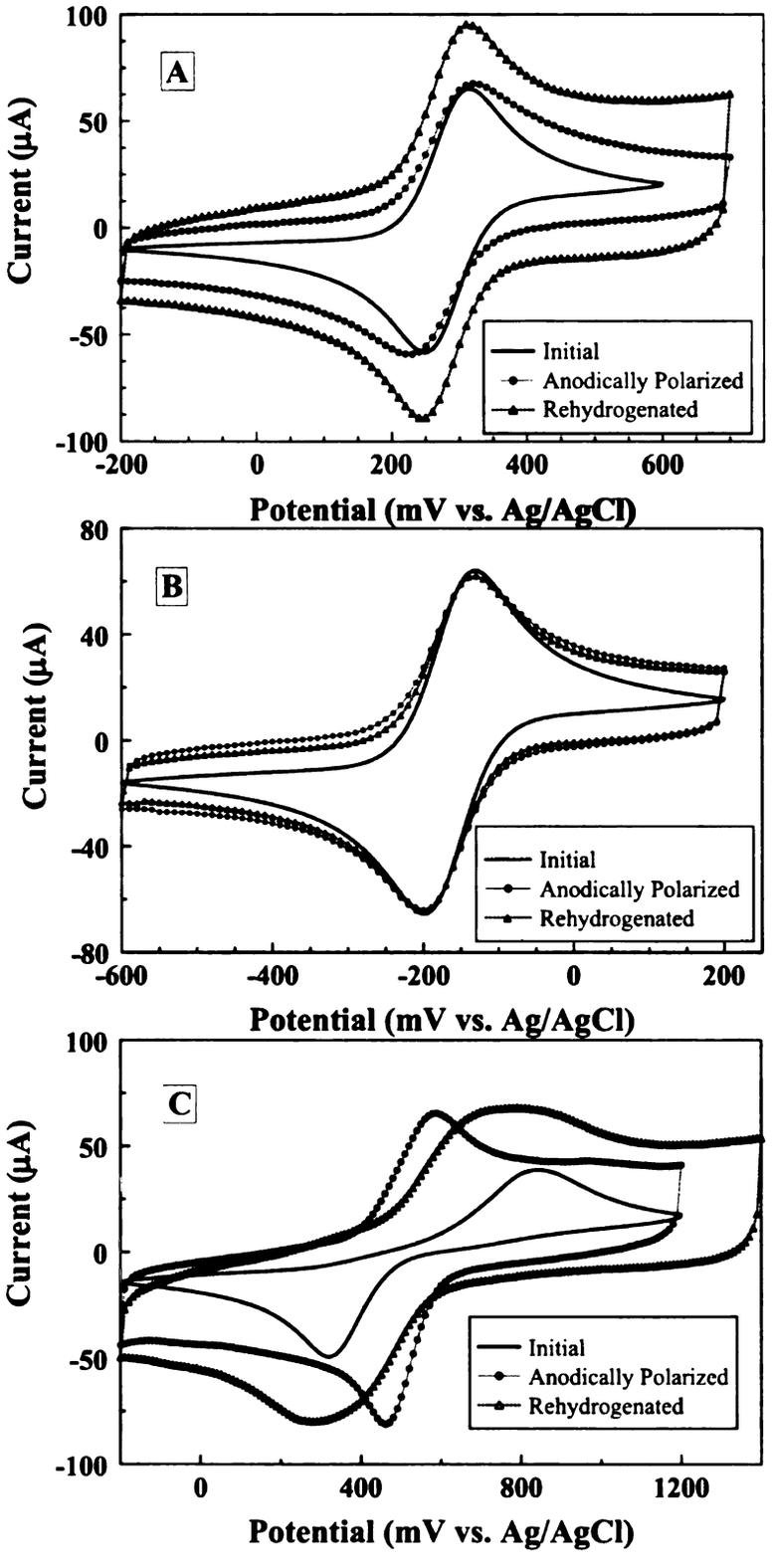

Figure 4.11. Cyclic voltammetric *i-E* curves for boron-doped nanocrystalline diamond films before, after anodic polarization and after rehydrogenation in the presence of (A) $Fe(CN)_6^{3-/4-}$, (B) $Ru(NH_3)_6^{3+/2+}$ and (C) $Fe^{3+/2+}$. Scan Rate = 100 mV/s.

Table 4.10. Cyclic Voltammetric Peak Potential Separation (ΔE_p) for 1 mM $Fe(CN)_6^{3-/4-}$ in 1 M KCl at Boron-Doped Nanocrystalline Diamond as a Function of the Surface State

Scan Rate	ΔE_p for $Fe(CN)_6^{3-/4}$ (mV)		
	Initially	Anodically Polarized	Rehydrogenated
50	66 ± 2	100 ± 30	65 ± 0
100	69 ± 2	120 ± 40	65 ± 2
300	74 ± 6	160 ± 70	78 ± 4
500	82 ± 5	180 ± 70	85 ± 2

The ΔE_p for $Ru(NH_3)_6^{3+/2+}$, which is known to be relatively insensitive to the surface chemistry of diamond, remained relatively unchanged throughout the course of the experiments. ΔE_p values of 64-82, 69-93, and 66-85 mV were observed at scan rates of 50-500 mV/s before, after anodic polarization and after rehydrogenation, respectively, as seen in Table 4.11. This indicates that despite the increase in capacitance, the electrical conductivity and activity of the film remained unaltered. As with the $Fe(CN)_6^{3-/4-}$ couple, the i_p^{ox}/i_p^{red} ratio remained approximately unity and each scaled linearly with $\nu^{1/2}$, indicating that the increased capacitance did not alter the reversibility of the reaction.

Table 4.11. Cyclic Voltammetric Peak Potential Separation (ΔE_p) for 1 mM $Ru(NH_3)_6^{3+/2+}$ in 1 M KCl at Boron-Doped Nanocrystalline Diamond as a Function of the Surface State

Scan Rate	ΔE_p for $Ru(NH_3)_6^{3+/2+}$ (mV)		
	Initially	Anodically Polarized	Rehydrogenated
50	64 ± 2	69 ± 2	66 ± 2
100	67 ± 1	67 ± 4	67 ± 3
300	74 ± 4	83 ± 8	75 ± 3
500	82 ± 5	93 ± 6	85 ± 2

The ΔE_p for $Fe^{3+/2+}$ exhibited a wide variation throughout the course of this work as shown in Table 4.12. The ΔE_p ranged from 480-660 mV before any treatment, consistent with an oxygen-free surface. As expected, this value decreased to 129-165 mV after anodic polarization. The relatively low ΔE_p indicates that surface carbon-oxygen functional groups were introduced, particularly carbonyl groups. After rehydrogenation, ΔE_p increased to a high value of 390-640 mV. Similar to the microcrystalline diamond, the i_p^{ox}/i_p^{red} ratio for this redox system was less than unity (*ca.* 0.7-0.8) as expected due to the electrochemical irreversibility. Interestingly, the increase in film capacitance did not influence the electrochemical response towards any of the redox analytes.

Table 4.12. Cyclic Voltammetric Peak Potential Separation (ΔE_p) for 1 mM $Fe^{3+/2+}$ in 0.1 M $HClO_4$ at Boron-Doped Nanocrystalline Diamond as a the Function of Surface State

Scan Rate	ΔE_p for $Fe^{3+/2+}$ (mV)		
	Initially	**Anodically Polarized**	**Rehydrogenated**
50	480 ± 50	130 ± 30	390 ± 130
100	530 ± 50	130 ± 30	470 ± 130
300	620 ± 50	170 ± 50	570 ± 110
500	660 ± 50	165 ± 9	640 ± 120

The nanocrystalline diamond could also serve as a dimensionally stable electrocatalyst support. However, the irreversible increase in background current is a concern. There is a least some minor damage to the nanocrystalline diamond film that is not detected in the microscopy. One thing worth noting is that when the nanocrystalline diamond was removed from the cell, the current collecting Cu plate had turned purple

where the film had been. Additionally, the Viton™ o-ring was stuck to the nanocrystalline diamond surface and had to be peeled off, leaving a noticeable ring of possible residue on the surface. This residue could not be removed with cleaning and rehydrogenating. In fact after rehydrogenation, the nanocrystalline film still possessed a dark spot where the film was exposed to the solution. None of this reactivity was seen with the microcrystalline film. It is almost as if the nanocrystalline film (due to resistance) got hotter during the anodic polarization than the microcrystalline diamond. Perhaps the Viton™ residue causes the increase in background current when that portion of the film is exposed to the electrolyte solution when remounted in the electrochemical cell. A possible source of increased capacitance is degradation of the carbon within the grain boundaries making the underlying Si substrate susceptible to solution. If this occurred during the anodic polarization, the Si would have been etched; a reaction which is exothermic.[40-43] Perhaps this released heat caused both the discoloration of the Cu plate and melting of the o-ring. Additionally, exposure of the electrolyte solution to the Si substrate would increase the observed capacitance in the *i-E* curves.

4.3.4 Electrical Conductivity Maps

Conductivity probe-atomic force microscopy (CP-AFM) was used to simultaneously map the film topography and electrical conductivity. Figure 4.12 presents AFM height mode images over a 1 x 1 μm area as well as conductivity maps of the same area for a boron-doped nanocrystalline diamond film after the completed experiment (*i.e.*, after both polarization and rehydrogenation) and compared to a H-terminated nanocrystalline diamond film which was previously presented.[15] Though these are not of

the same area, there is a greater distance between areas of higher conductivity for the polarized film compared to a normal nanocrystalline diamond film. The anodically polarized film shows very distinct "hot spots" of high conductivity and regions of almost complete insulation. It is possible that the electrically conducting regions are redistributed during the anodic polarization resulting in the increase in electrode capacitance. It is also possible that the removal of trans-polyacetylene (*i.e.*, H atoms) from the grain boundaries explains the change in the conductivity maps.

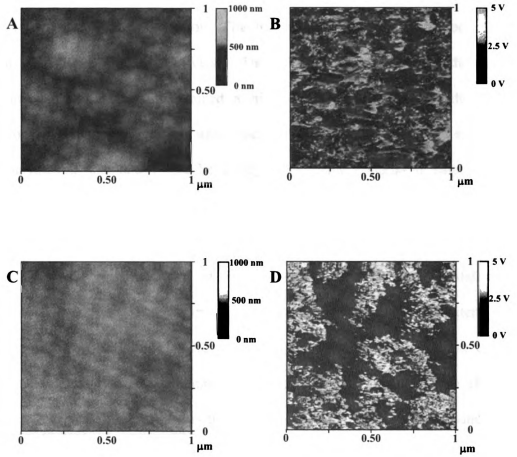

Figure 4.12. AFM height mode images (air) (A and C) and simultaneously recorded conductivity maps (bias voltage, $E_{tip} - E_{substrate} = +2$ V) of the same regions (B and D) of a boron-doped nanocrystalline diamond thin film over a 1 x 1 μm area not polarized (A and B) and anodically polarized (C and D).

4.4 Conclusions

Boron-doped microcrystalline and nanocrystalline diamond thin-film electrodes were evaluated as possible electrocatalyst support materials by assessing their stability under conditions commonly encountered in PAFCs. The microcrystalline diamond exhibited some surface oxidation resulting in slight roughening of the crystallite edges. Neither atomic force nor scanning electron microscopic images revealed signs of gross morphological degradation (*e.g.*, pitting or debonding). Additionally, any changes in the electrochemical properties brought about by the oxidative condition of the polarization were reversed after rehydrogenation. This is consistent with the changes being brought about by surface chemistry effects. The microcrystalline form of diamond was dimensionally stable and maintained a high degree of electrical conductivity and electrochemical responsiveness after the polarization. Indeed it appears that microcrystalline diamond would be a physically stable material if employed as an electrocatalyst support.

The nanocrystalline form of diamond also appears to be a candidate as an electrocatalyst support. The nanocrystalline film was altered to a greater extent than the microcrystalline film during anodic polarization as evidenced by the larger change in contact angle, increased background voltammetric current, and response change for $Fe(CN)_6^{3-/4-}$ and $Fe^{3+/2+}$. It appears that solution can penetrate the grain boundaries and react with the underlying Si during the polarization. The diamond is stable but the grain boundary carbon is not. However, the response towards $Fe(CN)_6^{3-/4-}$ and $Fe^{3+/2+}$ returned to the original values upon rehydrogenation indicating that alterations in the

nanocrystalline diamond surface chemistry are reversible. Microscopically, no gross morphological degradation was seen but some changes occurred that were irreversible. The electrical conductivity of the material was unchanged after polarization and rehydrogenation. All of this leads to the conclusion that the nanocrystalline form of diamond might function as a stable electrocatalyst support material.

REFERENCES

1. E. Antolini, *J. Mater. Sci.*, **38**, 2995 (2003).

2. F. Rodríguez-Reinoso, *Carbon*, **36**, 159 (1998).

3. E. Auer, A. Freund, J. Pietsch, and T. Tacke, *Appl. Catal. A: Gen.*, **173**, 259 (1998).

4. M. W. Reed and R. J. Brodd, *Carbon*, **3**, 241 (1965).

5. B. C. H. Steele and A. Heinzel, *Nature*, **414**, 345 (2001).

6. J. Wang, G. M. Swain, T. Tachibana, and K. Kobashi, *Electrochem. Solid-State Lett.*, **3**, 286 (2000).

7. J. Wang, G. M. Swain, T. Tachibana, and K. Kobashi, *J. New Mater. Electrochem. Sys.* , **3**, 75 (2000).

8. J. Wang and G. M. Swain, *Electrochem. Solid-State Lett.*, **5**, E4 (2002).

9. J. Wang and G. M. Swain, *J. Electrochem. Soc.*, **150**, E24 (2003).

10. A. E. Fischer and G. M. Swain, *J. Electrochem. Soc.*, **152**, B369 (2005).

11. M. Witek, J. Wang, J. Stotter, M. Hupert, S. Haymond, P. Sonthalia, G. M. Swain, J. K. Zak, Q. Chen, D. M. Gruen, J. E. Butler, K. Kobashi, and T. Tachibana, *J. Wide Bandgap Mater.*, **8**, 171 (2002).

12. J. Wang, G. M. Swain, M. Mermoux, G. Lucazeau, J. Zak, and J. W. Strojek, *New Diamond Front. Carbon Technol.*, **9**, 317 (1999).

13. Y. Show, M. A. Witek, P. Sonthalia, and G. M. Swain, *Chem. Mater.*, **15**, 879 (2003).

14. M. C. Granger, M. Witek, J. Xu, J. Wang, M. Hupert, A. Hanks, M. D. Koppang, J. E. Butler, G. Lucazeau, M. Mermoux, J. W. Strojek, and G. M. Swain, *Anal. Chem.*, **72**, 3793 (2000).

15. J. A. Bennett, Y. Show, S. Wang, and G. M. Swain, *J. Electrochem. Soc.*, **152**, E184 (2005).

16. J. A. Bennett and G. M. Swain, *Manuscript in preparation.*

17. P. Sonthalia, E. McGaw, Y. Show, and G. M. Swain, *Anal. Chim. Acta*, **522**, 35 (2004).

18. E. A. McGaw and G. M. Swain, *Anal. Chim. Acta*, **575**, 180 (2006).

19. A. E. Fischer, Ph. D. Dissertation, *Degradation Mechanisms of Carbon-Based Electrocatalyst Support Materials and Development of an Advanced Support Based on Electrically Conducting Diamond*, Michigan State University, East Lansing, MI, (2005).

20. W. L. Wang, M. C. Polo, G. Sánchez, J. Cifre, and J. Esteve, *J. Appl. Phys.*, **80**, 1846 (1996).

21. K. Ushizawa, K. Watanabe, T. Ando, I. Sakagucki, M. Nishitani-Gamo, Y. Sato, and H. Kanada, *Diamond and Rel. Mater.*, **7**, 1719 (1998).

22. P. Gonon, E. Gheeraert, A. Deneuville, F. Fontaine, L. Abello, and G. Lucazeau, *J. Appl. Phys.*, **78**, 7059 (1995).

23. M. C. Granger, J. Xu, J. W. Strojek, and G. M. Swain, *Anal. Chim. Acta*, **397**, 145 (1999).

24. M. Mermoux, B. Marcus, G. M. Swain, and J. E. Butler, *J. Phys. Chem. B*, **106**, 10816 (2002).

25. L. Ostrovskaya, V. Perevertailo, V. Ralchenko, A. Dementjev, and O. Loginova, *Diamond and Rel. Mater.*, **11**, 845 (2002).

26. F. Pinzari, P. Ascarelli, E. Cappelli, G. Mattei, and R. Giorgi, *Diamond and Rel. Mater.*, **10**, 781 (2001).

27. J. A. Bennett, J. Wang, Y. Show, and G. M. Swain, *J. Electrochem. Soc.*, **151**, E306 (2004).

28. M. C. Granger and G. M. Swain, *J. Electrochem. Soc.*, **146**, 4551 (1999).

29. Y. Bu and C. Deng, *J. Phys. Chem. A*, **101**, 1198 (1997).

30. B. S. Brunschwig, J. Logan, M. D. Newton, and N. Sutin, *J. Am. Chem. Soc.*, **102**, 5798 (1980).

31. C. A. McDermott, K. R. Kneten, and R. L. McCreery, *J. Electrochem. Soc.*, **140**, 2593 (1993).

32. A. C. Ferrari and J. Robertson, *Phys. Rev. B*, **63**, 121405 (2001).

33. A. C. Ferrari and J. Robertson, *Philos. Trans. R. Soc. London, A*, **362**, 2477 (2004).

34. D. M. Gruen, *MRS Bull.*, **23**, 32 (1998).

35. Q. Chen, D. M. Gruen, A. R. Krauss, T. D. Corrigan, M. Witek, and G. M. Swain, *J. Electrochem. Soc.*, **148**, E44 (2001).

36. L. Bergman and R. J. Nemanich, *J. Appl. Phys.*, **78**, 6709 (1995).

37. R. E. Shroder, R. J. Nemanich, and J. T. Glass, *Phys. Rev. B*, **41**, 3738 (1990).

38. S. Prawer, K. W. Nugent, D. N. Jamieson, J. O. Orwa, L. A. Bursill, and J. L. Peng, *Chem. Phys. Lett.*, **332**, 93 (2000).

39. J. Birrell, J. E. Gerbi, O. Auciello, J. M. Gibson, J. Johnson, and J. A. Carlisle, *Diamond and Rel. Mater.*, **14**, 86 (2005).

40. G. G. Budaguan, A. A. Aivazov, and A. Y. Sazonov, *Calorimetric Investigation of Relaxation Processes in Disordered Semiconductors*, **420 (Amorphous Silicon Technology--1996)**, p. 635, *Materials Research Society Symposium Proceedings*, Materials Research society, (1996).

41. T. Hoshino and Y. Nishioka, *Etching Process of Al Oxide on Si Surface with HF Treatment*, **492(Microscopic Simulation of Interfacial Phenomena in Solids and Liquids)**, p. 201, *Materials Research Society Symposium Proceedings*, Materials Research Society, (1998).

42. C. W. Lo, P. R. Varekamp, D. K. Shuh, T. D. Durbin, V. Chakarian, and J. A. Yarmoff, *Surf. Sci.*, **292**, 171 (1993).

43. C. J. Wu and E. A. Carter, *J. Am. Chem. Soc.*, **113**, 9061 (1991).

CHAPTER 5

Pulsed Galvanostatic Deposition of Pt Particles on Microcrystalline and Nanocrystalline Diamond Thin-Film Electrodes

5.1 Introduction

Carbon-supported metal catalysts are widely used in electrochemical technologies. For example, dispersed Pt particles on high-surface-area carbon supports are used as catalysts for hydrogenation and oxidation reactions, such as for both hydrogen oxidation and oxygen reduction in phosphoric acid (PAFCs) and proton exchange membrane fuel cells (PEMFCs).[1,2] Platinum is the best electrocatalyst for the oxygen reduction reaction (ORR); an important reaction in both biological systems and fuel cells.[3-13] Among the carbon support materials regularly employed, activated carbons are the most common. Activated carbons possess a turbostratic microstructure of sp^2-bonded carbon with a high surface area and microporosity.[1,2] The properties of the electrocatalyst support material are crucial for the operational performance.[1-3,14,15] The primary role of the support is to provide a high surface area over which highly dispersed, nanometer-sized electrocatalyst particles can be dispersed and stabilized, and electrical connection to these particles can be made. Highly dispersed supported catalysts are attractive for electrochemical processes because a high electrochemically active surface area can be achieved with a low loading of the normally expensive electrocatalyst.

As mentioned previously, current electrocatalyst support materials are generally porous, sp^2-bonded carbon materials (*e.g.*, physically or chemically activated carbon or carbon black). These materials function well in many applications but are susceptible to oxidation and/or corrosion in the presence of reactive oxygen, in aggressive chemical environments and/or under harsh electrochemical conditions.[1,2,15,16] If the degradation is severe enough, complete electrode failure can result. However, even minimal oxidation/corrosion causes morphological and microstructural damage that leads to decreased catalytic activity due to catalyst detachment, aggregation and/or fouling by gasification products.

Advanced electrocatalyst support materials are needed for those demanding applications where conventional sp^2-bonded carbon supports degrade. One example of this is in fuel cells during start-up and shut-down as a local cathode potential as high as 1.2-1.5 V can be reached, which is a potential well positive of the thermodynamic value for carbon corrosion.[17] The rate of carbon corrosion increases considerably at such high voltages and cumulatively this leads to degradation of the stack voltage. Our group has been investigating the possibility of using electrically conducting diamond as an advanced carbon electrocatalyst support material.[18-21] There are two technical challenges to be overcome in this effort: development of an electrically conducting, high surface area form of diamond (*e.g.*, powder)[22,23] and establishment of a protocol for depositing and stabilizing highly dispersed electrocatalyst particles on the diamond surface. Thus far, our efforts have been focused on the latter task with the goals of (*i*) determining the dimensional stability of diamond thin film (low surface area) under a variety of

electrochemical conditions with[19] and without (see Chapter 4) deposited metal particles and (*ii*) studying the formation of electrocatalytic Pt adlayers on the film surface.[20] Diamond possesses properties that make it an attractive support material: dimensional stability, resistance to corrosion and the ability to operate for extended periods of time in harsh chemical environments at high potential, current density, and temperature without microstructural or morphological degradation.[21,24]

Two types of electrically conducting diamond thin film are under investigation: microcrystalline (>1 μm crystallite size) and nanocrystalline (~10-20 nm crystallite size).[25-30] Each possesses a different morphology and microstructure, but both exhibit similar electrical conductivity and electrochemical activity when highly doped with boron. The formation of metal phases on polycrystalline diamond has been reported.[20,31-35] A common observation, though, is weak attachment of the metal particles to the hydrogen-terminated diamond surface.[19,20,33,34] Consequently, the metal particles are easily dislodged from the surface by gas evolution, for instance. In an effort to better stabilize the metal particles, we have adopted an approach whereby a short secondary diamond growth is applied to the metal-coated surface. This secondary growth physically entraps the metal particles into the surface microstructure without causing major loss in the electrocatalytic activity. We refer to this material as a metal/diamond composite electrode.[19-21] This sequential diamond growth/Pt deposition/secondary diamond growth procedure produces a dimensionally stable and electrically conductive catalytic electrode. The metal catalyst particles are strongly anchored in the microstructure by the secondary diamond growth. For instance, no morphological or

microstructural damage and no lost catalyst activity were observed after two 1-h periods of anodic polarization in 85% H_3PO_4 at 170 °C and 0.1 A/cm^2.[19] In comparison, a Pt-impregnated sp^2 carbon cloth electrode (E-Tek) failed catastrophically within the first few minutes of exposure to the same conditions.

We have previously studied the formation of Pt adlayers on diamond by dc magnetron sputtering[18] and electrodeposition, using both constant potential and current deposition.[19,20] Electrodeposition is the preferred method of the two because it affords better control over the particle size and coverage. Despite the excellent dimensional stability of the Pt/diamond composite electrode, the nominal Pt particle size produced was too large and the coverage too low to be practical. For example, the particle size varied from 50 to 300 nm and the particle coverage was in the 10^8 cm^{-2} range for metal phase formation at constant current.[19,20] Low loadings of highly dispersed metal particles are desired for a practical supported catalyst. Pulsed galvanostatic deposition can produce metal particles that are nominally smaller in size and more uniformly distributed over a surface compared to what is achieved using constant current deposition. Pulsed electrodeposition approaches have been employed to prepare nanometer-sized particles of metals and alloys.[35-47] Individual particle growth is favored as the conditions are selected to minimize overlap of reactant depletion layers from neighboring particles on the surface. Maintaining separate depletion layers around each particle results in similar growth rates for all and leads to more highly dispersed particles of nominally smaller size.

We report herein on the use of pulsed galvanostatic deposition to form Pt adlayers on both microcrystalline (BMD) and nanocrystalline (BND) diamond thin films. This work was a continuation of our effort to control and understand metal phase formation on diamond. The purpose for the work was to learn how the nucleation and growth of Pt electrocatalyst particles on both diamond types is affected by the pulse current density and pulse number. In particular, the spatial distribution of the deposits over the surface, the nominal particle size and variance, and the particle coverage were all factors of interest. Another objective was to learn how the diamond film morphology and microstructure affect the metal phase formation. Polycrystalline diamond is a heterogeneous electrode material in terms of its microstructural and electronic properties, which complicates the study of metal phase formation. The microstructural and electronic properties certainly play a key role in the kinetics of metal electrodeposition and the time-dependent surface morphology of the deposits. The uncoated and coated diamond electrodes were characterized by scanning electron microscopy (SEM), cyclic voltammetry, and conductivity-probe atomic force microscopy (CP-AFM).

5.2 Results

5.2.1 Pt Deposition on Microcrystalline Diamond

Pt metal was deposited onto the diamond surface by pulsed galvanostatic deposition with the pulse width and current density maintained constant for 1 s at 0.50 mA/cm^2 (geometric area), and a pulse number of 10, 25 or 50. This current was selected as a starting point based upon previous work in the group .[20] Figure 5.1A-C shows secondary electron micrograph (SEM) images of Pt-coated microcrystalline diamond

thin-film electrodes for these three pulse numbers. EDX analysis confirmed that the bright spots were indeed Pt. The particles decorate both the grains and grain boundaries, indicating that most regions of the polycrystalline film are electrochemically active and support charge transfer. This is somewhat in contrast to observations made recently using CP-AFM and SECM.[48] The formation of the multilayer islands or particles is consistent with a Volmer-Weber mechanism of deposition, which incorporates the postulate that deposition of metal on preexisting metal centers is more favorable than metal deposition on a foreign substrate that exhibits a low surface free energy.[36,41] Increasing the number of pulses lead to an increase in the metal loading as more overall deposition charge was passed; however, the nominal particle size increased and the particle coverage decreased. These trends are evident in the Table 5.1 data. Depositing Pt with 10 pulses yielded a nominal particle diameter of 50 ± 30 nm [relative standard deviation (RSD) = 60%] and a nominal particle coverage of 1.1 (± 0.6) x 10^9 cm^{-2}. Increasing the number of pulses to 25 approximately doubled the average particle diameter to 100 ± 90 nm (RSD = 90%) and reduced the particle coverage to 1.0 (± 0.4) x 10^9 cm^{-2}. Increasing the number of pulses to 50 slightly increased the average particle diameter to 110 ± 70 nm (RSD = 64%) and significantly reduced the particle coverage to 0.38 (± 0.01) x 10^9 cm^{-2}. Careful examination of the images, in particular Fig. 5.1C, reveals that the particles are not smooth but rather are rough with a dendritic morphology.

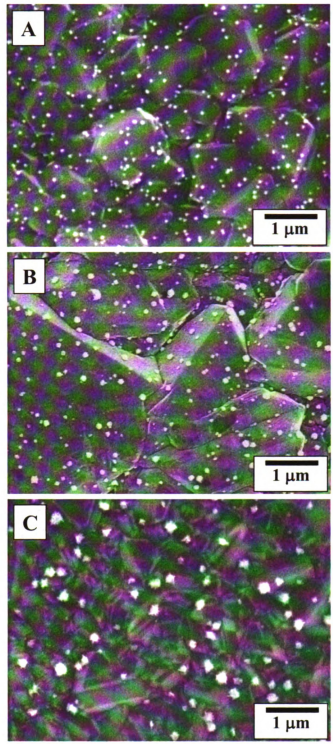

Figure 5.1. Scanning electron micrographs of microcrystalline diamond electrodes covered with Pt particles that were deposited using (A) 10, (B) 25 and (C) 50 pulses, respectively. Pulse width = 1 s. Current density = 0.50 mA/cm^2.

Figure 5.2 shows background cyclic voltammetric *i-E* curves in 0.1 M $HClO_4$ for the Pt-coated microcrystalline thin-film electrodes formed with different pulse numbers. The scans were initiated at 200 mV with the forward sweep in the positive direction at a rate of 50 mV/s. All the voltammetric features characteristic of clean polycrystalline Pt was observed. The total current response increased with pulse number, which is consistent with an increase in the Pt loading; more specifically an increase in the electrochemically active Pt. Even though the nominal particle diameter increased and the coverage decreased, the electrochemically active Pt increased because of a highly rough, dendritic particle morphology, as is evident in Figure 5.1C.[49]

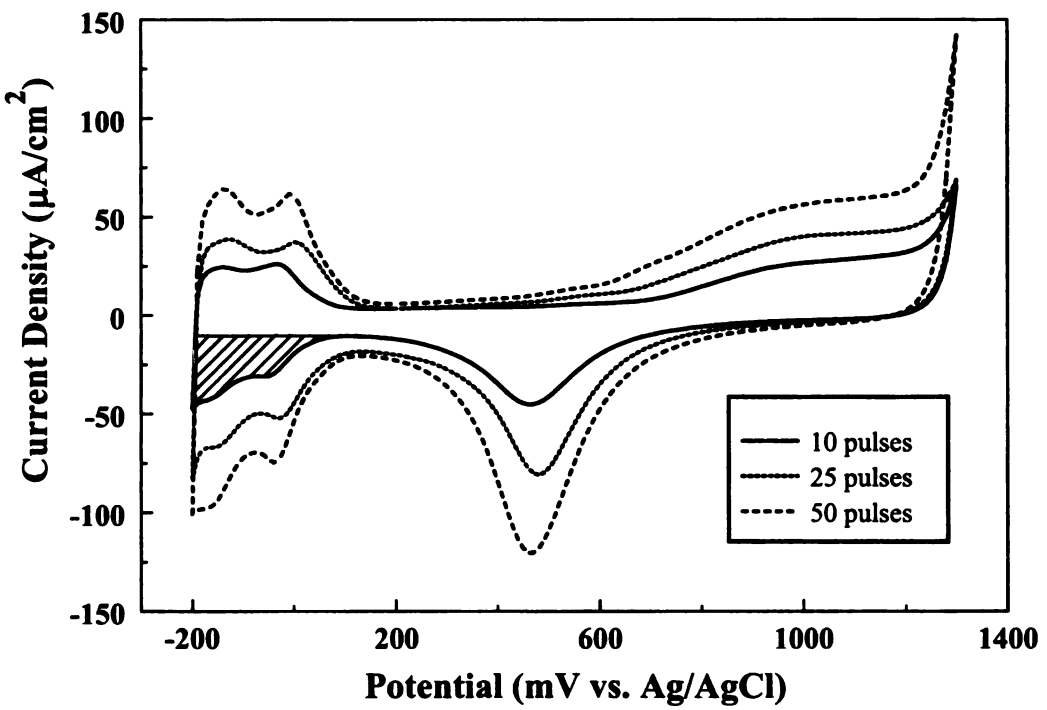

Figure 5.2. Cyclic voltammetric *i-E* curves in degassed 0.1 M $HClO_4$ for microcrystalline electrodes coated with Pt using different pulse numbers. Pulse width = 1 s. Current density = 0.50 mA/cm^2. Scan rate = 50 mV/s. The shaded region of the curve represents the charge associated with hydrogen adsorption. The current is normalized to the diamond geometric area, 0.2 cm^2.

Table 5.1. Particle Analysis and Hydrogen Adsorption Data for Pt-Coated Microcrystalline Diamond Films as a Function of the Pulse Number[a]

No. of Pulses	Mean Particle Size (nm)	Particle Coverage (10^9 cm^{-2})[b]	Hydrogen Adsorption Charge (mC/cm^2)[b]
10	50 ± 30	1.1 ± 0.6	0.07 ± 0.01
25	100 ± 90	1.0 ± 0.4	0.13 ± 0.01
50	110 ± 70	0.38 ± 0.01	0.21 ± 0.02

[a] Pulse width = 1 s. Delay time = 1 s. Current density = 0.50 mA/cm^2 (geometric area).
[b] Values normalized to the geometric area of the diamond film (0.2 cm^2)

The well-defined voltammetric signatures for Pt indicate that the metal particles are in good electrical communication with the current-collecting p-Si substrate through the boron-doped diamond film. The H^+ adsorption charge density, listed in Table 5.1, was found by integrating the cathodic current for this reaction between 100 and -190 mV vs. Ag/AgCl and correcting for the double-layer charging current (see the shaded region of the *i-E* curve in Figure 5.2). The electrochemically active Pt surface area (ESA), displayed in Table 5.2, was calculated to be 0.06, 0.13 and 0.20 cm^2_{Pt}, respectively for 10, 25 and 50 pulses. All electrodes possessed the same deviation of ± 0.02 cm^2_{Pt}. Consequently, the roughness factor [RF, the electrochemically active Pt area/geometric area of the diamond electrode (0.2 cm^2)] increased with pulse number, as is shown in Table 5.2. It appears that, once formed, the deposition of Pt on existing Pt clusters occurs more facilely than on the bare diamond surface and this leads to a greater microscopic surface roughening with increasing pulse number. The loading also increased with pulse number and this was confirmed by AAS (described in Chapter 2) with calculated values of 2.4, 3.3 and 7.4 $\mu g_{Pt}/cm^2$ measured for just one film at each at pulse numbers of 10, 25 and 50. An important performance parameter for electrocatalytic electrodes is the

specific Pt surface area, defined as the electrochemically active Pt area normalized to the Pt loading. The specific surface area was calculated to be 13, 20 and 14 m^2_{Pt}/g_{Pt}, respectively, and is shown in Table 5.2. This specific surface area, ~15 m^2_{Pt}/g_{Pt}, is about a factor of ten lower than what is necessary for a fuel cell electrode. This is largely due to the low surface area of the planar thin-film electrode.

Table 5.2. Electrochemically Active Pt Surface Area, Roughness Factor (RF) and Specific Pt Surface Area for Pt-Coated Microcrystalline Diamond Films as a Function of the Pulse Number[a]

No. of Pulses	Electrochemically Active Pt Surface Area (cm^2_{Pt})	RF	Specific Pt Surface Area (m^2_{Pt}/g_{Pt})
10	0.06 ± 0.02	0.31	13
25	0.13 ± 0.02	0.64	20
50	0.20 ± 0.02	0.99	14

[a] Pulse width = 1 s. Delay time = 1 s. Current density = 0.50 mA/cm^2 (geometric area). RF is the electrochemically active Pt area obtained from the hydrogen adsorption charge normalized to the geometric area of the diamond film (0.2 cm^2).

The electrodeposition of Pt on microcrystalline diamond was also investigated as a function of the pulse current density from 0.50 to 1.50 mA/cm^2 (geometric area). The deposition was carried out using a pulse number of 10 and a pulse width of 1 s. Increasing the current density has the effect of increasing the overpotential (η) for the reduction reaction, although in this case the actual values are not known. SEM images of metal-coated films are displayed in Figure 5.3A-E. Table 5.3 presents a summary of the particle analysis data. Statistically, the nominal particle size was the same for all five current densities, ranging from 40 to 70 nm with an RSD of approximately 50%. The particle coverage increased from 1.1 (± 0.6) to 7.5 (± 0.9) x 10^9 cm^{-2} with current density

up to 1.25 mA/cm^2. However, the particle coverage for the highest current density, 1.50 mA/cm^2, decreased to 1.9 ($\pm$ 0.9) x 10^9 cm^{-2}. The film deposited at 1.25 mA/cm^2 has particles that are nominally the same size as those produced at 0.50 mA/cm^2, but with a particle density nearly six times greater.

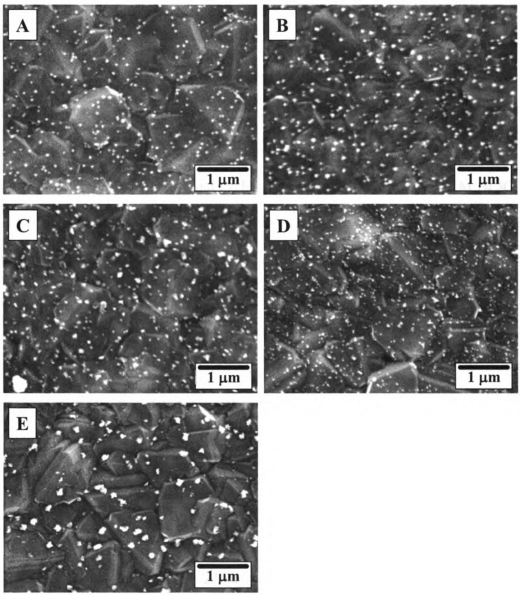

Figure 5.3. Scanning electron micrographs of Pt-coated microcrystalline diamond electrodes deposited at pulse current densities of (A) 0.50, (B) 0.75, (C) 1.00, (D) 1.25 and (E) 1.50 mA/cm^2. Pulse number = 10. Pulse width = 1 s.

Table 5.3. Particle Analysis and Hydrogen Adsorption Data for Pt-Coated Microcrystalline Diamond Films as a Function of the Pulse Current Density[a]

Pulse Current Density (mA/cm^2)[b]	Mean Particle Size (nm)	Particle Coverage (10^9 cm^{-2})[b]	Hydrogen Adsorption Charge (mC/cm^2)[b]
0.50	50 ± 30	1.1 ± 0.6	0.07 ± 0.02
0.75	70 ± 40	1.5 ± 0.4	0.095 ± 0.007
1.00	60 ± 30	2.2 ± 0.6	0.112 ± 0.005
1.25	50 ± 30	7.5 ± 0.9	0.156 ± 0.005
1.50	70 ± 40	1.9 ± 0.9	0.19 ± 0.03

[a] Pulse width = 1 s. Delay time = 1 s. Current density = 0.50 mA/cm^2 (geometric area).
[b] Values normalized to the geometric area of the diamond film (0.2 cm^2)

Figure 5.4 shows background cyclic voltammetric *i-E* curves in 0.1 M $HClO_4$ for the Pt-coated microcrystalline thin-film electrodes formed with different pulse current densities. The scans were initiated at 200 mV with the forward sweep in the positive direction at a rate of 50 mV/s. Again, all the voltammetric features characteristic of clean polycrystalline Pt are present. There is a progressive increase in the total voltammetric current as the deposition current density is increased from 0.50 to 1.50 mA/cm^2, consistent with an increasing electrochemically active metal phase. The charge associated with the H^+ adsorption increases with deposition current density, as shown in Table 5.3. This is due to an increase in particle coverage, as is observed for the films coated at current densities from 0.50 to 1.25 mA/cm^2, and particle roughening.

Table 5.4 shows the estimated metal loading, the electrochemically active Pt area, the specific Pt area and the roughness factor for the Pt-diamond electrodes formed using different pulse current densities. The electrochemically active Pt area and roughness

factor both increase with deposition current density, as reflected in the voltammetric *i-E* curves. This is due to the increase in particle coverage (at least up to 1.25 mA/cm^2) and microscopic roughness of the particles. The measured metal loading increased from 2 to 4 $\mu g_{Pt}/cm^2$ with deposition current density. The specific Pt surface area ranged from 10 to 25 $m^2{}_{Pt}/g_{Pt}$ with the values clustered around 20 $m^2{}_{Pt}/g_{Pt}$.

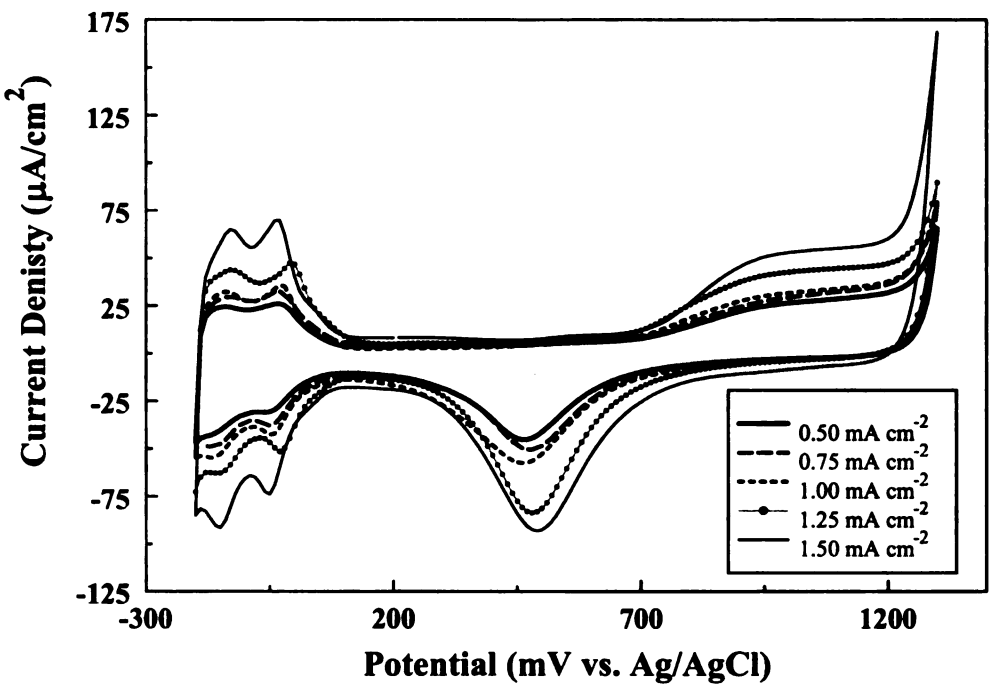

Figure 5.4. Cyclic voltammetric *i-E* curves in degassed 0.1 M $HClO_4$ for microcrystalline diamond electrodes coated with Pt at the different current densities. Pulse number = 10. Pulse width = 1 s. Scan rate 50 = mV/s. The current is normalized to the diamond geometric area, 0.2 cm^2.

Table 5.4. Electrochemically Active Pt Area, Specific Pt Surface Area and Roughness Factor for Pt-Coated Microcrystalline Diamond Films Deposited at Different Pulse Current Densities[a]

Pulse Current Density (mA/cm^2)[b]	Measured Loading ($\mu g_{Pt}/cm^2$)[b]	Electrochemically Active Pt Surface Area (cm^2_{Pt})	RF	Specific Pt Surface Area (m^2_{Pt}/g_{Pt})
0.50	2.4	0.06 ± 0.02	0.31	13
0.75	2.3	0.090 ± 0.007	0.45	20
1.00	2.2	0.107 ± 0.005	0.53	25
1.25	3.4	0.149 ± 0.004	0.74	22
1.50	4.3	0.18 ± 0.04	0.89	21

[a] Pulse number = 10. Pulse width = 1 s. Delay time = 1 s. Loading estimated from AAS measurements of the dissolved metal deposits.
[b] Normalized to the geometric area of the diamond film (0.2 cm^2).

5.2.2 Pt Deposition on Nanocrystalline Diamond

Pulsed galvanostatic deposition was also used to form Pt adlayers on boron-doped nanocrystalline diamond electrodes. Metal deposition is a surface "sensitive" charge-transfer process; therefore, the morphology and microstructure of a substrate electrode can influence the metal phase nucleation and growth. Comparing the deposition at these two diamond types provided insight about the influence of the film microstructure and morphology (*e.g.*, grain boundaries, defects, facets, etc.) on the metal phase formation.

Two deposition conditions were evaluated, ten 1-s pulses at 0.50 and 1.25 mA/cm^2. SEM images of these two metallized surfaces are shown in Figure 5.5A (0.50 mA/cm^2) and B (1.25 mA/cm^2). Nanocrystalline diamond has a much smoother surface morphology than does microcrystalline diamond and a larger fraction of exposed grain boundary due to the smaller aggregate size.[28,29] Though it is currently not as corrosion

resistant as microcrystalline diamond, it still is an improvement over sp^2 carbon materials. The morphology consists of *ca.* 50-100 nm aggregates of diamond crystallites that are 10-20 nm in size. We supposed that the higher fraction of grain boundary might lead to a higher nucleation site density for Pt and, in turn, to smaller particles and higher coverages. It has been observed in other work in our group that this is in fact the case, as nanocrystalline outperforms microcrystalline diamond for the anodic stripping voltammetric determination of dissolved metal ions, in part, because metal phase formation on the former occurs with lower particle size and higher coverage.[50] It can be seen in the images that many of the metal deposits are near the grain boundaries. Particle size analysis of the film in Figure 5.5A revealed a nominal diameter of 70 ± 40 nm (RSD = 57%), which is statistically similar to the particle size seen for microcrystalline diamond at the same current density. The particles are not as uniformly distributed over the surface as they are on the microcrystalline diamond surface, at least under these deposition conditions. The uneven distribution is reflected in a lower particle coverage of 6 (± 5) x 10^8 cm^{-2}, which is an order of magnitude less than that seen for the microcrystalline film.

The metal particles formed at 1.25 mA/cm^2 however, shown in Figure 5.5B, have a smaller nominal size of 30 ± 30 nm (RSD = 100%). The Pt particles are also more uniformly distributed over the surface and this is reflected in a larger particle coverage of 1.9 (± 1.0) x 10^{10} cm^{-2}. Many of the metal particles appear to reside at the grain boundaries, which is consistent with these regions being the primary nucleation sites.

This particle coverage is the highest observed for any of the diamond films under study, microcrystalline or nanocrystalline.

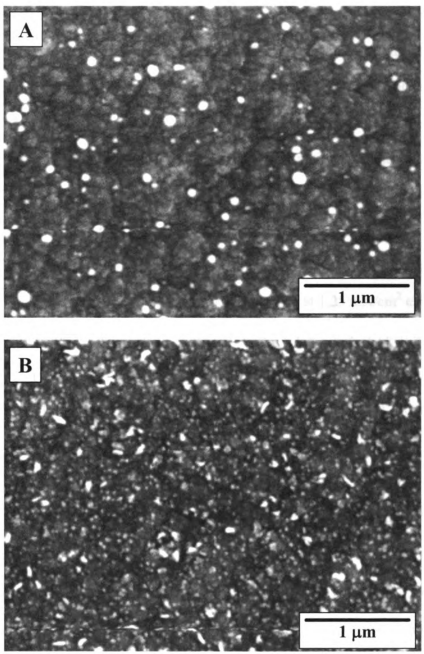

Figure 5.5. Scanning electron micrographs of Pt-coated nanocrystalline diamond electrodes deposited at pulse current densities of (A) 0.50 and (B) 1.25 mA/cm^2. Pulse number = 10. Pulse width = 1 s.

Figure 5.6 shows background cyclic voltammetric *i-E* curves in 0.1 M $HClO_4$ for nanocrystalline diamond thin-film electrodes decorated with Pt that was deposited at 0.50 and 1.25 mA/cm^2. The scans were initiated at 200 mV with the forward sweep in the positive direction at a rate of 50 mV/s. Again, all the voltammetric features characteristic of clean polycrystalline Pt are present. There is an increase in the total voltammetric current for increased deposition current density. This is consistent with the SEM data and results from an increased Pt loading. It is worth noting that the nanocrystalline diamond electrode decorated with Pt at 1.25 mA/cm^2 shows much larger voltammetric currents than does the microcrystalline diamond electrode coated at the same current density. This is due to the smaller nominal particle size and larger particle coverage on the former. Interestingly, the *i-E* curve for the film coated at 1.25 mA/cm^2 exhibits a pre-peak prior to Pt oxide formation at *ca.* 700 mV. This pre-peak is associated with a Pt_xOH species formed prior to the PtO monolayer in the plateau of the curve.[51,52] This peak may be due to Pt_4OH formation on the (100)-oriented surfaces and/or Pt_3OH formation on the (111)-oriented surfaces.[52]

The H^+ adsorption charge for the 0.50 and 1.25 mA/cm^2 films is 0.071 ± 0.010 and 0.25 ± 0.027 mC/cm^2, respectively. The electrochemically active Pt area for the films is 0.07 ± 0.01 (RSD = 15%) and 0.24 ± 0.03 (RSD = 13%) cm^2_{Pt}, respectively. These values result in roughness factors of 0.34 and 1.2. Calculations, based on AAS data revealed approximate Pt loadings of 1.4 and 2.4 $\mu g_{Pt}/cm^2$ for the 0.50 and 1.25 mA/cm^2 deposition currents, respectively. This translates into specific Pt surface areas of

24 and 50 m^2_{Pt}/g_{Pt}, respectively, which are the highest values we have recorded. It appears from these preliminary studies that the diamond film morphology and microstructure do indeed influence the nucleation and growth of Pt, and the highest specific areas are seen for the nanocrystalline films

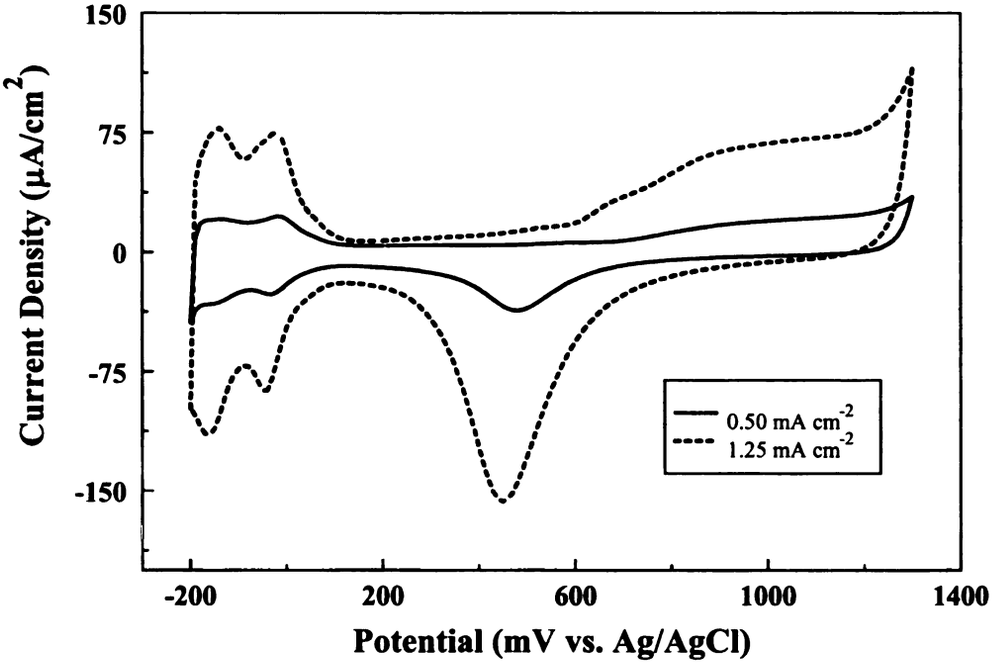

Figure 5.6. Cyclic voltammetric *i-E* curves in degassed 0.1 M $HClO_4$ for nanocrystalline diamond electrodes coated with Pt deposited at 0.50 and 1.25 mA/cm^2. Pulse number = 10. Pulse width = 1 s. Scan rate = 50 mV/s. The current is normalized to the diamond geometric area, 0.2 cm^2.

5.2.3 Comparison Studies with Glassy Carbon

In order to assess how metal deposition on diamond stacks up against deposition on sp^2 carbon electrodes, tests were conducted with glassy carbon. Based on the results discussed previously, the following conditions were selected for Pt deposition: Ten pulses of 1 s duration (delay time of 1 s between pulses) at 1.25 mA/cm^2. SEM was used

to evaluate the metal deposits. The micrograph is shown in Figure 5.7. Particle size analysis revealed a particle diameter of 70 ± 60 nm (RSD = 85%) and a particle coverage of 5 (± 1) x 10^9 cm^{-2}. Cyclic voltammetry was employed, in the same manner as with the Pt/diamond electrodes, to study the Pt activity for H^+ adsorption in 0.1 M $HClO_4$. Integration of the *i-E* curves revealed an H^+ adsorption charge of 0.25 ± 0.02 mC/cm^2 (n = 3). This charge is similar to that seen for the nanocrystalline film and is a little larger than the value for microcrystalline diamond. The electrochemically active Pt area was calculated to be 0.24 ± 0.02 cm^2_{Pt}. In summary, the metal phase formation on glassy carbon under these deposition conditions appears similar to what is seen for both diamond types in terms of the nominal particle size, coverage, and electrochemically active Pt area.

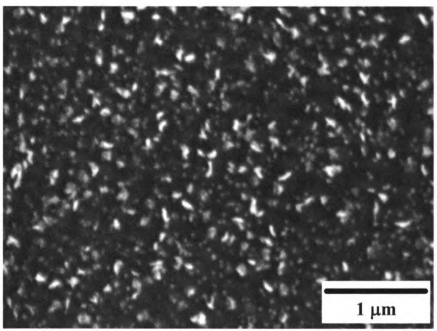

Figure 5.7. Scanning electron micrograph of Pt-coated glassy carbon deposited using 10 pulses of 1 s width at a current density of 1.25 mA/cm^2.

The specific Pt surface areas on diamond were in the range of 10-50 m^2_{Pt}/g_{Pt} (see Tables 5.2 and 5.4). These values are about a factor of 2-10 less than that necessary for a typical fuel cell electrode, which has an area of 100-200 m^2_{Pt}/g_{Pt}. Gloaguen *et al.* reported values of 15-73 m^2_{Pt}/g_{Pt} for adlayers on three different types of carbon powders.[53] It is important to remember that the specific Pt surface area depends on the surface area of the carbon support. Kucernak *et al.* reported values of 20-50 m^2_{Pt}/g_{Pt} for electrodeposited adlayers on highly ordered pyrolytic graphite (HOPG).[54] Mo *et al.* reported on the immobilization of high-area Pt particles on glassy carbon with specific surface areas of *ca.* 30 m^2_{Pt}/g_{Pt}.[55] It is clear that the deposition on diamond yields electrocatalyst structures and activities that are similar to those for other sp^2 carbon support materials.

5.2.4 Investigating Pt Nucleation and Growth Mechanism

In order to control the metal particle properties one must gain a better understanding of the nucleation and growth mechanism of Pt on the diamond substrate. Unlike most materials used to study metal nucleation, diamond is a heterogeneous material both morphologically and electronically. Figure 5.8 shows cyclic voltammetric *i-E* curves for the deposition of Pt on four different carbon surfaces: microcrystalline and nanocrystalline diamond, GC and HOPG. The solution consisted of 1 mM K_2PtCl_6 dissolved in 0.1 M $HClO_4$ and the potential was scanned at a rate of 20 mV/s. The scans were initiated at 1 V and scanned negative with a Pt nucleation peak appearing between -100 and 100 mV (peak I), followed by the onset of hydrogen adsorption at *ca.* -200 mV

(peak II) on the deposited particles. On the subsequent scan, the onset of peak III is observed at *ca.* 900 mV. This is attributed to the formation of oxides on the Pt layer.

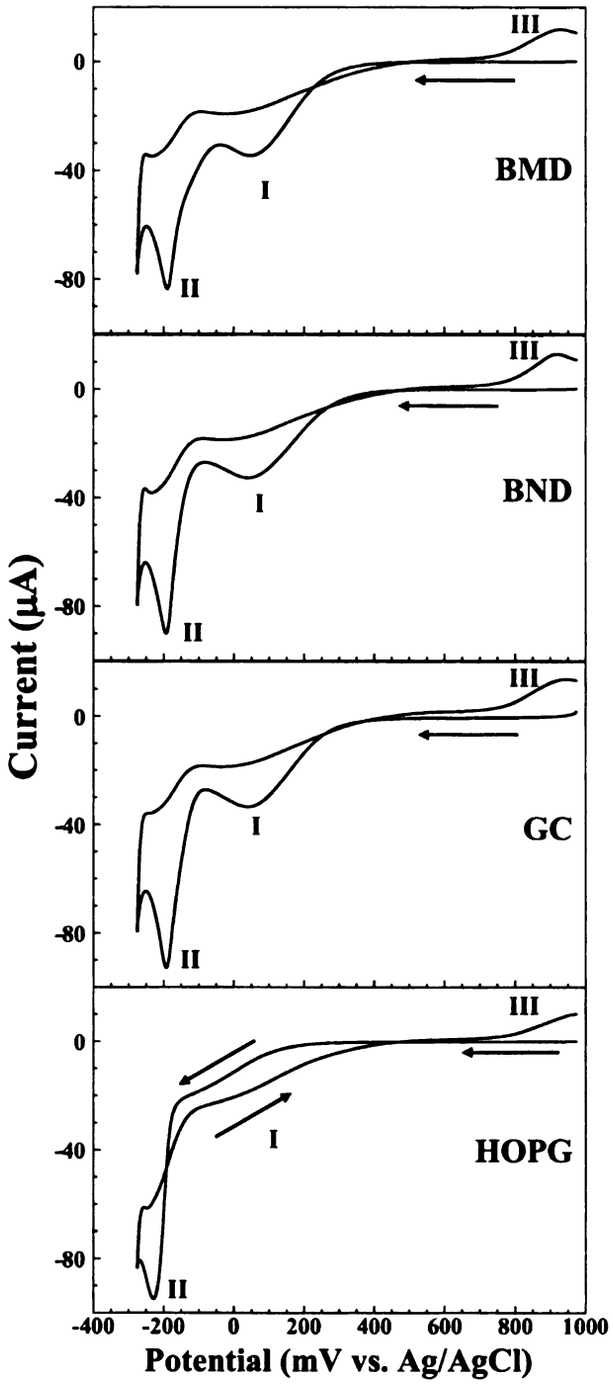

Figure 5.8. Cyclic voltammetric *i-E* curves for 1 mM K_2PtCl_6 + 0.1 M $HClO_4$ on different carbon materials. Scan rate = 20 mV/s.

The *i-E* curve for HOPG, the most ordered material of the four, is quite different from the other curves. This material had the most negative reduction curve for the nucleation of Pt and is the only curve for which the reverse scan was at a lower current (see region between 0 and 200 mV) than the forward scan. This is consistent with the small amount of edge plane exposed on the freshly cleaved HOPG. The edge plane is known to be more active towards the formation of metal adlayer than the basal plane.[39]

The other three carbon materials exhibited a nicely resolved reduction peak positive of 0 mV indicating metal adlayer formation on the surface. There was however, more variability in the reduction peak potential for these materials than observed for the HOPG. The GC exhibited a deviation of *ca.* 50%, while the deviation for both diamond types was >100%. This increase in deviation is likely due to an increase in the disorder in the carbon with the diamond materials being the most heterogeneous. It appears from the curves that an overpotential of approximately -500 mV is required to deposit Pt on the diamond surfaces.

A series of chronoamperometric steps were performed with both diamond types in an attempt to investigate the Pt nucleation mechanism as discussed in Chapter 1. The potential was held at 800 mV, a potential at which no Pt deposition occurs, and stepped to different final potentials at which deposition occurred. The background subtracted *i-t* curves for the microcrystalline and nanocrystalline diamond is presented in Figures 5.9 and 5.10, respectively. Note that the potentials indicate the overpotential for the reaction ($\eta = E_{eq} - E_{Final}$).

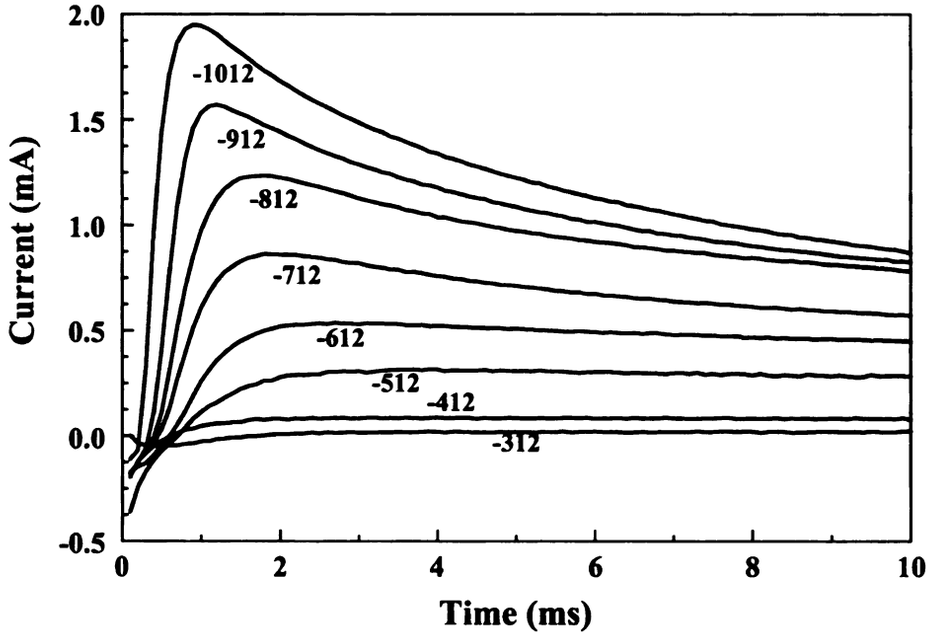

Figure 5.9. Background subtracted chronoamperometric *i-t* curves for Pt deposition on microcrystalline diamond thin film in 1 mM K_2PtCl_6 + 0.1 M $HClO_4$ at the overpotentials indicated in mV.

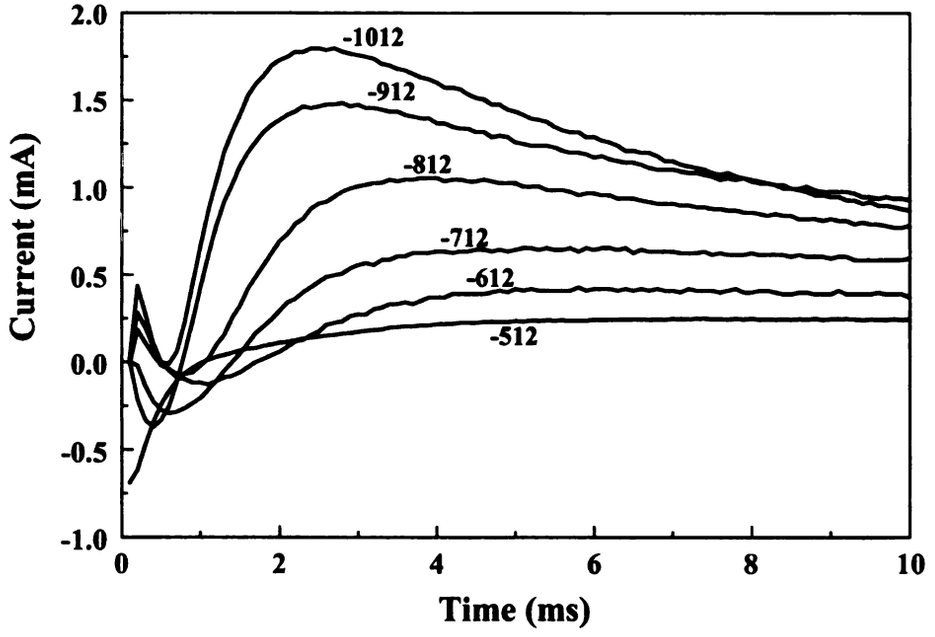

Figure 5.10. Background subtracted chronoamperometric *i-t* curves for Pt deposition on nanocrystalline diamond thin film in 1 mM K_2PtCl_6 + 0.1 M $HClO_4$ at the overpotentials indicated in mV.

As expected, overpotentials less than -500 mV did not cause significant deposition current to flow as seen in Figure 5.9 for overpotentials of -312 and -412 mV. This is consistent with that predicted from the cyclic voltammetric *i-E* curves in Figure 5.8. As the overpotential increases, the resulting current maximum (I_m) increases and is reached at shorter times (t_m) consistent with an increase in the amount of metal deposited and the rate at which it is formed. Following the maximum, the current decreased as depletion layers around each particle start to overlap resulting in a planar diffusion pattern to the electrode.

The *i-t* transients were analyzed according to the theory described by Scharifker and Hills presented in section 1.4. Theoretical curves representing the limiting cases for instantaneous and progressive nucleation mechanisms were constructed based on equations 1.4.1 and 1.4.2, and are the same as those presented in Figure 1.7. The normalized *i-t* transients at the different overpotentials for both diamond types are presented in Figure 5.11A-F. As the overpotential increases, the nucleation on both diamond surfaces transitions from an instantaneous nucleation mechanism towards a more progressive one. This is similar to what was found for Cu deposition on microcrystalline diamond.[56] Interestingly, the curve for the nanocrystalline diamond is always closer to the theoretical curve for progressive nucleation than is the curve for microcrystalline diamond. This perhaps explains the greater dispersity in particle size observed for the Pt/BND films compared to the Pt/BMD films as progressive nucleation generally leads to an increase in particle size dispersion.

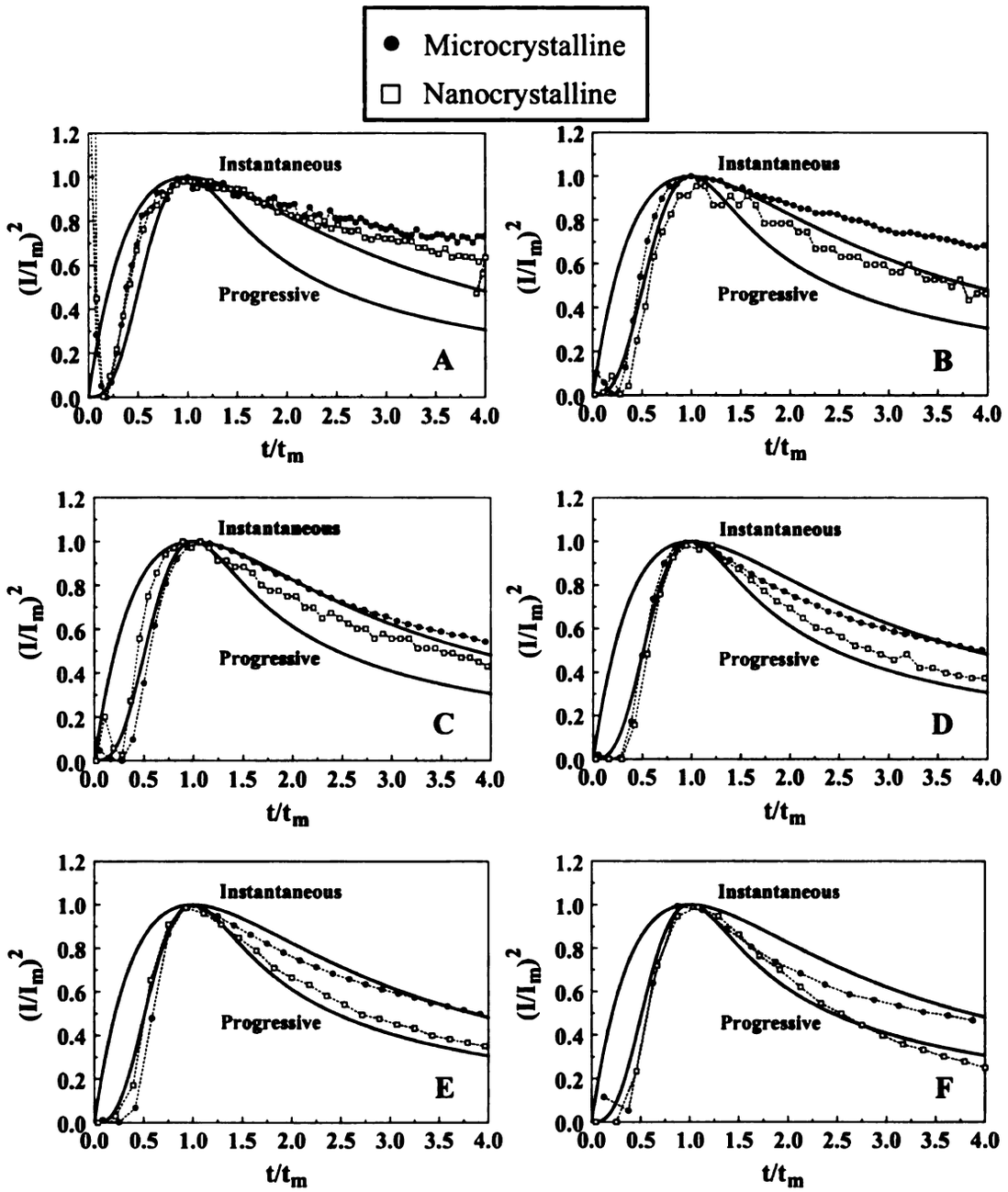

Figure 5.11. Comparison of experimental normalized *i-t* curves for microcrystalline (•) and nanocrystalline (□) diamond with the theoretical curves corresponding to instantaneous and progressive nucleation at overpotentials of (A) -512, (B) -612, (C) -712, (D) -812, (E) -912 and (F) -1012 mV.

As shown in Figure 5.11, the normalized *i-t* curve rarely follows one of the limiting cases perfectly. These limiting cases are for primary nucleation and deviation from these curves is generally attributed to secondary nucleation, however this could also be attributed to a mixture of mechanisms across a heterogeneous surface.[57] However, in Scharifker and Mostany's approach, it is not necessary to classify the nucleation by one of the limiting cases.[58] Instead, the values of I_m and t_m can be used to calculate two parameters: the nucleation rate per active site on the surface, A, and the number density of active sites for nucleation, N_o. We attempted to calculate these values, however, according to this approach, the value for $I_m t_m^{1/2}/a$ (where $a = zfD^{1/2}C/\pi^{1/2}$) needs to fall between 0.7153 (instantaneous) and 0.9034 (progressive). Only two of our chronoamperometric *i-t* curves fit this criterion. They were for overpotentials of -912 and -1012 mV at the nanocrystalline diamond. For these transients, the values for A were 931 and 28.7 s^{-1} and for N_o were 3.5×10^9 and 1.3×10^{11} cm^{-2}, respectively. All the other curves exhibited $I_m t_m^{1/2}/a$ values that were too low, consistent with low values of I_m and/or t_m. It appears that while the rate of Pt nucleation on diamond is quite fast, there is not enough metal deposited to achieve considerable current to satisfy this approach. However, the difference between the values of A and N_o found for the 2 nanocrystalline films is consistent with an increase in both the deposition rate and number of active sites with increasing overpotential as would be expected.

5.2.5 Secondary Diamond Growth

The effect of a secondary diamond growth on the activity and stability of the Pt nanoparticles on microcrystalline diamond was also investigated, and is illustrated in Figure 5.12A-C. Figure 5.12A shows an SEM image of a microcrystalline diamond thin-

film electrode freshly coated with Pt using ten 1-s pulses at a current density of 1.25 mA/cm^2. The SEM image reveals good metal coverage over the entire diamond surface. A nominal particle size of 30 ± 30 nm and particle coverage of 6 (± 2) x 10^9 cm^{-2} were determined from particle size analysis. No loss of Pt activity was observed after long-term solution exposure. The initial hydrogen adsorption charge in 0.1 M $HClO_4$ was 0.21 mC/cm^2. This corresponds to an electrochemically active Pt area of 0.20 cm^2_{Pt}.

The metal-coated film was then subjected to a 20 min diamond deposition using a 0.5% CH_4/H_2 source gas mixture at 1 kW, 200 sccm of total gas flow, 40 Torr, and *ca.* 800 °C. These conditions are not necessarily optimal but rather were selected as a starting point. Figure 5.12B shows an SEM image of the Pt-coated electrode immediately following the secondary diamond growth. A nominal particle size of 40 ± 40 nm and particle coverage of 4 (± 1) x 10^9 cm^{-2} was observed. The slightly larger nominal particle size and lower particle coverage are consistent with some coalescence of neighboring particles as the deposition temperature is *ca.* 800 °C. More importantly, the particle shape changed from a rough, dendritic morphology to a smoother, more rounded morphology during the plasma treatment as a result of annealing effects. This is important as smoothening of the particle surface results in a decrease in surface area.

After the secondary diamond growth, background cyclic voltammetric *i-E* curves were re-recorded in 0.1 M $HClO_4$. The hydrogen adsorption charge decreased to 0.015 mC/cm^2 (a factor of 10 loss), and this corresponds to an electrochemically active Pt area of 0.014 cm^2_{Pt}. There is clearly some loss in Pt activity due to particle coalescence,

annealing of the surface roughness and blockage by the diamond deposition. We also suspect that some percentage of the loss seen here resulted not from "buried" particles but rather from poor alignment of the metallized electrode area inside the O-ring of the cell. The Pt exposed to the solution was anchored strongly and exhibited good stability with the surface area during extended potential cycling (1000 cycles) between -0.4 and 1.9 V vs. Ag/AgCl in 0.1 M $HClO_4$. The maximum currents were near ± 5 mA/cm^2 at the two potential extremes. The hydrogen adsorption charge actually increased slightly, exhibiting a value of 0.020 mC/cm^2 after cycling likely due to removal of carbon contaminants from the surface and particle roughening. This correlates to a calculated electrochemically active surface area of 0.019 cm^2_{Pt}, or an increase of 31%. In comparison, over 63% of the electrochemically active Pt was lost from a metal-coated diamond surface exposed to the same cycling conditions when no secondary diamond growth was applied. The SEM image of the Pt/diamond composite electrode following the extensive electrochemical treatment is shown in Figure 5.12C. There is no visible change compared to the image taken prior to potential cycling. A nominal particle size of 50 ± 40 nm and a particle density of 3 (± 1) x 10^9 cm^{-2} was determined. Both of these values are comparable to those prior to potential cycling supporting our assertion of particle stability. The particle size, particle density, and calculated electrochemically active area for the Pt/diamond film as-deposited, after secondary diamond growth, and after extensive potential cycling are summarized in Table 5.5. Research is ongoing to optimize the secondary diamond growth conditions in order to maximize the particle stability while minimizing the extent of Pt activity loss. One possible alternative is a very short nanocrystalline diamond growth procedure to anchor the metal particles to either a

microcrystalline or nanocrystalline diamond surface without significantly covering the smaller catalyst particles.

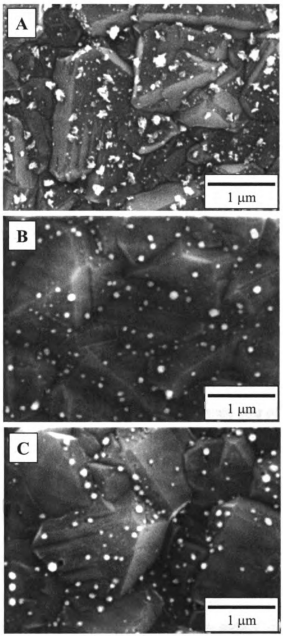

Figure 5.12. Scanning electron micrographs of Pt-coated microcrystalline diamond electrode (A) before, (B) after a 20 min secondary microcrystalline diamond growth and (C) the film with the secondary diamond growth after extensive potential cycling (1000 cycles between *ca.* ±5 mA/cm^2 (geometric area)). Pulse number = 10. Current density = 1.25 mA/cm^2. Pulse width = 1 s.

Table 5.5. Particle Analysis and Electrochemically Active Pt Area for Pt-Coated Microcrystalline Diamond Film Subjected to 20 min Secondary Diamond Growth Procedure and Extensive Potential Cycling

Pt/diamond	Mean Particle Size (nm)	Particle coverage (10^9 cm^{-2})	Electrochemically Active Pt Area (cm^2_{Pt})
As-deposited	30 ± 30	6 ± 2	0.20
After 2° BMD Growth	40 ± 40	4 ± 1	0.014
After Potential Cycling	50 ± 40	3 ± 1	0.019

5.3 Discussion

The results presented herein demonstrate that pulsed galvanostatic deposition is a useful method for depositing nanometer-sized particles of Pt on diamond electrode surfaces. In terms of the nominal particle size, particle coverage, and electrochemically active Pt, pulsed deposition is superior to constant current deposition.[19-21] The optimum conditions for depositing Pt on both types of diamond were ten 1-s pulses at 1.25 mA/cm^2 with a 1 s delay between each pulse. The nominal particle size of *ca.* 30 nm and particle coverage of *ca.* 10^{10} cm^{-2} seen for the nanocrystalline film are good values for a supported electrocatalyst. These values are also comparable to what was achieved with glassy carbon, indicating that metal deposition on diamond occurs in a similar manner to that on a sp^2 carbon electrode.

The basic objective of pulsed deposition is to reduce the particle growth rate, which is expected to reduce the interactions between closely space ones. While we did not monitor the deposition and growth of the metal particles *in situ*, there are some trends

in the data that shed light on the mechanistic aspects of the deposition. The nominal particle size increased and the particle coverage decreased with increasing pulse number at a fixed deposition current density (*i.e.*, constant η). It appears from our results that the initial nucleation occurs at a fixed number of sites and that new Pt particles nucleate and grow primarily on existing Pt rather than forming at new sites on the diamond surface. This explains the rough, dendritic morphology of the deposits. With longer pulse times, and therefore more charge passed, the growth of neighboring nuclei eventually becomes coupled. This results in particle coalescence, reduced particle coverage and an increased nominal particle size.

Increasing the deposition current density (*i.e.*, increasing η) produced increased particle coverage up to the 1.25 mA/cm^2 level, at which point particle coalescence began to occur. It is possible that the increased current density activates areas of the electrode surface that were not active for metal phase formation at lower current density. The observation is consistent with nucleation via a more progressive mechanism, in agreement with the chronoamperometric *i-t* curves. Growth of new Pt particles occurred on both existing Pt sites and at sites on the diamond surface. We have previously found using EC-AFM and *i-t* transient measurements, that the nucleation of Cu on microcrystalline diamond follows an instantaneous mechanism at low overpotentials ($\eta <$ 500 mV) and shifts to a progressive mechanism at higher overpotentials.[56] This is in agreement with that found here for Pt deposition on microcrystalline and nanocrystalline diamond thin film. Additionally, Vinokur *et al.* studied the electrodeposition of Ag and Hg on diamond using *i-t* transients and found that the mechanism of nucleation depended

on the overpotential and the metal ion concentration.[34] At low overpotentials, instantaneous nucleation was observed and at high overpotentials or metal ion concentrations the process became progressive. Preliminary results using EC-AFM and *i-t* transients have revealed that the electrodeposition of the more electronegative Zn on microcrystalline diamond follows a more progressive nucleation mechanism at both low and high overpotentials.[56]

Finally, it is useful to consider what challenges exist for electrochemically producing a dimensionally uniform metal adlayer on polycrystalline diamond. The condition of the deposition method certainly will impact the dimensional uniformity of the metal deposits, as does the heterogeneity of the electrode's microstructural and electronic properties. Electrically conducting diamond is a heterogeneous electrode material, both microstructurally and electronically. The polycrystalline films possess diamond crystallites or grains, grain boundaries, and a multitude of other defects (*e.g.*, dislocations, step edges, etc.). The microcrystalline films are rough with grain boundaries between the crystallites that could serve as sites of higher coordination for the metal phase, whereas the nanocrystalline films are smoother but possess a high fraction of exposed grain boundary due to the small crystallite size. We suppose that the grain boundaries are the primary nucleation sites initially and, therefore, the high grain boundary density leads to a smaller nominal particle size and larger particle coverage.

The electronic properties of diamond also play a key role on the dispersion and uniformity of metal adlayers. The electronic properties of diamond are controlled in a

complex manner by (*i*) the boron doping level and distribution throughout the film,[59-64] (*ii*) incorporated hydrogen which can act both as an acceptor and provide a charge carrier or as a donor and passivate a boron acceptor,[65-69] and (*iii*) defect density.[64,70,71] Of these, the boron doping level and distribution are probably the most influential. Furthermore, it is known that boron incorporates into polycrystalline diamond with different concentrations depending on the growth sector.[72,73] The boron concentration in the {111} growth sector is five or more times greater than that found in the {100} sector. In other words, polycrystalline diamond, particularly the microcrystalline films, is composed of sites of faster (reversible) kinetics where the dopant level is high and sites of slower kinetics (less reversible) where there is less dopant. We have recently observed such electrical and electrochemical heterogeneity using CP-AFM mapping and scanning electrochemical microscopy (SECM) of microcrystalline diamond films.[48,74] Similar heterogeneity is seen for the nanocrystalline films as well. An example of this is shown in Figure 5.13A-D. Both height mode images and conductivity maps are presented over a 10 x 10 (A) and 1 x 1 μm (C) area. Nodular features are seen in the images that are ~50-100 nm in dimension. These are actually a collection of diamond grains that are 10-20 nm in size.[28,29] The intersection of the nodules constitutes the grain boundaries. The figure also shows conductivity maps over the same areas (B and D). In these measurements, a Au-coated Si tip contacting the surface was rastered over an area and the current was measured using a bias voltage of +2 V ($E_{tip} - E_{substrate}$). The bright areas correspond to regions of higher conductivity and the darker features to regions of lower conductivity. Clearly, there are conductivity variations across the surface. The more conductive regions do not appear to be exclusively at the grain boundaries. The higher

resolution image in Figure 5.13D reveals that the distance between the more conducting zones is on the order of 200-300 nm in some cases. These data are important and have implications for the dimensional uniformity of the metal adlayers. The take-home message is that inherently there is going to be spatial variation in the metal adlayer formation on polycrystalline diamond due to this heterogeneity in electrical conductivity. It remains to be proven but it is logical to suppose that the conductive regions are the sites where initial nucleation occurs. Therefore, the fraction of these conductive sites on a film will control the initial nucleation density. A similar conclusion was recently reached by Enea *et al.* in their AFM study of the electrodeposition of Pt on polycrystalline diamond.[35]

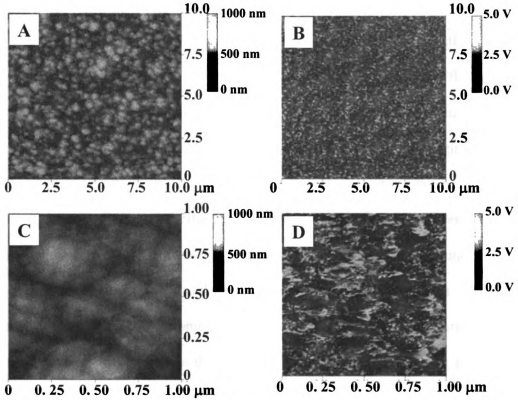

Figure 5.13. AFM height mode images (air) of a boron-doped nanocrystalline diamond thin film over a (A) 10 x 10 and (C) 1 x 1 μm area. Simultaneously recorded conductivity maps of the same regions (B and D) with a bias voltage of +2 V ($E_{tip} - E_{substrate}$).

5.4 Conclusions

The pulsed galvanostatic deposition of Pt electrocatalyst particles on boron-doped microcrystalline and nanocrystalline diamond thin film was investigated. The deposition was studied as a function of the pulse number and current density, while maintaining a pulse length of 1-s and a duty cycle of 50%. Pulsed galvanostatic deposition produced a nominal particle size that was an order of magnitude smaller than that previously observed for constant current deposition.[19,20] Deposition using ten pulses and a current density of 1.25 mA/cm^2 yielded the most ideal electrocatalyst on both diamond types, in

terms of the nominal particle size, particle coverage and the highest specific Pt surface area. For both electrode types, the nominal particle size was *ca.* 30 nm with an RSD of 50% or less, and the particle coverage was *ca.* 10^9-10^{10} cm^{-2} under the optimum deposition conditions. The typical specific surface areas were in the 10-50 m^2_{Pt}/g_{Pt} range. The deposition of Pt on diamond compared favorably to deposition on glassy carbon. The microstructure and morphology of diamond strongly influenced the nucleation and growth of Pt. The highest specific surface area of 50 m^2_{Pt}/g_{Pt} was observed for the nanocrystalline film, which possesses a higher fraction of exposed grain boundaries. The grain boundaries appear to serve as the primary nucleation sites on this film. Finally, the influence of the film's electronic properties on the metal phase formation was investigated. The polycrystalline diamond film is quite heterogeneous in terms of the electrical conductivity, as evidenced by CP-AFM. The film is composed of sites of faster (reversible) kinetics where the dopant level is high and sites of slower kinetics (less reversible) where there is less dopant. It is supposed that the regions of high electrical conductivity serve as the initial nucleation sites.

REFERENCES

1. E. Antolini, *J. Mater. Sci.*, **38**, 2995 (2003).

2. F. Rodríguez-Reinoso, *Carbon*, **36**, 159 (1998).

3. L. Carrette, K. A. Friedrich, and U. Stimming, *Fuel Cells*, **1**, 5 (2001).

4. J. Y. Lucisano, J. C. Armour, and D. A. Gough, *Anal. Chem.*, **59**, 736 (1987).

5. A. Damjanovic and V. Brusic, *Electrochim. Acta*, **12**, 615 (1967).

6. N. Giordano, E. Passalacqua, L. Pino, A. S. Aricó, V. Antonucci, M. Vivaldi, and K. Kinoshita, *Electrochim. Acta*, **36**, 1979 (1991).

7. N. M. Markovic, T. J. Schmidt, V. Stamenkovic, and P. N. Ross, *Fuel Cells*, **1**, 105 (2001).

8. H.-H. Yang and R. L. McCreery, *J. Electrochem. Soc.*, **147**, 3420 (2000).

9. T. Yano, E. Popa, D. A. Tryk, K. Hashimoto, and A. Fujishima, *J. Electrochem. Soc.*, **146**, 1081 (1999).

10. E. Yeager, *Electrochim. Acta*, **29**, 1527 (1984).

11. I. Morcos and E. Yeager, *Electrochim. Acta*, **15**, 953 (1970).

12. E. Yeager, J. A. Molla, and S. Gupta, in *Electrochemistry of Carbon*, S. Sarangapani, J. R. Akridge, and B. Schumm, Editors, **PV 84-5**, p. 123, The Electrochemical Society Proceedings Series, Pennington, NJ, (1984).

13. E. Yeager and D. Tryk, in *Proceedings of the 33rd International Power Sources Symposium*, The Electrochemical Society, Inc., Cherry Hill, NJ, (1988).

14. B. C. H. Steele and A. Heinzel, *Nature*, **414**, 345 (2001).

15. E. Auer, A. Freund, J. Pietsch, and T. Tacke, *Appl. Catal. A: Gen.*, **173**, 259 (1998).

16. A. J. Appleby, *Corrosion (Houston)*, **43**, 398 (1987).

17. R. Makharia, P. Yu, J. Pisco, S. Kocha, and H. Gasteiger, Paper 1888 presented at The 206th Meeting of the Electrochemical Society, Honolulu, HI, Oct. 3-8, 2004.

18. J. Wang, G. M. Swain, T. Tachibana, and K. Kobashi, *Electrochem. Solid-State Lett.*, **3**, 286 (2000).

19. J. Wang and G. M. Swain, *Electrochem. Solid-State Lett.*, **5**, E4 (2002).

20. J. Wang and G. M. Swain, *J. Electrochem. Soc.*, **150**, E24 (2003).

21. M. Hupert, A. Muck, J. Wang, J. Stotter, Z. Cvackova, S. Haymond, Y. Show, and G. M. Swain, *Diamond and Rel. Mater.*, **12**, 1940 (2003).

22. A. E. Fischer and G. M. Swain, *J. Electrochem. Soc.*, **152**, B369 (2005).

23. A. E. Fischer, *Degradation Mechanisms of Carbon-Based Electrocatalyst Support Materials and Development of an Advanced Support Based on Electrically Conducting Diamond*, Michigan State University, East Lansing, MI, (2005).

24. G. M. Swain, *J. Electrochem. Soc.*, **141**, 3382 (1994).

25. J. Xu, M. C. Granger, Q. Chen, J. W. Strojek, T. E. Lister, and G. M. Swain, *Anal. Chem.*, **69**, 591A (1997).

26. M. C. Granger, J. Xu, J. W. Strojek, and G. M. Swain, *Anal. Chim. Acta*, **397**, 145 (1999).

27. G. M. Swain, A. B. Anderson, and J. C. Angus, *MRS Bull.*, **23**, 56 (1998).

28. Q. Chen, D. M. Gruen, A. R. Krauss, T. D. Corrigan, M. Witek, and G. M. Swain, *J. Electrochem. Soc.*, **148**, E44 (2001).

29. Y. Show, M. A. Witek, P. Sonthalia, and G. M. Swain, *Chem. Mater.*, **15**, 879 (2003).

30. A. E. Fischer, Y. Show, and G. M. Swain, *Anal. Chem.*, **76**, 2553 (2004).

31. M. Awada, J. W. Strojek, and G. M. Swain, *J. Electrochem. Soc.*, **142**, L42 (1995).

32. Y. Zhang, S. Asahina, S. Yoshihara, and T. Shirakashi, *Electrochim. Acta*, **48**, 741 (2003).

33. S. Nakabayashi, D. A. Tryk, A. Fujishima, and N. Ohta, *Chem. Phys. Lett.*, **300**, 409 (1999).

34. N. Vinokur, B. Miller, Y. Avyigal, and R. Kalish, *J. Electrochem. Soc.*, **146**, 125 (1999).

35. O. Enea, B. Riedo, and G. Dietler, *Nano Letters*, **2**, 241 (2002).

36. E. Budevski, G. Staikov, and W. J. Lorenz, *Electrochemical Phase Formation and Growth*, VCH, New York (1996).

37. M.-S. Löffler, B. Groß, H. Natter, R. Hempelmann, T. Krajewski, and J. Divisek, *Phys. Chem. Chem. Phys.*, **3**, 333 (2001).

38. J. V. Zoval, R. M. Stiger, P. R. Biernacki, and R. M. Penner, *J. Phys. Chem.*, **100**, 837 (1996).

39. J. V. Zoval, J. Lee, S. Gorer, and R. M. Penner, *J. Phys. Chem. B*, **102**, 1166 (1998).

40. J. L. Fransaer and R. M. Penner, *J. Phys. Chem. B*, **103**, 7643 (1999).

41. S. Gorer, H. Liu, R. M. Stiger, M. P. Zach, J. V. Zoval, and R. M. Penner, in *Metal Nanoparticles*, D. L. Feldheim and C. A. Foss Jr., Editors, p. 237, Marcel Dekker, Inc., New York, New York, (2002).

42. R. M. Penner, *J. Phys. Chem. B*, **105**, 8672 (2001).

43. R. M. Penner, *J. Phys. Chem. B*, **106**, 3339 (2002).

44. H. Liu, F. Favier, K. Ng, M. P. Zach, and R. M. Penner, *Electrochim. Acta*, **47**, 671 (2001).

45. H. Liu and R. M. Penner, *J. Phys. Chem. B*, **104**, 9131 (2000).

46. G. Gunawardena, G. Hills, I. Montenegro, and B. Scharifker, *J. Electroanal. Chem.*, **138**, 225 (1982).

47. P. Allongue and E. Souteyrand, *J. Electroanal. Chem.*, **286**, 217 (1990).

48. S. Wang and G. M. Swain, *Manuscript in preparation.*

49. A. Essalik, K. Amouzegar, and O. Savadogo, *J. Appl. Electrochem.*, **25**, 404 (1995).

50. P. Sonthalia, E. McGaw, Y. Show, and G. M. Swain, *Anal. Chim. Acta*, **522**, 35 (2004).

51. H. Angerstein-Kozlowska, B. E. Conway, and W. B. A. Sharp, *J. Electroanal. Chem.*, **43**, 9 (1973).

52. B. V. Tilak, B. E. Conway, and H. Angerstein-Kozlowska, *J. Electroanal. Chem.*, **48**, 1 (1973).

53. F. Gloaguen, J.-M. Léger, and C. Lamy, *J. Appl. Electrochem.*, **27**, 1052 (1997).

54. A. R. Kucernak, P. B. Chowdhury, C. P. Wilde, G. H. Kelsall, Y. Y. Zhu, and D. E. Williams, *Electrochim. Acta*, **45**, 4483 (2000).

55. Y. Mo, S. Sarangapani, A. Le, and D. A. Scherson, *J. Electroanal. Chem.*, **538-539**, 35 (2002).

56. J. Wang, Ph.D. Dissertation, *Fabrication, Characterization, And Electrocatalytic Activity of Metal/Diamond Composite Electrodes*, Michigan State University, East Lansing, MI, (2002).

57. L. M. Plyasova, I. Y. Molina, A. N. Gavrilov, S. V. Cherepanova, O. V. Cherstiouk, N. A. Rudina, E. R. Savinova, and G. A. Tsirlina, *Electrochim. Acta*, **51**, 4477 (2006).

58. B. R. Scharifker and J. Mostany, *J. Electroanal. Chem.*, **177**, 13 (1984).

59. J. T. Huang, C. S. Hu, J. Hwang, H. Chang, and L. J. Lee, *Appl. Phys. Lett.*, **67**, 2382 (1995).

60. K. Nishimura, K. Das, and J. T. Glass, *J. Appl. Phys.*, **69**, 3142 (1991).

61. N. Vinokur, B. Miller, Y. Avyigal, and R. Kalish, *J. Electrochem. Soc.*, **143**, L238 (1996).

62. M. N. Latto, G. Pastor-Moreno, and D. J. Riley, *Electroanalysis*, **16**, 434 (2004).

63. R. F. Mamin and T. Inushima, *Phys. Rev. B*, **63**, 033201 (2001).

64. W. Zhu, in *Diamond: Electronic Properties and Applications*, L. S. Pan and D. R. Kania, Editors, p. Chapter 5, Kluwer Academic Publishers, Boston, (1995).

65. M. I. Landstrass and K. V. Ravi, *Appl. Phys. Lett.*, **55**, 1391 (1989).

66. K. Hayashi, S. Yamanaka, H. Okushi, and K. Kajimura, *Appl. Phys. Lett.*, **68**, 376 (1996).

67. H. J. Looi, R. B. Jackman, and J. S. Foord, *Appl. Phys. Lett.*, **72**, 353 (1998).

68. H. J. Looi, L. Y. S. Pang, A. B. Molloy, F. Jones, J. S. Foord, and R. B. Jackman, *Diamond and Rel. Mater.*, **7**, 550 (1998).

69. H. J. Looi, M. D. Whitfield, J. S. Foord, and R. B. Jackman, *Thin Solid Films*, **343-344**, 623 (1999).

70. B. Fiegl, R. Kuhnert, M. Ben-Chorin, and F. Koch, *Appl. Phys. Lett.*, **65**, 371 (1994).

71. D. Stenbach, A. Flöter, H. Güttler, R. Zachai, and P. Ziemann, *Diamond and Rel. Mater.*, **8**, 273 (1999).

72. T. Kolber, K. Piplits, R. Haubner, and H. Hutter, *Fresenius. J. Anal. Chem.*, **365**, 636 (1999).

73. K. Ushizawa, K. Watanabe, T. Ando, I. Sakagucki, M. Nishitani-Gamo, Y. Sato, and H. Kanada, *Diamond and Rel. Mater.*, **7**, 1719 (1998).

74. K. B. Holt, A. J. Bard, Y. Show, and G. M. Swain, *J. Phys. Chem. B*, **108**, 15117 (2004).

CHAPTER 6

The Effect of Surface Chemistry on Metal Phase Formation and Particle Stability

6.1 Introduction

Our effort developing diamond as an advanced electrocatalyst support material involves learning how to form and stabilize Pt catalyst particles on the surface.[1-6] Most of the metal electrodeposition research reported to date has been performed with H-terminated diamond (microcrystalline and nanocrystalline) thin-film electrodes. Therefore, little is known about how the surface chemistry influences metal phase formation and stability. Recently, some work on the formation of metal catalyst particles on oxidized diamond film was reported.[7] In this work, Zhang *et al.* observed that Au particles electrodeposited on an oxidized diamond surface form as 40-400 nm clusters located principally near the grain boundaries. In comparison, Au particles electrodeposited on hydrogen-terminated diamond were randomly dispersed over the whole surface with a nominal diameter of *ca.* 60 nm. This suggests that the oxidized grains of diamond are less favorable sites for metal phase formation.

Understanding how these metal phases form and interact with diamond is necessary because there is considerable research showing the importance of metal-support interactions in electrocatalytic reactions; specifically, the effect of carbon surface oxides on supported catalysts.[8-18] In general, an increase in carbon-oxygen functionality

on various sp^2-bonded carbon supports has little influence on the catalyst morphology (*i.e.*, real Pt area); however, the particles often exhibit increased catalytic activity for certain reactions. For example, Jovanović *et al.* found that electrochemically oxidizing glassy carbon lead to both a better distribution of Pt over the surface and an increase in activity towards methanol oxidation, but did not significantly affect the real Pt surface area.[18] They attributed the increased activity to (*i*) a higher percentage of acidic groups on the oxidized GC promoting a higher fraction of oxygen containing species in the Pt catalyst and (*ii*) OH-like functional groups present on the oxidized GC promoting the oxidation of absorbed intermediates in the oxidation reaction.[18] Similar results were found by Gloaguen *et al.* for Pt potentiostatically deposited on graphite powder and carbon black.[14] They determined that neither the structure of the carbon support nor the amount of surface oxide significantly affected the particle morphology. However, the increased surface oxide content did lead to an increase in both the Pt mass and specific activity for methanol oxidation.

Chapter 5 of this dissertation presented a comparison of Pt metallization of both microcrystalline (BMD) and nanocrystalline (BND) diamond thin-film electrodes by pulsed galvanostatic deposition. The effect of the morphology and microstructure on the nucleation and growth of Pt electrocatalyst particles was studied as a function of the pulse current density and pulse number. In this chapter, how the surface chemistry of microcrystalline and nanocrystalline diamond surfaces affects the formation and stabilization of Pt particles is reported on. The surface chemistries studied were hydrogen (H-terminated), oxygen formed by chemical oxidation (O-terminated), 4-

nitrobenzene diazonium-modified (4-NBD) and 4-methoxybenzene diazonium-modified (4-MBD). The comparison surface is the H-terminated one as such films emerge from the CVD reactor after growth. The O-terminated surfaces were studied because oxygen is slowly incorporated during air exposure. The effect of surface oxides on metal formation and stability are particularly important for fuel cell applications as the electrocatalyst support material slowly oxidizes. The aryl molecule modification was used to see if the molecular adlayer would act as an extension of the electrode surface or simply as a blocking layer. Specifically, 4-NBD was selected because it had already been used by our group in other work, which revealed that diamond surfaces can be modified with this molecule.[19-21] Finally, 4-MBD (derivatized with SO_3- groups) was chosen to see if excess surface charge can influence metal phase formation.[22] The Pt adlayers were deposited by pulsed galvanostatic deposition using the parameters described in Chapter 5 (ten 1-s pulses with a 50% duty cycle at a pulse current density of 1.25 mA/cm^2). This work is part of our long-term goal of understanding metal phase formation on diamond and gaining fundamental insight into what electrode properties affect the particle formation and stability. The Pt-coated films were characterized by scanning electron microscopy (SEM) and cyclic voltammetry. The catalytic activity of the electrode toward the oxygen reduction reaction in acid was investigated at room temperature.

6.2 Results & Discussion

6.2.1 Physical Characterization

The target particle size and density for the catalytic Pt phase is *ca.* 10 nm and 10^{10} cm^{-2}, respectively. Scanning electron micrographs of Pt adlayers formed on BMD surfaces terminated by (A) H, (B) O, (C) 4-NBD and (D) 4-MBD are shown in Figure 6.1A-D. A summary of the particle analysis data is presented in Table 6.1. The particles on BMD_H are spherical, moderately rough and evenly distributed over the entire surface including the facets and grain boundaries. The nominal particle diameter and density were 40 ± 30 nm and 8 (± 1) x 10^9 cm^{-2}.[6] A lower density of particles with a larger nominal diameter is seen on BMD_{ox} (B). This is consistent with the observation made by Zhang *et al.* for oxidized diamond.[7] The particles are fairly spherical, but rougher than those on BMD_H and unevenly distributed over the surface indicating that certain regions are more favorable for metal adlayer formation than others. The nominal size was 100 ± 50 nm and the particle density was 1 (± 1) x 10^9 cm^{-2}. The increase in particle roughness and size as well as the decrease in density, as compared with BMD_H, is consistent with a decrease in the number of active sites initially available for metal deposition and consequent metal deposition on pre-existing growth centers. It appears that the surface carbon-oxygen functionalities block sites for metal phase formation possibly by lowering the surface electrical conductivity.[23]

Figure 6.1C and D show Pt deposited on $BMD_{4\text{-}NBD}$ and $BMD_{4\text{-}MBD}$, respectively. The nominal particle size on both of these surfaces was similar, 80 ± 50 nm and 70 ± 30 nm, respectively. Similar particle coverages of 4 (± 2) and 6 (± 3) x 10^9 cm^{-2} were also

observed. There is a larger deviation in the particle density on the aryl-modified surfaces compared to the hydrogenated surface. This is likely due to variation in the aryl-layer formation on the heterogeneous diamond surface. We suspect that while the aryl-admolecule coverage, determined by integrating the faradaic charge associated with the 1-electron reduction of the nitro functional group $\left(\text{Ar-NO}_2 + e^- \rightarrow \text{Ar-NO}_2^{\bullet}\right)$, is the equivalent of a theoretical monolayer, it is likely that the aryl-adlayer formed as a multilayer in isolated regions over the surface. Such was a conclusion from tapping mode AFM measurements.[21] The similar particle size and density possessed by each film suggests that the 4-MBD modification procedure does not inhibit Pt formation. Recall that the 4-MBD contains SO_3^- functional groups and the reactant is the anionic $PtCl_6^{4-}$ species. Additionally, the particles on these surfaces were not as spherical as those seen on the H- and O-terminated films, but rather more elongated. This is possibly due to blocking caused by the aryl-adlayer. Particle roughness was difficult to determine for $BMD_{4\text{-NBD}}$ due to the tendency for this film to charge in the SEM, however $BMD_{4\text{-MBD}}$ exhibited particles that were quite dendritic in nature.

All three surface chemistries examined provided no benefit in terms of achieving the target nominal particle size and coverage. In fact, it appears that all three chemistries act as partial blocking layers, either because of chemical or electronic effects. The H-terminated surface yielded the best particle characteristics. Certainly, the particle size was increased, the particle density was reduced and the particle shape was affected by the three surface chemistries. The particle shape for the Pt/BMD_H film appeared to be

spherical but the shapes for the $Pt/BMD_{4\text{-}NBD}$ and $Pt/BMD_{4\text{-}MBD}$ films were more elongated and dendritic with high surface area.

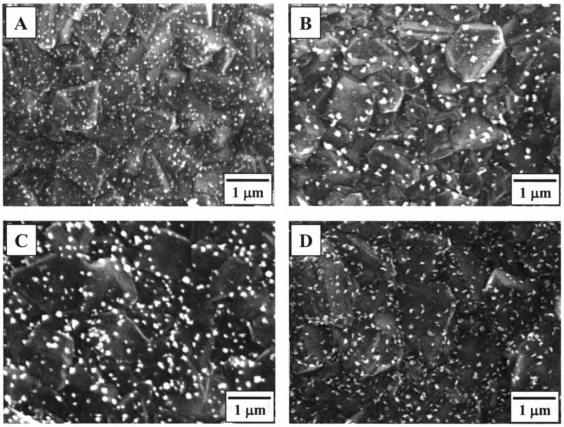

Figure 6.1. Scanning electron micrographs of as-deposited Pt/BMD electrodes deposited using ten 1-s pulses at 1.25 mA/cm^2. The BMD surfaces were (A) H-terminated, (B) O-terminated, (C) 4-NBD modified and (D) 4-MBD modified.

Table 6.1. Particle Analysis Data for Pt-Coated Microcrystalline and Nanocrystalline Diamond Films as a Function of the Surface Chemistry

Surface Chemistry	Microcrystalline Diamond		Nanocrystalline Diamond	
	Particle Size (nm)	Particle Coverage (10^9 cm^{-2})[a]	Particle Size (nm)	Particle Coverage (10^9 cm^{-2})[a]
H-terminated	40 ± 30	8 ± 1	30 ± 30	20 ± 10
O-terminated	100 ± 50	1 ± 1	130 ± 60	0.5 ± 0.3
4-NBD modified	80 ± 50	4 ± 2	100 ± 50	1 ± 1
4-MBD modified	70 ± 30	6 ± 3	50 ± 30	5 ± 3

[a] Area normalized to geometric area of diamond, 0.2 cm^2.

Pt deposition was also performed on BND thin films modified by the same chemistries. The high resolution SEM images and particle analysis data are shown in Figure 6.2A-D and Table 6.1, respectively. BND_H (A) possessed particles that were mostly spherical, quite rough, and distributed evenly over the surface. The particles were nominally 30 ± 30 nm in size at a density of 20 (± 10) x 10^9 cm^{-2}.[6] Of all the films tested, this one most closely meets the desired targets for particle size and density. This particular image shows many particles on the order of 30 nm, plus a few that are sizably larger. The oxidized microcrystalline diamond, BND_{ox} (B) possessed spherical particles that were significantly (*i.e.*, an order of magnitude) larger and less dense than those seen for BND_H. Additionally, these larger agglomerates possess an increased roughness compared to Pt/BND_H. The average particle diameter was 130 ± 60 nm and the particle density was 5 (± 3) x 10^8 cm^{-2}. The H-terminated sample had particles deposited over the entire surface. The O-terminated sample had a much more localized distribution of metal particles. $BND_{4\text{-}NBD}$ (C) exhibited a nominal particle size of 100 ± 50 nm and a particle

density of 1 (± 1) x 10^9 cm^{-2}. The larger size and lower density, as compared to the H-terminated surface, is consistent with a blocking effect produced by the aryl-adlayer that results in a decrease in the number of active sites for metal phase formation. While there are a significant number of particles that are quite spherical, there are a large number of agglomerates that are elongated and quite dendritic. Finally, $BND_{4\text{-}MBD}$ exhibited a nominal particle size and density of 50 ± 30 nm and 5 (± 3) x 10^9 cm^{-2}, respectively. Again, the aryl-adlayer modification produced non-spherical particles that were quite rough. Interestingly, the type of aryl molecule used to modify the surface had a more significant impact on particle size and density on the nanocrystalline diamond than on the microcrystalline diamond. Perhaps the aryl molecules are more evenly distributed on the smoother nanocrystalline surface, whereas modifying the rough microcrystalline surface results in an uneven distribution of the adlayer. This results in voids in the modified layer and less impact on the metal deposition process.

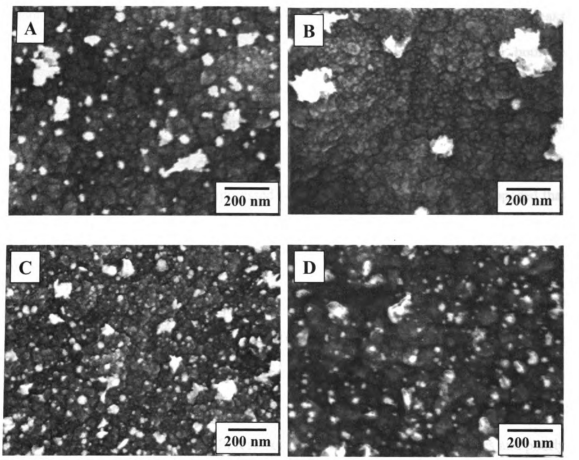

Figure 6.2. Scanning electron micrographs of as-deposited Pt/BND electrodes deposited using ten 1-s pulses at 1.25 mA/cm^2. The BND surfaces were (A) H-terminated, (B) O-terminated, (C) 4-NBD modified and (D) 4-MBD modified.

6.2.2 Electrochemical Response

Cyclic voltammetric *i-E* curves were obtained in deoxygenated 0.1 M $HClO_4$ for Pt/BMD and Pt/BND films possessing the different surface chemistries. The curves for the Pt/BMD films are shown in Figure 6.3. All scans were initiated at 200 mV and scanned in the positive direction at a scan rate of 50 mV/s. It can be seen that the curves for the H-terminated and O-terminated surfaces possess voltammetric features characteristic of clean polycrystalline Pt. These include a flat Pt oxide formation region

from 800-1100 mV, Pt oxide reduction at *ca.* 450 mV and four clearly resolved peaks between 0 and -200 mV due to hydrogen adsorption and desorption. However, both the diazonium modified electrodes had curves with some noticeable differences. First, the Pt oxide formation current is not flat but rather possesses a peak shape character that is most pronounced for the 4-NBD modified surface. Also, the charge in the hydrogen adsorption/desorption region is suppressed with no resolvable peaks. It is supposed that aryl admolecules on the diamond surface near the metal deposits interact with the surface to increase the "Pt oxide" current due to their oxidation and suppress the hydrogen adsorption/desorption charge. Surprisingly, potential cycling 100 times between -300 and 1500 mV did not improve the Pt voltammetric features consistent with strong contaminant adsorption on the surface. The voltammetric *i-E* curves for Pt deposited on the BND surfaces (not shown) exhibited similar features to those described for the Pt/BMD films (*i.e.*, well resolved Pt features for H- and O-terminated surfaces and poorly resolved Pt features for diazonium modified surfaces).

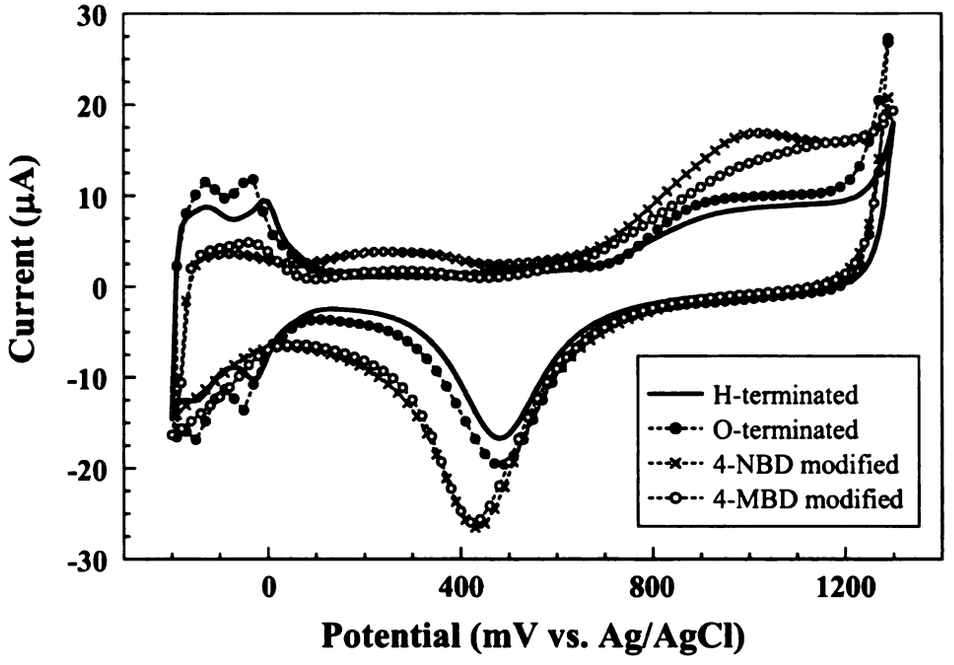

Figure 6.3. Cyclic voltammetric *i-E* curves in degassed 0.1 M $HClO_4$ for Pt-coated microcrystalline diamond electrodes as a function of the surface chemistry. Scan rate = 50 mV/s.

The poorly resolved hydrogen adsorption/desorption region for the diazonium modified diamond surfaces made determining the electrochemically active surface area (ESA) problematic. The hydrogen adsorption/desorption charge is often used to calculate this value and can be found by integrating either the anodic or cathodic current for the respective reaction between *ca.* 100 and -190 mV vs. Ag/AgCl and correcting for the double-layer charging current, as discussed previously.[6] While the charges associated with hydrogen adsorption and desorption on the clean Pt surfaces were approximately equal, the values for the diazonium modified surfaces were not. The charge associated with hydrogen adsorption was always several times larger than that for desorption. Therefore, we suppose that a parasitic reaction(s) was adding to the hydrogen adsorption

charge. One possibility is that the admolecule oxidation product formed during Pt-oxide formation gets reduced at potentials where hydrogen adsorption occurs. In any case, the hydrogen desorption charge was used to calculate the Pt ESA. The ESA obtained from the hydrogen adsorption/desorption charge and the roughness factor (RF = ESA normalized to the geometric area of the diamond, 0.2 cm^2) are summarized for the two diamond morphologies in Table 6.2. Surprisingly, the ESA for the H- and O-terminated BMD surfaces were quite similar despite the large difference in particle size and density. This is attributed to an increased surface roughness of the particles on the oxidized surface (*i.e.*, metal depositing on pre-existing growth centers). As expected, the 4-NBD modified surface exhibited the lowest ESA of the four. Interestingly, $BMD_{4\text{-}MBD}$ had a higher Pt ESA and RF despite possessing particles of similar size and density. This is attributed to the increased surface roughness due to the more irregularly shaped particles.

Table 6.2. Electrochemically Active Pt Surface Area (ESA) and Roughness Factor (RF) for Pt-Coated Microcrystalline and Nanocrystalline Diamond Films as a Function of the Surface Chemistry

Surface Chemistry	Microcrystalline Diamond		Nanocrystalline Diamond	
	Pt ESA (cm^2)	Roughness Factor	Pt ESA (cm^2)	Roughness Factor
H-terminated	0.15 ± 0.01	0.74	0.24 ± 0.03	1.2
O-terminated	0.18 ± 0.02	0.90	0.18 ± 0.03	0.90
4-NBD modified	0.013 ± 0.001	0.065	0.014 ± 0.003	0.070
4-MBD modified	0.06 ± 0.02	0.28	0.02 ± 0.01	0.11

RF = Electrochemically Active Pt Surface Area Normalized to Geometric Area of the Diamond, 0.2 cm^2.

The ESA values for the Pt/BND surfaces follow a more expected trend. The clean H-terminated surface exhibited the largest ESA, possessing the smallest particle size and largest particle density, followed by the clean O-terminated surface, and finally the 4-MBD and 4-NBD modified surfaces. Interestingly, the larger particle size and rougher particles on the O-terminated surface still do not result in a higher ESA than was observed for the large coverage of much smaller particles on the H-terminated surface.

6.2.3 Probing the Oxygen Reduction Reaction

The oxygen reduction reaction in 0.1 M $HClO_4$ at room temperature was used to investigate the effect of the diamond surface chemistry on the catalytic activity of the freshly deposited metal particles. Pt and Pt-based alloys are currently considered the most active catalysts for the ORR under acidic conditions, promoting the reaction via a 4-electron pathway as shown in equation 6.2.1.[24] This pathway is preferred from an energy density standpoint over the 2-electron pathway presented in equation 3.2.1.

$$O_2 + 4H^+ + 4e^- \rightleftarrows 2H_2O \qquad (E^o = 1.03 \text{ V } \textit{vs.} \text{ Ag/AgCl}) \qquad (6.2.1)$$

The linear sweep voltammetric *i-E* curves for the Pt-containing microcrystalline and nanocrystalline diamond films that were first modified by the four various surface chemistries are shown in Figures 6.4 and 6.5. The scans were recorded in the presence of dissolved O_2, initiated at 1000 mV and swept negative at a rate of 1 mV/s. For the microcrystalline diamond surfaces, it can be seen that both the reduction peak potential (E_p^{red}) and half-peak potential ($E_{p/2}^{red}$), displayed in Table 6.3, are invariant with the

surface chemistry. However, the curves vary significantly at potentials negative of the reduction peak suggesting that the mass transport of O_2 is different for each. The clean Pt/BMD_H and Pt/BMD_{ox} films reach a near steady state condition at *ca.* 200 mV. The $Pt/BMD_{4\text{-}MBD}$ film appears to approach a steady state condition at more negative potentials while the $Pt/BMD_{4\text{-}NBD}$ film does not. Instead, the mass transfer for this film appears to be a mixture of semi-infinite linear diffusion ($t^{-1/2}$) and steady-state diffusion (time independent decay), based on a qualitative analysis of the *i-t* curve shape. The differences in mass transfer are attributed to differences in the particle shape, size and spacing in relation to the time scale of the potential sweep rate.

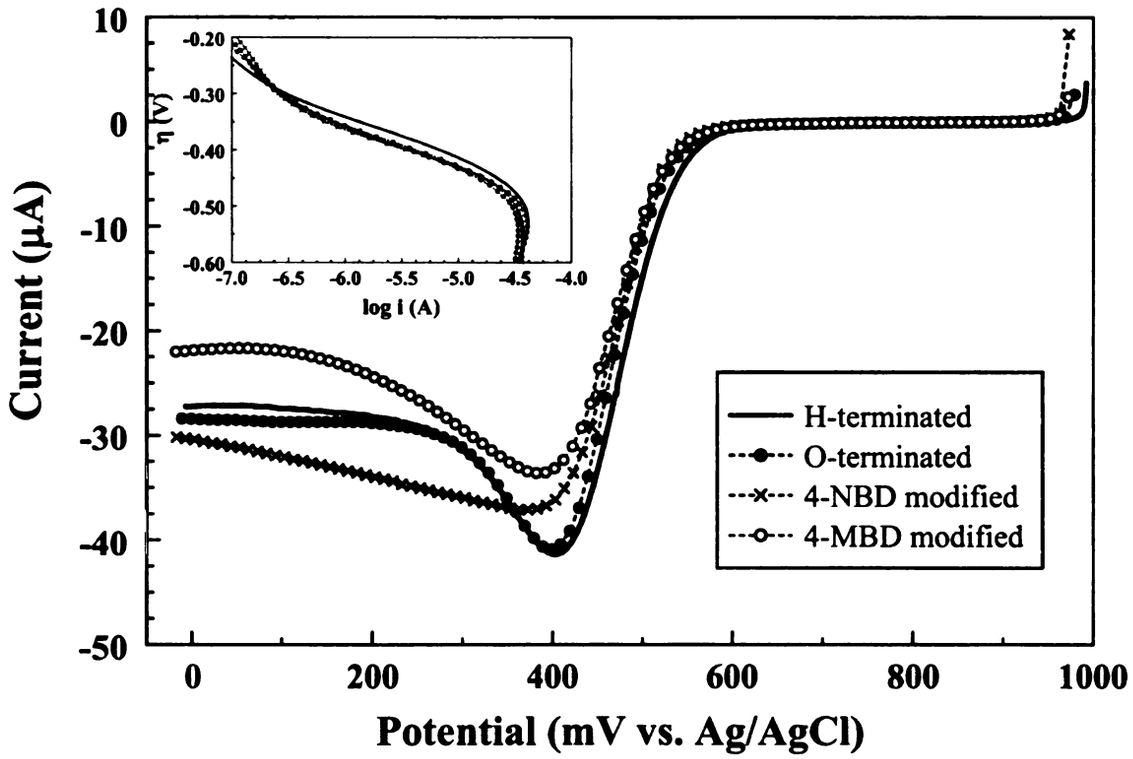

Figure 6.4. Linear sweep voltammetric *i-E* curves for the ORR in 0.1 M $HClO_4$ at Pt-coated microcrystalline diamond electrodes as a function of the surface chemistry. Scan rate = 1 mV/s. The corresponding Tafel plots are presented in the inset.

Table 6.3 Reduction Peak Potential (E_p^{red}) and Half-Peak Potential ($E_{p/2}^{red}$), Cathodic Peak Current (i_p^c) and Specific Activity (at E = 600 mV) for the Oxygen Reduction Reaction at Pt-Coated Microcrystalline Diamond Films as a Function of the Surface Chemistry

Surface Chemistry	E_p^{red} (mV)	$E_{p/2}^{red}$ (mV)	i_p^c (mA/cm^2_{Pt})[a]	Specific Activity (E = 600 mV, $\mu A/cm^2_{Pt}$)[a]
H-terminated	397 ± 7	479 ± 6	0.28 ± 0.01	4 ± 1
O-terminated	390 ± 30	460 ± 20	0.22 ± 0.01	3 ± 1
4-NBD modified	380 ± 20	480 ± 10	2.6 ± 0.2	32 ± 8
4-MBD modified	390 ± 20	470 ± 10	0.7 ± 0.3	8 ± 2

[a] Values Normalized to the Calculated Electrochemically Active Pt Surface Area (ESA) and the potential is reported on the Ag/AgCl reference scale

In contrast to the trends for the microcrystalline diamond electrodes, the voltammetric *i-E* curves for the Pt-coated nanocrystalline diamond electrodes, shown in Figure 6.5, exhibit significant variation in the E_p^{red} and $E_{p/2}^{red}$ values (summarized in Table 6.4) as a function of surface chemistry. Interestingly, these two values were significantly more positive for Pt/BND_H than for Pt/BND_{ox} and even Pt/BMD_H suggesting that these particles were more electrochemically active towards the reaction. This is somewhat contrary to that observed by others for oxidized GC towards methanol oxidation.[14,18] The activity differences might also be related to structural differences (Pt(*hkl*)) in the metal catalyst particles. For example, it is well known that the exchange current density for hydrogen evolution increases in the order $i_o(111) > i_o(100) > i_o(110)$, which gives a measure of the kinetic activity of the three surfaces. In contrast, the opposite is seen for the ORR, (100) < (110) ≅ (111). The 4-NBD modified BND surface, however, showed significantly more negative E_p^{red} and $E_{p/2}^{red}$ values than the same

modified BMD film. This may be due to a more evenly distributed aryl-adlayer over the smoother nanocrystalline surface and suggests the adlayer inhibits the reaction as opposed to acting as an extension of the electrode surface. All the curves reach a steady state mass transfer at potentials negative of 200 mV. It appears that the 4-NBD adlayer produces more of a blocking effect than the 4-MBD layer.

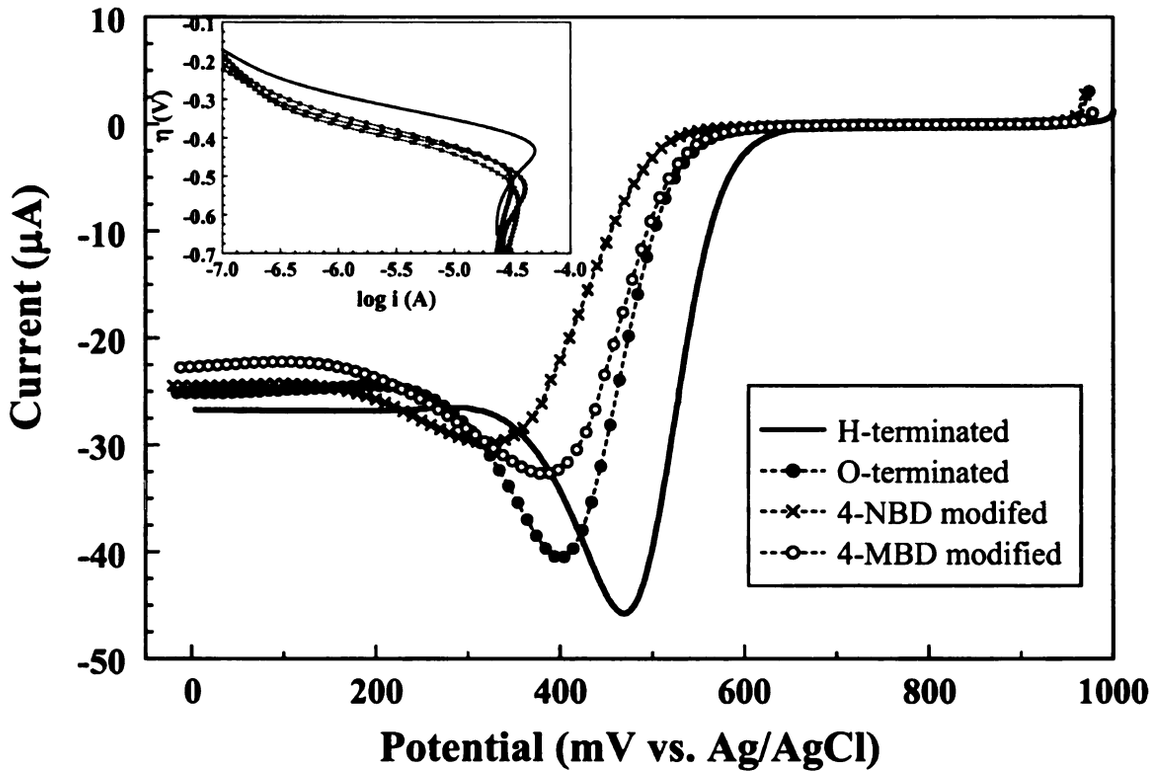

Figure 6.5. Linear sweep voltammetric *i-E* curves for the ORR in 0.1 M $HClO_4$ at Pt-coated nanocrystalline diamond electrodes as a function of the surface chemistry. Scan rate = 1 mV/s. The corresponding Tafel plots are shown in the inset.

The normalized peak current density was greatest for the 4-NBD and 4-MBD modified surfaces and smallest for the hydrogen- and oxygen-terminated surfaces, with the values differing by about an order of magnitude. We suppose though that these

values are high because of an underestimate of the active Pt area for the reaction (*e.g.*, ESA) based on the hydrogen adsorption/desorption charge measurement. In other words, the active area for the ORR is larger than that calculated from the voltammetric curves for hydrogen adsorption/desorption. In support of this, chronoamperometric *i-t* transients (discussed in the following section) obtained in the same solution and plotted using the well known Cottrell equation resulted in an unrealistically high calculated value for the number of electrons involved in the reaction, *ca.* 50-80, when using the Pt ESA determined from the hydrogen adsorption/desorption. However, if a Pt area of 0.2 cm^2 (RF = 1) was used, values between 3 and 5 were calculated, which is close to the predicted value of 4. The Pt ESA appears affected by admolecule contamination on the aryl-modified diamond surfaces. It is possible that the admolecule adsorption inhibits hydrogen adsorption/desorption but may facilitate the ORR. Verification of this would require further study.

Table 6.4. Reduction Peak Potential (E_p^{red}) and Half-Peak Potential ($E_{p/2}^{red}$), Cathodic Peak Current (i_p^c) and Specific Activity (at E = 600 mV) for the Oxygen Reduction Reaction at Pt-Coated Nanocrystalline Diamond Films as a Function of the Surface Chemistry

Surface Chemistry	E_p^{red} (mV)	$E_{p/2}^{red}$ (mV)	i_p^c (mA/cm^2_{Pt})[a]	Specific Activity (E = 600 mV, ($\mu A/cm^2_{Pt}$)[a]
H-terminated	470 ± 20	540 ± 10	0.20 ± 0.02	13 ± 5
O-terminated	400 ± 10	474 ± 7	0.23 ± 0.04	3 ± 1
4-NBD modified	330 ± 20	430 ± 20	2.3 ± 0.4	21 ± 3
4-MBD modified	390 ± 20	480 ± 10	1.6 ± 0.5	28 ± 3

[a] Values Normalized to the Calculated Electrochemically Active Pt Surface Area (ESA)

The specific activity (SA = current / cm^2 of electrochemically-active Pt) of an electrocatalyst is often used to describe the kinetic activity for the ORR.[25] Values calculated in this work are displayed in Tables 6.3 and 6.4. The SA is obtained by measuring the current at an overpotential of -330 mV; a potential at which the current is controlled by the electron transfer kinetics.[26,27] The equilibrium potential (E_{eq}) here was taken to be 930 mV vs. Ag/AgCl, assuming an O_2 concentration of 1.3 mM (estimated for 0.1 M $HClO_4$ at 25 °C)[28], a 4-electron transfer and accounting for the solution pH. Therefore, the current was measured at a potential of 600 mV, which corresponds to an overpotential of -330 mV.

Interestingly, the microcrystalline and nanocrystalline samples do not exhibit the same trends. The largest SA value for the Pt/BMD samples is observed for the 4-NBD film followed by the 4-MBD, H-terminated and O-terminated surfaces. The largest SA value for the Pt/BND samples, however, is observed for the 4-MBD surface, followed by the 4-NBD, H-terminated and O-terminated surfaces. The diazonium modified surfaces give the highest SA values likely due to an underestimated ESA. However, the SA on the clean diamond surfaces appears to correlate well with what one might expect based on the particle size and density observed in the SEM images. Pt/BND_H exhibited the largest SA (13 ± 5 $\mu A/cm^2_{Pt}$) while possessing rough spherical particles of the smallest size and largest density. Pt/BMD_H exhibited the second largest SA (4 ± 1 $\mu A/cm^2_{Pt}$) while possessing slightly larger, more spherically shaped particles and at a lower density compared to Pt/BND_H. Finally, both the oxidized films exhibited similar SA values (*ca.*

3 $\mu A/cm^2_{Pt}$) as a result of comparably large Pt agglomerates and a much lower particle density compared to the H-terminated diamond surfaces.

Tafel analysis of the *i-E* data was performed in the potential region where the reaction rate is limited by electron transfer. The corresponding plots are shown in the insets of Figures 6.4 and 6.5. The Tafel slope, uncorrected for mass transfer effects, the transfer coefficient and the exchange current density are presented for the two diamond electrode types in Tables 6.5 and 6.6. It can be seen that the Tafel slope and transfer coefficient depend little on the diamond film morphology or surface chemistry. These values range between *ca.* -70 – -75 mV/dec. and *ca.* 0.75 – 0.87, respectively. This indicates that mechanistically, the ORR is the same for all the surfaces and depends on the properties of Pt and not the support. In general, the exchange current density ranged from 10^{-10} to 10^{-11} A/cm^2_{Pt} (normalized to the Pt ESA), with the exception of the $Pt/BND_{4\text{-}MBD}$ sample. This film exhibited the highest exchange current density of 2 (± 1) x 10^{-9} A/cm^2_{Pt}. This could be connected to the high specific activity observed for the sample. The exchange current density depends on the crystallographic orientation, the Pt ESA and the solution conditions. The orientation and ESA are indirectly affected by the surface chemistry by virtue of its effect on Pt nucleation and growth.

Table 6.5. Summary of Values Obtained from Tafel Analysis of the ORR at Pt-Coated Microcrystalline Diamond Films as a Function of the Surface Chemistry

Surface Chemistry	Tafel Slope (mV/dec.)	α	j_o (10^{-10} A/cm$^2_{Pt}$)
H-terminated	-75 ± 2	0.79 ± 0.02	1.5 ± 0.2
O-terminated	-74 ± 4	0.80 ± 0.04	0.7 ± 0.2
4-NBD modified	-70 ± 1	0.85 ± 0.01	5 ± 2
4-MBD modified	-71 ± 9	0.8 ± 0.1	2 ± 1

Table 6.6. Summary of Values Obtained from Tafel Analysis of the ORR at Pt-Coated Nanocrystalline Diamond Films as a Function of the Surface Chemistry

Surface Chemistry	Tafel Slope (mV/dec.)	α	j_o (10^{-10} A/cm$^2_{Pt}$)
H-terminated	-68 ± 2	0.87 ± 0.02	1.7 ± 0.4
O-terminated	-73 ± 2	0.81 ± 0.02	0.9 ± 0.4
4-NBD modified	-77 ± 3	0.77 ± 0.03	8 ± 2
4-MBD modified	-80 ± 4	0.74 ± 0.03	20 ± 10

6.2.4 Investigating the Oxygen Reduction Mechanism

The oxygen reduction mechanism was investigated at the different Pt-diamond electrodes. The conclusions reached are based on one set of measurements using each technique. Cyclic voltammetric *i-E* curves were recorded at scan rates from 1 mV/s to 10 V/s, and the data were evaluated in the manner described in Chapter 3. Since the ORR is an irreversible reaction, the *i-E* curve is expected to follow the trends given by equations 6.2.2 to 6.2.4.

$$E_p = E^{o'} - \frac{RT}{\alpha n_a F}\left[0.780 + \ln\left(\frac{D_o^{1/2}}{k^0}\right) + \ln\left(\frac{\alpha F v}{RT}\right)^{1/2}\right] \quad (6.2.2)$$

$$i_p = 2.99 \times 10^5 n(\alpha n_a)^{1/2} A D_o^{1/2} C_o^* v^{1/2} \quad (6.2.3)$$

$$i_p = 0.227 n F A C_o^* k^0 \exp\left[-\left(\frac{\alpha n_a F}{RT}\right)\left(E_p - E^{o'}\right)\right] \quad (6.2.4)$$

Indeed plots of i_p vs. $v^{1/2}$ and ln i_p vs. $(E_p - E^o)$ (assuming $E^o = E^{o'}$) exhibited linear trends and were used to calculate αn_a, the stoichiometric number of electrons transferred (n) and the rate constant (k^0). These values along with the individually determined Pt ESA from the hydrogen adsorption/desorption charge measurements are summarized for the two diamond types in Tables 6.7 and 6.8. Note that there are two k^0 values presented in each table that correspond to a value calculated using the n value determined experimentally (referred to in the table as $n_{exp.}$) and the other to a value found using the assumed value n = 4.

There are two points worth noting here. First, Pt on hydrogen- and oxygen-terminated diamond behaves in a similar manner independent of the diamond type as n values of 2-4 and k^0 values in the mid-10^{-5} cm/s range are seen. In comparison, Marković *et al.* found n values of 4 and k^0 values of *ca.* 10^{-2} cm/s for single crystal Pt electrodes in 0.1 M $HClO_4$ at 22 °C using rotating-disk measurements.[29] Second, there is no n value listed for any of the aryl-modified films because of its unrealistic value. It appears that

there must be a larger surface area participating in the ORR than estimated from the hydrogen adsorption/desorption charge for the aryl-molecule modified films because the αn_a values are similar to that obtained for the clean films and there is no possible way to observe n values of 18-25. Additionally, considering the voltammetric *i-E* curves in Figures 6.4 and 6.5, there is no way that the modified surfaces could exhibit a higher rate constant for the reaction by nearly an order of magnitude.

Table 6.7. Electrochemical Quantities Determined Using Cyclic Voltammetric Data Obtained for the ORR at Pt-Coated Microcrystalline Diamond Films as a Function of the Surface Chemistry

Parameter	H-terminated	O-terminated	4-NBD mod.	4-MBD mod.
Pt ESA (cm^2)	0.14	0.12	0.016	0.014
αn_a	0.231	0.187	0.187	0.182
n	3.5	2.4	???	???
k^0 (cm/s, $n = n_{exp.}$)	4.8×10^{-5}	3.4×10^{-5}	—	—
k^0 (cm/s, $n = 4$)	4.2×10^{-5}	2.1×10^{-5}	1.2×10^{-4}	1.5×10^{-4}

Table 6.8. Electrochemical Quantities Determined Using Cyclic Voltammetric Data Obtained for the ORR at Pt-Coated Nanocrystalline Diamond Films as a Function of the Surface Chemistry

Parameter	H-terminated	O-terminated	4-NBD mod.	4-MBD mod.
Pt ESA (cm^2)	0.16	0.20	0.015	0.011
αn_a	0.185	0.175	0.190	0.212
n	2.9	2.2	???	???
k^0 (cm/s, $n = n_{exp.}$)	5.0×10^{-5}	7.0×10^{-5}	—	—
k^0 (cm/s, $n = 4$)	3.7×10^{-5}	4.0×10^{-5}	2.2×10^{-4}	1.3×10^{-4}

It appears that the calculated Pt ESA values for the aryl-modified surfaces are an underestimate for the ORR active area. By comparison, if it is assumed that the active Pt area is equal to the geometric electrode area (0.2 cm^2) and the values for the aryl molecule-modified surfaces in Tables 6.7 and 6.8 are recalculated, then n values of *ca.* 1.5 and k^0 values of *ca.* 10^{-5} are obtained, which are certainly more reasonable.

The same set of measurements was also preformed using a polished polycrystalline Pt electrode. A Pt ESA value of 0.31 cm^2 was determined based on the hydrogen adsorption charge. This electrode exhibited the following values: $\alpha n_a = 0.188$, $n = 1.5$ and $k^0 = 4.0 \times 10^{-5}$ ($n = n_{exp.}$) or 1.5×10^{-5} ($n = 4$) cm/s. The Pt nanoparticles deposited on the diamond surfaces exhibited similar values suggesting that indeed the reaction proceeds via the same mechanism on the Pt nanoparticles as it does on the bulk Pt electrode. As observed in Chapter 3, n values determined using this method is lower than the predicted value.

Comparatively, the number of electrons involved in the reaction (n) was also determined using a large amplitude potential step technique and corresponding $i\text{-}t^{-1/2}$ plots with the Cottrell equation (3.2.10). As expected, an n value of 4.2 was observed for the polycrystalline Pt electrode, consistent with the 4-electron reaction. Pt deposited on the oxidized diamond surfaces exhibited similar values, ranging from 4-5. However, n values calculated for the Pt-coated H-terminated diamond surfaces were *ca.* 8. This also suggests that the Pt ESA calculated from hydrogen adsorption is less than that participating in the ORR. These results were able to be repeated on another H-terminated

film. However, if we assume the literature value for *n* of 4, the Pt ESA calculated for the Pt-coated H-terminated diamond films using the Cottrell equation is *ca.* 0.33 cm^2. Additional evidence that the Pt ESA was underestimated for the aryl molecule-modified diamond films is the fact that *n* values calculated using the Pt ESA values determined from the hydrogen desorption process ranged from 47-79. However, if we again assume a Pt surface area of 0.2 cm^2, *n* values of 3.7-4.5 were determined. It is obvious from the data at hand that the Pt ESA calculated using the hydrogen adsorption/desorption process is not the same area that participates in the ORR. It is possible that the reduction of Pt-oxides or oxygen concentrated within the Pt lattice contributes to the ORR current therefore resulting in errant measurements. This significantly complicates matters in regards to determining the reaction mechanism. Much more work is needed to understand how structural effects influence the reaction mechanism on Pt-diamond electrodes.

It appears that the ORR on the H- and O-terminated films proceeds via a 4-electron pathway. The question is does the mechanism proceed through a direct 4-electron pathway to H_2O, as shown in equation 6.2.1, or through an indirect mechanism as shown in equations 6.2.5 – 6.2.7 and proposed by Yeager?[30,31]

$$O_2 + 2H^+ + 2e^- \rightarrow H_2O_2 \quad (E^o = 473 \text{ mV vs. Ag/AgCl}) \qquad (6.2.5)$$

followed by either

$$H_2O_2 + 2H^+ + 2e^- \rightarrow 2H_2O \quad (E^o = 1.57\ V\ vs.\ Ag/AgCl) \qquad (6.2.6)$$

or

$$2H_2O_2 \rightarrow 2H_2O + O_2 \qquad (6.2.7)$$

Oxygen reduction on Pt and Pt-alloys supported on carbon is known to proceed primarily through the direct pathway with minor contributions from the indirect mechanism.[31,32] This would be consistent with the initial step shown in equation 6.2.8 followed by the 4-electron reduction shown in equation 6.2.1.

$$O_2 \rightarrow O_2(ads) \qquad (6.2.8)$$

Examining the standard reduction potential for equation 6.2.5, it is clear that H_2O_2 can not be produced except at potentials past the reduction peak potentials observed in the voltammetric *i-E* curves (*i.e.*, E < 473 mV). Additionally, if H_2O_2 is produced, this species is also likely adsorbed on Pt since it appears that the reaction goes to completion with a final *n* value of 4. It is suspected that the ORR on H-terminated Pt-diamond proceeds almost entirely though the direct 4-electron pathway as with each experiment, the H-terminated surfaces gave a more positive reduction potential, higher *n* value and slightly higher k^0 compared to the oxidized sample. It is likely that the ORR on the oxidized diamond films also proceeds primarily through the direct pathway; however, it appears that the indirect pathway contributes more to the overall reaction based on the

calculated n value from the i-E curves. This could be due to oxygen-containing functional groups forcing an end-on interaction between the O_2 and Pt (as opposed to a bridged interaction) by blocking certain regions of the metal and promoting H_2O_2 formation. This is similar to the theory proposed by Jovanović *et al.* whereby oxygen groups on the carbon surface promote a higher fraction of oxygen containing species in the Pt catalyst.[18]

6.2.5 Investigating Particle Stability

There have been numerous studies devoted to evaluating catalyst surface area loss for carbon-supported platinum.[33-42] It is well known that metal particles, while in good electrical contact, can be unstable on the diamond surface.[2,43,44] In addition to examining surface chemistry affects on metal deposition, we also investigated the causes for lost catalytic activity with the goal of learning how to better stabilize the particles on the diamond surface without the use of a binding agent or secondary diamond growth. Several experiments were performed, all in 0.1 M $HClO_4$ at room temperature. The individual experiments and key findings are summarized below.

- The stability of the Pt particles was assessed under open circuit conditions by exposing the Pt/diamond film to a quiescent 0.1 M $HClO_4$ solution in the presence and absence of O_2. In general, there was no change in the Pt ESA in the deoxygenated solution ($\geq$ 50 h) while the Pt ESA decreased by 2-15% in the presence of O_2, independent of the surface chemistry or the exposure time ($\leq$ 18 h). This means that catalyst detachment

during solution exposure is not a problem, but does suggest some slight oxidation of the metal upon exposure to O_2 saturated solutions.

- Cycling the potential of the Pt/diamond (H- and O-terminated) films 1000 times between -0.35 and 1.7 V (*ca.* ±3 mA/cm^2 (geometric area)) resulted in a Pt ESA decrease of *ca.* 40-50% (n = 2 – 4). The Pt/BMD_{ox} film lost the least amount of Pt ESA of all the films tested; however, the loss was still significant (*ca.* 30%). Exposure to these extreme potentials caused a significant reduction in the available Pt area. Two possible causes for this are oxidation (corrosion) of the Pt at anodic potentials and detachment of the particles during hydrogen evolution.
- The particle stability on H-terminated diamond was also investigated by cycling the potential 1000 times in deoxygenated 0.1 M $HClO_4$ within increasingly expanded potential limits. Overall, the Pt ESA decreased only ~14% if the potential limits were kept below the values where significant gas evolution occurs (-0.2 and 1.2 V).
- The effect of the different gas evolution reactions was studied at freshly deposited Pt/BMD_H films (n = 2) by holding the current at either -0.1 (H_2 evolution) or +0.1 (O_2 evolution) A/cm^2 (geometric area) for 2 h.
  - Holding the current at -0.1 A/cm^2 for 2 h initially resulted in a 25-30% decrease in the Pt ESA as determined using the hydrogen adsorption process, but returned to the initial value (within 3%) after allowing the film to soak overnight in ultrapure water. It would appear that some of the area of the rough, porous Pt particles was initially blocked by H_2 gas.
  - Additionally, the response towards the ORR (recorded after full recovery of the Pt ESA) changed as shown in Figure 6.6. Instead of exhibiting a reduction peak as

usual, both electrodes exhibited "microelectrode" behavior, reaching a steady-state current (constant flux to the active sites). The different mass transfer indicates there must be some redistribution of the particles such that they are further spaced (*i.e.*, individual hemispherical diffusion zones).

- Holding the current at +0.1 A/cm^2 for 2 h; however, resulted in a Pt ESA decrease of 84%. This suggests that Pt loss observed from potential cycling is primarily due not to gas evolution but rather to metal oxidation and corrosion.

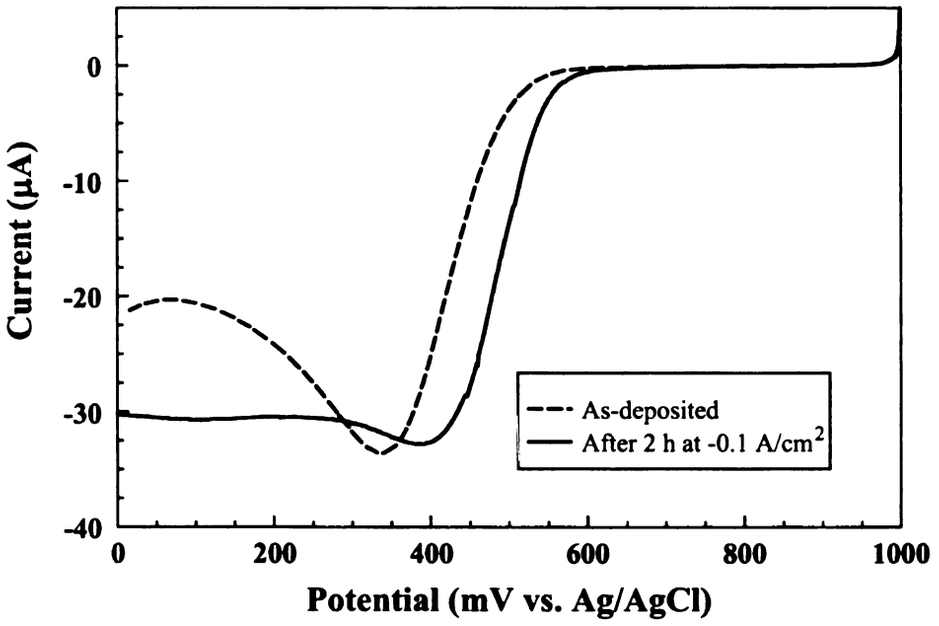

Figure 6.6. ORR linear sweep voltammetric *i-E* curves for Pt/BMD$_H$ electrode in 0.1 M $HClO_4$ before (– – –) and after (——) 2 h cathodic polarization of -0.1 A/cm^2. Scan rate = 1 mV/s.

6.3 Conclusions

It was previously concluded from studies of microcrystalline and nanocrystalline diamond that the film morphology plays a role in metal phase formation by influencing

particle size and density.[6] Additionally, it has been shown here that the surface chemistry plays only a minor role in metal phase formation on both types of diamond. The most relevant surface terminations to compare are hydrogen and oxygen. Rough spherical particles were formed on both diamond film types possessing H- and O-termination but the roughness and nominal diameter increased and the density decreased with increasing surface oxide content, based on XPS measurements. We previously suggested that metal deposits form preferentially on active sites and that these sites possess a differential potential dependent activity. Oxidizing or modifying the diamond surface further enhances this effect by decreasing the number of active sites through blockage effects. This produces particles of lower density, larger diameter and rougher surface morphology. Of all the films studied, the Pt/BND_H film possessed particles closest to our target in terms of particle size and density, and exhibited the best electrocatalytic activity towards the ORR.

Interestingly, oxidizing the surface had minimal effect on the electrochemically active surface area of the Pt, based on the recorded hydrogen adsorption/desorption charges and the catalytic activity of the particles towards the oxygen reduction reaction. The particles deposited on this surface possess an increase in microscopic surface roughness. It is likely that a given set of pulse conditions results in a similar relative mass loading and the properties of the diamond (*i.e.,* surface chemistry, morphology, conductivity) affect where and how the particles are deposited.

In addition to the effects of H- and O-termination, a brief look was given to the effect of modifying the diamond surface with aryl-adlayers using the reduction of corresponding diazonium salts. In short, the presence of the aryl-adlayer did not appear to influence the particle size or density to a great extent. There was a slight increase in size and decrease in coverage with the presence of the adlayer suggesting that it acts more as a blocking layer rather than an extension of the electrode surface. The presence of an aryl-adlayer did appear to influence the particle shape as it transitioned from a spherical shape on the non-modified diamond surfaces to a more elongated shape with a dendritic morphology on the modified surfaces. Interestingly, the presence of the adlayer had a profound effect on the electrochemical behavior of the deposited metal. Despite a similar particle size and density, the calculated ESA based on hydrogen desorption was an order of magnitude less than on the clean diamond surfaces consistent with the adlayer acting as a contaminant for the reaction. Additionally, the structure of the aryl-adlayer appears to be a function of diamond morphology as particles deposited on aryl-modified diamond in the same manner possessed very different catalytic activities. We suppose that modifying the smoother more homogeneous nanocrystalline diamond surface likely results in a more continuous coverage while modifying the rougher more heterogeneous microcrystalline diamond likely results in unevenly dispersed clumps of the aryl molecules, though this has yet to be confirmed.

It appears that putting a negative charge on the diamond surface did not promote nor inhibit Pt complex-ion adsorption. While it is possible that this adsorption would result in more stable particles at lower pulse numbers and at 10 pulses this advantage is

not seen, it is likely that the procedure proposed by Yan and coworkers does not work because the Pt cation remains complexed to the Cl anions in solution making the overall complex anionic ($PtCl_6^{4-}$). Both these possibilities can be investigated further by (*i*) putting a positive charged molecule on the diamond surface and (*ii*) investigating how the deposition proceeds with each individual pulse number using electrochemical atomic force microscopy (EC-AFM).

In addition to developing a new carbon support material to mitigate catalyst activity loss due to support oxidation and/or corrosion, research was performed to learn how to better stabilize the metal deposits on the diamond surface. Potential cycling experiments suggested that decreases in the active Pt area appear to be relatively independent of the applied potential as long as the value is within the working potential window. This means that simple metal phase detachment in solution is not a major cause for lost catalytic activity. This also suggests that the increase in Pt crystallite size is not due to dissolution and re-deposition of platinum ions.[36,42] Hydrogen gas evolution did not cause severe loss in activity so the turbulence of gas evolution is not problematic. The main decrease in catalyst activity occurs under anodic conditions where the Pt can oxidize or corrode via potential cycling beyond the limits of excessive gas evolution.

The SEM image after the H_2 evolution exposure showed that the majority of the particles were large rough agglomerates residing primarily in defect sites (*i.e.*, grain boundaries or intersections between two crystallite faces) on the diamond surface. One possible explanation for this is the Ostwald ripening model in which metal crystallites

dissociate to metal atoms which then diffuse to and associate with larger particles.[42] Bett *et al.* point out that this model is frequently dismissed due to the large energy difference between the adatom on the support and the adatom on the metal surface.[42] This energy difference would make the activation energy for an atom transfer process too large. However, they also go on to say that Geus has argued that the presence of defect sites has the possibility of significantly increasing the bonding strength of the adatom to the support and thereby reducing the activation energy required for an atom transfer process.[45] The large particles in the SEM image mainly reside at defect sites suggesting the possibility of Ostwald ripening as the major cause of particle sintering on diamond. Additionally, the presence of mostly large particles as well as some very small particles is also consistent with an Ostwald ripening model.[34,36]

Significant Pt loss was only observed upon O_2 evolution suggesting that the major cause of Pt loss from diamond was due to Pt oxidation/corrosion and not physical detachment. This Ostwald ripening mechanism has been observed by others with regards to specific fuel cell testing.[42,46,47] Since a weak Pt-diamond interaction is not the reason for Pt loss, it seems logical to assume that the surface chemistry of the diamond would not significantly influence Pt stability. This is consistent with what we observed here with regards to H- vs. O-termination. Eliminating both the support material and the metal-support interaction as the cause for catalyst degradation further supports our conclusion that the properties of the metal are the most influential cause for decreased activity. Therefore, research is necessary in developing a more corrosion resistant catalyst material to further advance the use of fuel cells in real life applications.

REFERENCES

1. A. E. Fischer and G. M. Swain, *J. Electrochem. Soc.*, **152**, B369 (2005).

2. J. Wang, G. M. Swain, T. Tachibana, and K. Kobashi, *J. New Mater. Electrochem. Sys.* , **3**, 75 (2000).

3. J. Wang, G. M. Swain, T. Tachibana, and K. Kobashi, *Electrochem. Solid-State Lett.*, **3**, 286 (2000).

4. J. Wang and G. M. Swain, *Electrochem. Solid-State Lett.*, **5**, E4 (2002).

5. J. Wang and G. M. Swain, *J. Electrochem. Soc.*, **150**, E24 (2003).

6. J. A. Bennett, Y. Show, S. Wang, and G. M. Swain, *J. Electrochem. Soc.*, **152**, E184 (2005).

7. Y. Zhang, V. Suryanarayanan, I. Nakazawa, S. Yoshihara, and T. Shirakashi, *Electrochim. Acta*, **49**, 5235 (2004).

8. C. G. Vayenas, D. Archonta, and D. Tsiplakides, *J. Electroanal. Chem.*, **554-555**, 301 (2003).

9. J. S. Noh and J. A. Schwarz, *Carbon*, **28**, 675 (1990).

10. F. Coloma, A. Sepúlveda-Escribano, J. L. G. Fierro, and F. Rodríguez-Reinoso, *Langmuir*, **10**, 750 (1994).

11. H. E. van Dam and H. van Bekkum, *J. Catal.*, **131**, 335 (1991).

12. C. Prado-Burguete, A. Linares-Solano, F. Rodríguez-Reinoso, and C. Salinas-Martíez De Lecea, *J. Catal.*, **115**, 98 (1989).

13. D. J. Suh, T.-J. Park, and S.-K. Ihm, *Carbon*, **31**, 427 (1993).

14. F. Gloaguen, J.-M. Léger, and C. Lamy, *J. Appl. Electrochem.*, **27**, 1052 (1997).

15. Y. Zhang, M. L. Toebes, A. van der Eerden, W. E. O'Grady, K. P. de Jong, and D. C. Koningsberger, *J. Phys. Chem. B*, **108**, 18509 (2004).

16. M. Kang, H. K. Yoon, B. H. Kim, M. W. Song, and C. H. Lee, *React. Kinet. Catal. Lett.*, **80**, 139 (2003).

17. M. C. Román-Martínez, D. Cazorla-Amorós, A. Linares-Solano, C. Salinas-Martíez De Lecea, H. Yamashita, and M. Anpo, *Carbon*, **33**, 3 (1995).

18. V. M. Jovanović, S. Terzić, A. V. Tripković, K. D. Popović, and J. D. Lović, *Electrochem. Commun.*, **6**, 1254 (2004).

19. T.-C. Kuo, R. L. McCreery, and G. M. Swain, *Electrochem. Solid-State Lett.*, **2**, 288 (1999).

20. J. Wang, M. A. Firestone, O. Auciello, and J. A. Carlisle, *Langmuir*, **20**, 11450 (2004).

21. D. Knigge, P. Kaur, and G. M. Swain, *Unpublished results*.

22. M. M. Waje, X. Wang, W. Li, and Y. Yan, *Nanotechnology*, **16**, S395 (2005).

23. L. Zhang, T. Sakai, H. Yoshida, S. Yamanaka, and H. Okushi, *J. Appl. Phys.*, **91**, 4585 (2002).

24. A. J. Bard and L. R. Faulkner, *Electrochemical Methods: Fundamentals and Applications*, John Wiley & Sons, Inc., New York (2001).

25. K. Kinoshita, *Electrochemical Oxygen Technology*, John Wiley & Sons, Inc., New York (1992).

26. J. A. Poirier and G. E. Stoner, *J. Electrochem. Soc.*, **141**, 425 (1994).

27. U. A. Paulus, T. J. Schmidt, H. A. Gasteiger, and R. J. Behm, *J. Electroanal. Chem.*, **495**, 134 (2001).

28. N. Wakabayashi, M. Takeichi, M. Itagaki, H. Uchida, and M. Watanabe, *J. Electroanal. Chem.*, **574**, 339 (2005).

29. N. M. Marković, R. R. Adzić, B. D. Cahan, and E. B. Yeager, *J. Electroanal. Chem.*, **377**, 249 (1994).

30. E. Yeager, *Electrochim. Acta*, **29**, 1527 (1984).

31. E. Yeager, *J. Mol. Catal.*, **38**, 5 (1986).

32. M. Inaba, H. Yamada, J. Tokunaga, and A. Tasaka, *Electrochem. Solid-State Lett.*, **7**, A474 (2004).

33. E. Antolini, *J. Mater. Sci.*, **38**, 2995 (2003).

34. M. S. Wilson, F. H. Garzon, K. E. Sickafus, and S. Gottesfeld, *J. Electrochem. Soc.*, **140**, 2872 (1993).

35. Y. Mo, S. Sarangapani, A. Le, and D. A. Scherson, *J. Electroanal. Chem.*, **538-539**, 35 (2002).

36. G. A. Gruver, R. F. Pascoe, and H. R. Kunz, *J. Electrochem. Soc.*, **127**, 1219 (1980).

37. P. Bindra, S. J. Clouser, and E. Yeager, *J. Electrochem. Soc.*, **126**, 1631 (1979).

38. A. C. C. Tseung and S. C. Dhara, *Electrochim. Acta*, **20**, 681 (1975).

39. L. J. Bregoli, *Electrochim. Acta*, **23**, 489 (1978).

40. K. F. Blurton, H. R. Kunz, and D. R. Rutt, *Electrochim. Acta*, **23**, 183 (1978).

41. A. Honji, T. Mori, K. Tamura, and Y. Hishinuma, *J. Electrochem. Soc.*, **135**, 355 (1988).

42. J. A. S. Bett, K. Kinoshita, and P. Stonehart, *J. Catal.*, **41**, 124 (1976).

43. S. Nakabayashi, D. A. Tryk, A. Fujishima, and N. Ohta, *Chem. Phys. Lett.*, **300**, 409 (1999).

44. N. Vinokur, B. Miller, Y. Avyigal, and R. Kalish, *J. Electrochem. Soc.*, **146**, 125 (1999).

45. J. W. Geus, in *Chemisorption and Reactions on Metallic Films*, J. R. Anderson, Editor, **1**, p. 129, Academic Press, New York, (1971).

46. P. J. Ferreira, G. J. la O', Y. Shao-Horn, D. Morgan, R. Makharia, S. Kocha, and H. A. Gasteiger, *J. Electrochem. Soc.*, **152**, A2256 (2005).

47. R. M. Darling and J. P. Meyers, *J. Electrochem. Soc.*, **150**, A1523 (2003).

CHAPTER 7

Key Findings and Future Research Directions

7.1 Key Findings

Growing concern over environmental impacts, limited fuel supplies and reliance on foreign oil has lead to considerable interest in fuel cells as a clean, renewable energy alternative for stationary and portable power applications. While there have been considerable advances made in fuel cell materials research in the last decade, there are still several technological hurdles that need to be overcome before fuel cells can become commercially viable. Two hurdles are (*i*) catalyst cost and activity loss which must be reduced through decreased metal loading and development of non-noble metal catalysts and (*ii*) prevention of carbon support degradation through the development of more dimensionally stable and corrosion resistant electrocatalyst supports.

The research conducted for this dissertation had the goal of advancing diamond as a state-of-the-art electrocatalyst support material through a better understanding of metal phase formation, electrocatalytic activity and stabilization. The key findings of this research are summarized as follows:

1. The physical and electrochemical properties of diamond can be easily altered by adjusting the CH_4/H_2 deposition source gas ratio. Increasing the CH_4/H_2 ratio increases the rate of secondary nucleation leading to an increase in the fraction of grain boundary

exposed, a decrease in both the diamond crystallite size and overall film roughness, and an increasing amount of sp^2-bonded nondiamond carbon impurity incorporated into the film microstructure. The presence of this sp^2-bonded nondiamond carbon strongly influences the electron-transfer kinetics for some reactions (*e.g.*, $Fe^{3+/2+}$, 4-*tert*-butylcatechol, and the ORR in acid and alkaline solution) and exerts little influence on others (*e.g.*, $Fe(CN)_6^{3-/4-}$ and $Ru(NH_3)_6^{3+/2+}$).

2. Boron-doped microcrystalline and nanocrystalline diamond are both structurally stable under polarization conditions commonly encountered in PAFCs. Both diamond types exhibit some surface oxidation resulting in slight roughening of the crystallite edges; however, no gross morphological degradation occurs. Additionally, any alteration in the electrochemical response of the material towards several well known redox couples is reversed by rehydrogenation. The only irreversible change seen is an increase in background voltammetric current exhibited by the nanocrystalline diamond film. It appears that for these thin, nanograined films, solution can penetrate the grain boundaries and react with the underlying Si. This penetration is enabled by the minor structural changes that occur during polarization.

3. The use of pulsed galvanostatic deposition produces metal particles with a small nominal particle diameter and a high particle density. This method is superior to constant current/potential deposition methods reported on by our group in the past. Deposition using ten 1-s pulses at 1.25 mA/cm^2 yields the most ideal electrocatalyst on both diamond types in terms of the nominal particle size (*ca.* 30-40 nm), particle coverage (10^9-10^{10} cm^{-}

^{2}) and the highest specific Pt surface area (*ca.* 25-50 m^2/g_{Pt}). The heterogeneous diamond surface possesses sites that exhibit a differential potential dependent activity towards metal phase formation. Additionally, the Pt nucleation mechanism on diamond transitions from an instantaneous mechanism at low overpotentials to a more progressive one at high overpotentials.

4. The diamond surface chemistry plays a minor role in metal phase formation or stability. The roughness and nominal particle diameter increases and the density decreases with increasing surface oxide content. Oxidizing or modifying the diamond surface decreases the number of active sites available for deposition through blocking effects. Pt/BND_H exhibits the highest catalytic activity for the oxygen reduction reaction. Finally, the loss of Pt catalyst from the diamond surface is not due to degradation of the diamond or physical displacement of the particles, but rather due to oxidation and corrosion of the metal. The results are consistent with an Ostwald ripening mechanism.

7.2 Future Research Needs

The research advanced diamond as an advanced electrocatalyst support material; however, a number of issues remain to be determined. Some future research topics are given below.

1. While diamond shows promise as a dimensionally stable electrocatalyst support material, further work is required to produce the material in a high surface area form (~100 m^2/g). A step towards this goal may require the incorporation of sp^2-bonded

nondiamond carbon impurity through increases in the CH_4/H_2 source gas ratio. A mixed sp^3/sp^2 material may be easier to deposit on high surface area materials. Additionally, diamond is a hydrophobic material and increasing the hydrophilicity of the material through sp^2-bonded nondiamond carbon incorporation may result in better contact with the Nafion membrane and thus reduce the resistance in the membrane electrode assembly while still maintaining satisfactory electrical conductivity and dimensional stability.

2. Additional optimization of the metal phase formation by studying the effect of pulse width and duty cycle. An informative way to study metal adlayer formation on diamond is to image the surface *in situ* using electrochemical-atomic force microscopy (EC-AFM). This method will (*i*) aide in determining the exact nucleation and growth mechanism of Pt on diamond, (*ii*) allow for the real-time monitoring of particle growth with each pulse so the pulse parameters can be more easily optimized and (*iii*) allow for the monitoring of any changes in the particles with electrochemical cycling (*i.e.*, particles moving during cyclic voltammetric cleaning). Perhaps the particles change when we do the potential cycling to activate the Pt and we only see the end result when viewing using SEM.

3. Additionally, a procedure for electrodepositing metal particles on high surface area forms of carbon (*e.g.*, diamond) needs to be developed. Two approaches are being followed by the group: overcoating conducting diamond on diamond polishing grit and on carbon paper. The architecture of the high surface area carbon will likely affect the metal deposition process, especially in terms of wettability and current density.

However, an increased support area will likely make it easier to deposit particles with the desired properties. We have designed electrochemical cells that could house powderous diamond for electrochemical testing. Two ideas that appear promising are based on the works of Tran and Langer[1] or Porter and coworkers.[2,3]

4. Work is needed to reduce the metal loading while still maintaining high electrocatalytic activity. Also, alternate electrocatalysts need to be discovered. Perhaps the deposition of Pt-alloys or Pt on non-noble catalysts will help to reduce both Pt particle size and loading while increasing the catalyst activity. Additionally, if the electrodeposition process can not be optimized, alternative deposition methods must be investigated. Possible alternatives include impregnation, microemulsion or colloid. A key factor in optimizing the catalyst layer is understanding the factors that influence the activity of the deposited catalyst towards H_2 oxidation and O_2 reduction.

5. Understanding the interaction between the catalyst particle and the carbon support material is important for particle stabilization on the diamond surface. So far, a secondary diamond growth appears to be the most promising method, however as mentioned previously, microcrystalline diamond has crystallites that are too large for our target particles. Therefore a secondary nanocrystalline diamond growth procedure should be investigated as a method for stabilizing particles < 30 nm as well as particles on a high surface area form of diamond.

6. Finally, membrane electrode assemblies (MEAs) must be developed and tested in actual PEMFCs and PAFCs. The stability and activity of the electrocatalyst particles must be monitored and compared to that for commonly used fuel cell electrodes.

REFERENCES

1. T. D. Tran and S. H. Langer, *Anal. Chem.*, **65**, 1805 (1983).

2. R. S. Deinhammer, E.-Y. Ting, and M. D. Porter, *Anal. Chem.*, **67**, 237 (1995).

3. J. A. Harnisch, D. B. Gazda, J. W. Anderegg, and M. D. Porter, *Anal. Chem.*, **73**, 3954 (2001).

APPENDIX A

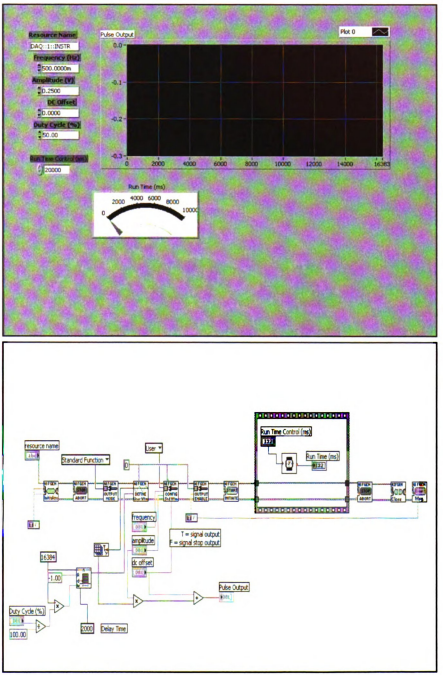

Figure A.1. Front panel and schematic code for the potential pulse generator program created in LabVIEW Version 6.1 in conjunction with a National Instruments PCI-5401 card. The parameters in the top window were those used to deposit Pt using 10 pulses of 1 s (delay 1 s for 50% duty cycle) and a pulse current density of 1.25 mA/cm^2.


MICHIGAN STATE UNIVERSITY LIBR
3 1293 02845 53